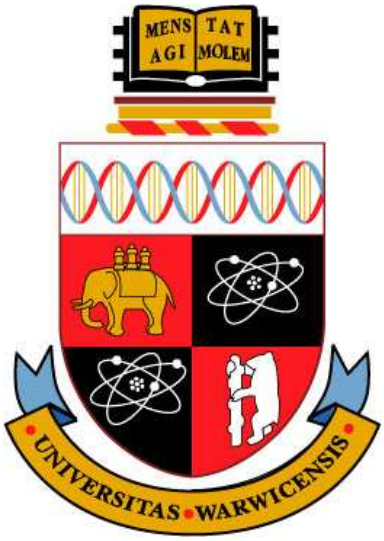

Statistical Description and Modelling of Fusion Plasma Edge Turbulence

by

Joseph Michael Dewhurst

Thesis

Submitted to the University of Warwick

for the degree of

Doctor of Philosophy

Physics

April 2010

THE UNIVERSITY OF WARWICK

Contents

List of Tables

List of Figures

Acknowledgments

I would like to thank my supervisor Bogdan Hnat for his help, support and flexibility during my time at Warwick. I am very grateful to Richard Dendy for his insight, advice and encouragement over the past three and a half years.

Thank you S Masuzaki, T Morisaki, N Ohno, H Tsuchiya and A Komori for the friendliness and hospitality which made my visit to NIFS such a great experience.

Thank you to everyone at CFSA, especially Francis Casson and Chris Brady for help with computational problems.

I'd like to acknowledge the continuing support and advice from my parents and grandmother. To my in-laws, the Nakamuras, I am extremely grateful.

Finally, I'd like to thank my wife Michiko for her love and support.

To Michiko

Abstract

In tokamaks, heat and particle fluxes reaching the wall are often bursty and intermittent and understanding this behaviour is vital for the design of future reactors. Plasma edge turbulence plays an important role, its quantitative characterisation and modelling under different operating regimes is therefore an important area of research.

Ion saturation current (I_{sat}) measurements made in the edge region of the Large Helical Device (LHD) and Mega-Amp Spherical Tokamak (MAST) are analysed. Absolute moment analysis is used to quantify properties on different temporal scales of the measured signals, which are bursty and intermittent. In all data sets, two regions of power-law scaling are found, with the temporal scale $\tau \approx 40\mu$s separating the two regimes. A monotonic relationship between connection length and skewness of the probability density function is found for LHD.

A new numerical code, 'HAWK,' which solves the Hasegawa-Wakatani (HW) equations is presented. The HAWK code is successfully tested and used to study the HW model and modifications. The curvature-Hasegawa-Wakatani (CHW) equations include a magnetic field strength inhomogeneity, $C = -\partial \ln B/\partial x$. The zonal-Hasegawa-Wakatani (ZHW) equations allow the self-generation of zonal flows. The statistical properties of the turbulent fluctuations produced by the HW model and variations thereof are studied. In particular, the probability density function of $E \times B$ density flux $\Gamma_n = -n\partial\phi/\partial y$, structure functions, the bispectrum and transfer functions are investigated.

Test particle transport is studied. For the CHW model, the conservation of potential vorticity $\Pi = \nabla^2\phi - n + (\kappa - C)x$ accounts for much of the phenomenology. Simple analytical arguments yield a Fickian relation $\Gamma_n = (\kappa - C)D_x$ between the radial density flux Γ_n and the radial tracer diffusivity D_x. For the ZHW model, a subtle interplay between trapping in small scale vortices and entrainment in larger scale zonal flows determines the rate, character and Larmor radius dependence of the test particle transport. When zonal flows are allowed non-Gaussian statistics are observed. Radial transport (across the zones) is subdiffusive and decreases with the Larmor radius. Poloidal transport (along the zones), however, is superdiffusive and increases with small values of the Larmor radius.

Chapter 1

Introduction

1.1 Thermonuclear fusion

The world's energy requirements are rapidly increasing as the global population rises and nations become more industrialised. With growing concerns over the finite size of the world's fossil fuel supplies and their contribution to climate change, the need for a clean, safe, carbon-neutral and politically-neutral form of electricity generation is clear. Controlled thermonuclear fusion has long been recognised as an ideal solution.

Fusion is the process that powers the Sun. During the reaction, nuclei fuse together and the mass of the reaction products is less than the mass of the reactants. Due to this small mass loss, and Einstein's famous mass-energy equivalence $E = mc^2$, energy is released. The fusion of nuclei relies on the nuclear force, which is attractive on very small spatial scales; nuclei, however, are positively charged and experience mutual electrostatic repulsion. Thus for the fusion reaction to proceed, an electrostatic potential barrier must be overcome.

The size of the potential barrier depends on the reactants. It is conventional to work in terms of a reaction cross-section, which measures the likelihood of a reaction. Some cross-sections for candidate reactions are shown in figure 1.1. The most promising reaction with the highest cross-section is deuterium-tritium (D-T) at an energy of

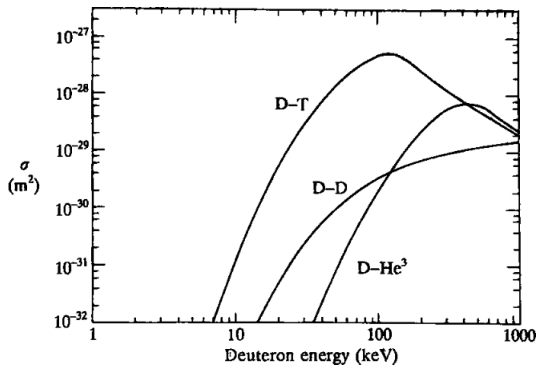

Figure 1.1: Cross sections for various fusion reactions [Wesson, 2004].

100keV. The reaction is as follows,

$$\mathrm{D} + \mathrm{T} \rightarrow \alpha(3.5\mathrm{MeV}) + \mathrm{n}(14\mathrm{MeV}) \ ; \tag{1.1}$$

D and T nuclei fuse together creating an alpha particle and a neutron, and releasing 17.5 MeV of energy. Deuterium and tritium are relatively abundant–deuterium is found in sea water while tritium can be bred from lithium–and will therefore be the fuel of choice for the first generation of fusion reactors. It is important to note that, unlike in nuclear fission, the fusion reaction cannot lead to a catastrophic runaway event and produces little radioactive waste. In fact, small quantities of short-lived radioactive waste would be produced indirectly due to the activation of the device by neutron bombardment.

Thermonuclear fusion occurs when the fuel is heated sufficiently so that the thermal velocities of the particles are large enough to produce the required fusion reactions. The optimum temperature for D-T thermonuclear fusion is around 30keV, less than the 100keV peak in figure 1.1 since a significant fraction of the fusion reactions can occur in the high energy tail of the Maxwellian [Wesson, 2004]. At such high temperatures, the fuel will be a fully ionised plasma.

To produce significant amounts of energy, sufficient amounts of the plasma fuel must be confined for a sufficiently long time. In other words, the product of the density of fusing nuclei n and the time-scale of confinement τ_e must be large. This energy confinement time is defined as $\tau_e = W/P$, where W is the energy content of the

plasma and P is the rate of energy loss. The plasma is said to reach ignition when all energy losses are balanced by alpha particle heating and no external energy inputs are needed to maintain the fusion reaction. The relevant criterion was derived by Lawson and expressed in terms of $n\tau_e$. At a temperature of 30keV, the Lawson criterion for ignition is

$$n\tau_e > 1.5 \times 10^{20}\text{sm}^{-3} \ . \tag{1.2}$$

There are generally two approaches to satisfying this inequality: inertial confinement and magnetic confinement. Inertial confinement involves the rapid compression of small fuel pellets using high powered lasers, aiming for extremely high values of n and short τ_e. Magnetic confinement, which this thesis is concerned with, takes advantage of the charge of plasma particles and attempts to design a magnetic field to confine plasma at relatively low n and for long τ_e.

1.2 Plasma

A plasma is an ionised gas or, more accurately, "a quasi-neutral collection of ions and electrons which exhibits collective behaviour" [Chen, 1984]. In a plasma, electrons are much more mobile than ions due to their lower mass. Thus any charge imbalance is quickly screened out by the rapid movement of electrons, so that the bulk of the plasma can be considered neutral; this is quasi-neutrality. The length scale over which charge imbalance is screened out is called the Debye length,

$$\lambda_D = \left(\frac{\epsilon_0 T_e}{ne^2}\right)^{\frac{1}{2}} \ , \tag{1.3}$$

where n is number density, T_e is electron temperature and all other quantities are constants. In plasma physics, temperature is conventionally measured in energy units so that the Boltzmann constant k_B is suppressed in the preceding and all following formulae. The time scale over which electrons move to screen out charge imbalance is

$1/\omega_{pe}$, where

$$\omega_{pe} = \left(\frac{ne^2}{m_e \epsilon_o}\right)^{\frac{1}{2}} = \left(\frac{T_e}{m_e}\right)^{\frac{1}{2}} \frac{1}{\lambda_D} \ , \tag{1.4}$$

is the plasma frequency. For quasi-neutrality λ_D must be small compared to the system size and $1/\omega_{pe}$ must be small compared to the collision time. Also, the plasma must be dense enough so that charge imbalance is screened effectively, this condition can be written,

$$n\lambda_D^3 \gg 1 \ . \tag{1.5}$$

This also ensures collective behaviour because it implies that plasma particles interact with a large number of others.

1.3 Charged particle motion in electromagnetic fields

On a small scale, a plasma can be understood as a soup of charged particles which react to, and generate electromagnetic fields. A particle of charge q and mass m, moving with velocity $\mathbf{v}$ in an electric field $\mathbf{E}$ and magnetic field $\mathbf{B}$ experiences a Lorentz force,

$$\mathbf{F}_L = q(\mathbf{E} + \mathbf{v} \times \mathbf{B}) \ . \tag{1.6}$$

In the absence of an electric field and with a uniform magnetic field, the motion of the particle consists of a uniform velocity parallel to $\mathbf{B}$ and gyration perpendicular to $\mathbf{B}$ with cyclotron (or gyro) frequency

$$\omega_c = \frac{qB}{m} \ , \tag{1.7}$$

and Larmor radius

$$\rho = \frac{mv_\perp}{qB} \ , \tag{1.8}$$

where $v_\perp$ is the component of velocity perpendicular to $\mathbf{B}$. Thus the particle moves along a helical path. This type of motion can be thought of as rapid gyration around a guiding centre which moves at constant velocity parallel to $\mathbf{B}$. Such a circulating charge constitutes a current loop with magnetic moment,

$$\mu = \frac{mv_\perp^2}{2B} \ . \tag{1.9}$$

If in addition to the magnetic field, the particle feels an electric field $\mathbf{E}$, the guiding centre of the particle will drift with the so-called '$E \times B$ velocity',

$$\mathbf{v_E} = \frac{\mathbf{E} \times \mathbf{B}}{B^2} \ , \tag{1.10}$$

which is perpendicular to both $\mathbf{E}$ and $\mathbf{B}$. The $E \times B$ velocity is the most fundamental of the plasma particle guiding centre drifts and plays a central role in the physics of magnetic confinement. Guiding centre drifts are created whenever plasma particles are subject to a force $\mathbf{F}$ in the presence of a strong magnetic field $\mathbf{B}$,

$$\mathbf{v_F} = \frac{1}{q}\frac{\mathbf{F} \times \mathbf{B}}{B^2} \ . \tag{1.11}$$

In the above $E \times B$ example, the particle experiences a force $\mathbf{F} = q\mathbf{E}$ due to the electric field and equation 1.11 reduces to equation 1.10. Guiding centre drifts are also produced by non-uniform and time varying electromagnetic fields, for example the polarisation drift $\mathbf{v}_p$ is produced by a time varying electric field,

$$\mathbf{v}_p = \pm\frac{1}{\omega_c B}\frac{d\mathbf{E}}{dt} \ . \tag{1.12}$$

One important plasma drift is the diamagnetic drift,

$$\mathbf{v}_d = -\frac{\nabla p \times \mathbf{B}}{qnB^2} \ . \tag{1.13}$$

This drift is not a particle drift: individual particles do not actually drift with $\mathbf{v}_d$. The diamagnetic drift is a fluid drift which arises due to the fluid-like nature of a plasma. The left hand side of figure 1.2 shows the orbits of plasma particles gyrating in a magnetic field. The plasma is inhomogeneous, with a density gradient pointing from right to left. As illustrated in the right hand side of figure 1.2, through any fixed volume of plasma there are more particles gyrating downwards than upwards. Thus there is a net drift of particles perpendicular to the magnetic field and density gradient.

The motion of charged particles is affected by imposed magnetic fields and guiding centre drifts. But moving charged particles generate their own magnetic fields which affect the motion of other particles. It is clear that magnetically confining a plasma is a self-consistent problem.

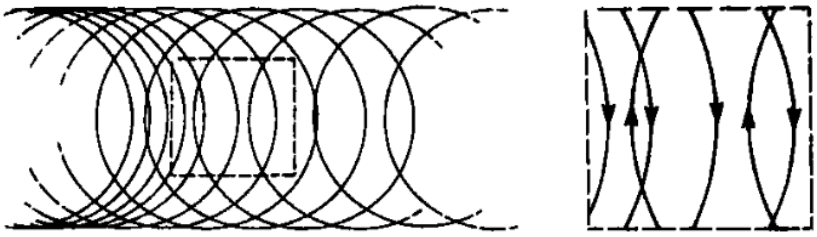

Figure 1.2: Origin of the diamagnetic drift [Wesson, 2004].

1.4 Kinetic description of plasma

In most physically relevant situations it is not feasible to follow the individual motions of each plasma particle, and a statistical approach must be taken. The Vlasov equation treats plasma as a phase space continuum and describes the time evolution of the distribution function $f(\mathbf{r}, \mathbf{v}, t)$ of a single plasma species in the presence of averaged electric and magnetic fields and in the absence of collisions. The Vlasov equation can be derived from first principles by considering individual particle motions in electric and magnetic fields [Clemmow and Dougherty, 1969]. When collisions are included, the equation becomes the Boltzmann equation,

$$\frac{df}{dt} = \frac{\partial f}{\partial t} + \mathbf{v} \cdot \nabla f + \frac{q}{m} (\mathbf{E} + \mathbf{v} \times \mathbf{B}) \cdot \frac{\partial f}{\partial \mathbf{v}} = \left(\frac{\partial f}{\partial t} \right)_{\text{coll}} = C(f, f) \ , \tag{1.14}$$

where $C(f, f)$ is the collision operator and contains terms due to collisions with both like-species and other species. This equation is six-dimensional (three space and three velocity) and is therefore difficult to handle numerically and analytically. When the evolution of f is small on spatial scales compared to the Larmor radius and slow on time scales compared to the gyroperiod, the Boltzmann equation can be reduced to the five-dimensional drift-kinetic equation [Wesson, 2004]. Alternatively, averaging over the rapid gyration of particles around magnetic field lines gives the five-dimensional gyrokinetic equation. The gyrokinetic equation is generally used in the most advanced models relevant to magnetically confined fusion plasmas.

1.5 Fluid description of plasma

It is often sufficient to describe a plasma by average quantities such as the number of particles of a given species per unit volume n, the mean velocity of these particles $\mathbf{u}$ and the mean temperature T. Such fluid equations were derived by Braginskii by taking moments of the Boltzmann equation [Braginskii, 1965]. In the two fluid model, ions and electrons are treated as two separate but interpenetrating fluids which interact with each other via electromagnetic fields. Each species has an equation for continuity

$$\frac{\partial n}{\partial t} + \nabla \cdot (n\mathbf{u}) = 0 \ , \tag{1.15}$$

momentum

$$mn\left(\frac{\partial}{\partial t} + \mathbf{u}\cdot\nabla\right)\mathbf{u} = nq(\mathbf{E} + \mathbf{u}\times\mathbf{B}) - \nabla p - \nabla\cdot\Pi + \mathbf{R} \ , \tag{1.16}$$

and energy

$$\frac{3}{2}n\left(\frac{\partial}{\partial t} + \mathbf{u}\cdot\nabla\right)T = -p\nabla\cdot\mathbf{u} - \nabla\cdot\mathbf{q} - \Pi : \nabla\mathbf{u} + Q \ . \tag{1.17}$$

Here, $p = nT$ is the scalar pressure, Π is the traceless component of the pressure tensor, $\mathbf{R}$ is the transfer of momentum from other species, $\mathbf{q}$ is the heat flux, Q is the heat exchange between species and the colon notation denotes the vector inner product. The plasma variables are coupled to electromagnetic fields which satisfy

$$\nabla\cdot\mathbf{E} = 0 \ , \tag{1.18}$$

$$\nabla\cdot\mathbf{B} = 0 \ , \tag{1.19}$$

$$\nabla\times\mathbf{E} = -\frac{\partial\mathbf{B}}{\partial t} \ , \tag{1.20}$$

$$\nabla\times\mathbf{B} = \mu_0\mathbf{J} \ , \tag{1.21}$$

where $\mathbf{J}$ is current density, charge density is zero because of quasi-neutrality and the displacement current can be neglected on the slow time scales of interest, i.e. we are not concerned with high frequency electromagnetic radiation. Taking moments of the gyrokinetic equation, instead of the Boltzmann equation, gives gyrofluid equations.

Often, it is too computationally expensive to numerically solve the full two fluid Braginskii equations and many reduced models have been developed. In this thesis one such model, namely the Hasegawa-Wakatani model [Hasegawa and Wakatani, 1983], is extensively studied; see Chapter 3.

1.6 Magnetohydrodynamic equilibrium

One of the most successful ways of dealing with a plasma is treating it as a single electrically neutral conducting fluid; this is magnetohydrodynamics (MHD). The MHD equations can be derived by summing the Braginskii two fluid equations and thus represent a further simplification to the description of a plasma. Ideal MHD assumes zero resistivity and the equations can be written,

$$\frac{\partial \rho}{\partial t} + \nabla \cdot (\rho \mathbf{u}) = 0 \ , \tag{1.22}$$

$$\rho \frac{d\mathbf{u}}{dt} = \mathbf{J} \times \mathbf{B} - \nabla p \ , \tag{1.23}$$

$$\mathbf{E} + \mathbf{u} \times \mathbf{B} = 0 \ , \tag{1.24}$$

where ρ is mass density [Dendy, 1990]. The equations are closed with an equation of state, Ampère's law (equation 1.21) and Faraday's law (equation 1.20).

MHD describes the large scale, bulk dynamics of a magnetised plasma and is thus used in the study of plasma equilibrium and stability. Using the force balance equation (equation 1.23), the conducting fluid will be at equilibrium when pressure gradients are balanced by the Lorentz force,

$$\nabla p = \mathbf{J} \times \mathbf{B} \ . \tag{1.25}$$

Slowly varying (time scales comparable to τ_e) confined plasma configurations are usually well approximated by solutions to this equation [Biskamp, 1993]. It implies that p must be constant along lines of $\mathbf{J}$ and $\mathbf{B}$, so a spherical reactor with isobars on nested spheres would not satisfy Ampère's Law (equation 1.21). In fact, the simplest geometry which satisfies equation 1.25 and Ampère's Law is toroidal. A torus is a doughnut shape (see

figure 1.3) and is characterised by the major radius R and minor radius a; the ratio R/a is called the aspect ratio. There are two directions around a torus: the long, toroidal way around ϕ and the short, poloidal way around θ. Thinking naively, a plasma

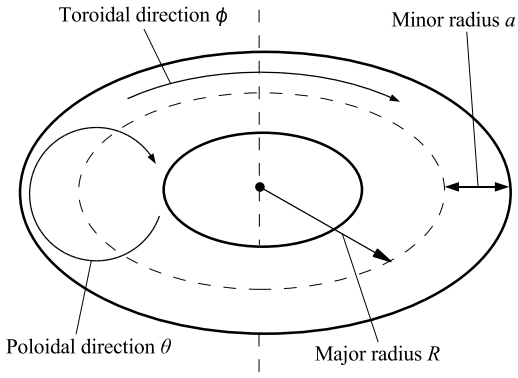

Figure 1.3: The torus.

might be confined by driving a current through the hole of a torus, along the axis of symmetry thus producing a purely toroidal magnetic field. However, in such a situation the particles, following magnetic field lines, move in circles and therefore experience a centrifugal force. Such a force generates a guiding centre drift according to equation 1.11; a guiding centre drift is also produced by the non-uniform magnetic field strength (falling off with the major radius as $1/R$). These two drifts happen to be in the same direction and can be written together as

$$\mathbf{v}_d = \frac{m}{q}\left(v_\parallel^2 + \frac{1}{2}v_\perp^2\right)\frac{\mathbf{R}_c \times \mathbf{B}}{R_c^2 B^2}\ , \tag{1.26}$$

where $\mathbf{R}_c$ is the radius of curvature and $v_\parallel$ is the component of velocity parallel to the magnetic field. Since $\mathbf{v}_d$ is charge dependent, its direction is opposite for ions and electrons: depending on the direction of the magnetic field, one species drifts up while the other drifts down. This generates an electric field and associated $E \times B$ drift velocity in the direction perpendicular to $\mathbf{B}$ (equation 1.10) and the plasma particles are lost.

The solution is to generate a poloidal magnetic field as well as toroidal so that the total magnetic field has a helical shape. Then the up-down charge asymmetry can

be short-circuited by rapid motion along field lines. There are two leading approaches to generating such a helical magnetic field: the tokamak and the stellarator; see figure 1.4.

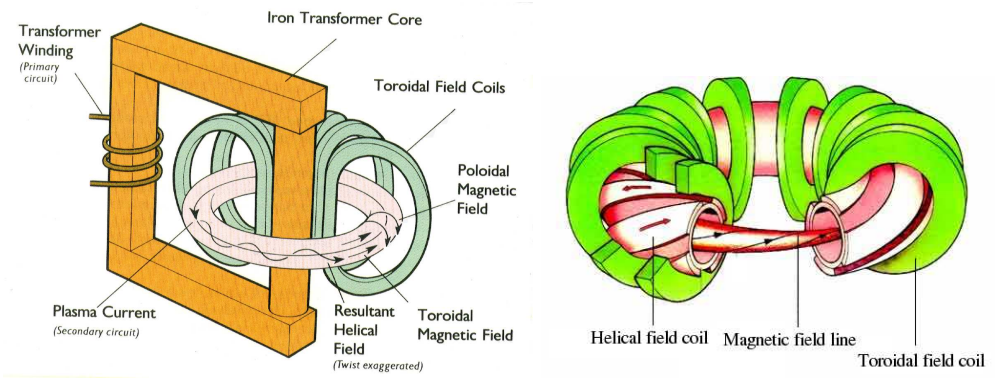

Figure 1.4: Principle of the tokamak [Pecseli, 2009] (left) and stellarator [ENS, 2009] (right).

1.6.1 Stellarator

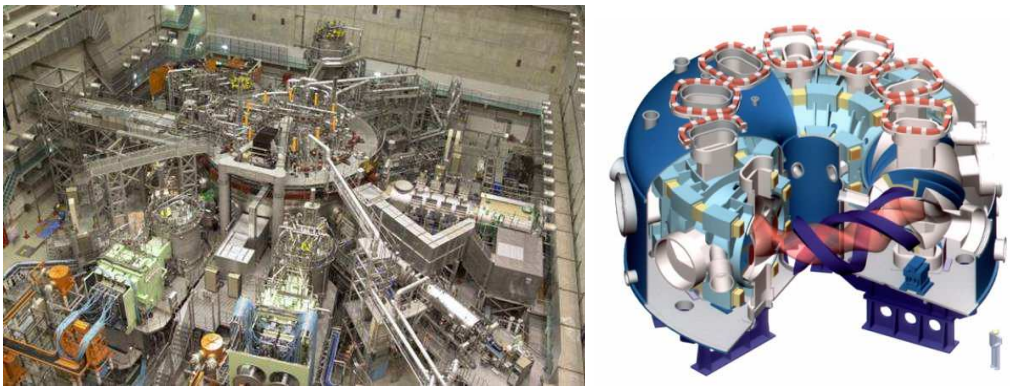

Figure 1.5: The Large Helical Device (LHD) stellarator [NIFS, 2009].

The stellarator was originally proposed by Spitzer in the early 1950s, twisted field coils are used to produce the desired magnetic field. Steady state operation is easily achieved, however their complexity makes stellarators challenging for theoreticians and engineers alike. Currently, the largest stellarator experiment is the Large Helical Device

(LHD), located at the National Institute for Fusion Studies (NIFS) in Japan. LHD is a heliotron type stellarator with major radius $R = 3.9$m, minor radius $a = 0.65$m and superconducting field coils generating a magnetic field strength of typically 2.5T. Pictures of LHD are shown in figure 1.5; in the diagram on the right the helical shape of plasma can be seen in pink. The statistical analysis of experimental data taken from LHD forms part of Chapter 2 of this thesis.

1.6.2 Tokamak

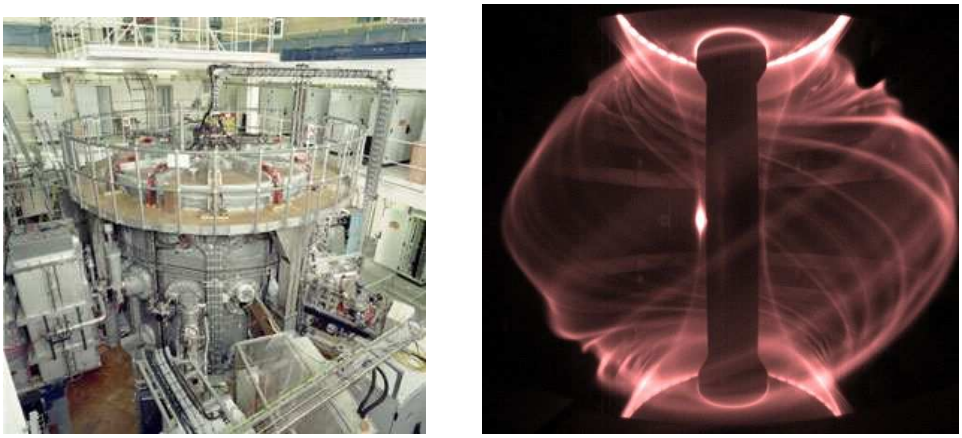

Figure 1.6: External (left) and internal (right) photographs of the Mega-Amp Spherical Tokamak (MAST) [CCFE, 2009].

The tokamak was originally developed in Russia in the late 1950s. The word 'tokamak' is a transliteration of a Russian acronym, meaning "toroidal chamber with magnetic coils." In tokamaks, a poloidal field is generated by driving a current toroidally through the plasma using transformer action. This has the additional benefit of Ohmically heating the plasma, however the process is inherently pulsed and can lead to current driven instabilities. Conventionally, tokamaks have an aspect ratio much greater than one, i.e. their major radius is much larger than their minor radius. Tokamaks with an aspect ratio close to one are referred to as spherical tokamaks (ST). The Mega-Amp Spherical Tokamak (MAST), located at Culham in Oxfordshire, is a leading ST exper-

iment with major radius $R = 0.7$m, minor radius $a = 0.5$ and a typical magnetic field strength of 0.5T; photographs are shown in figure 1.6. The shape of a typical MAST plasma can be seen in the right hand image: due to its low aspect ratio the plasma resembles a cored apple, rather than the doughnut shape associated with conventional tokamaks. The statistical analysis of experimental data from MAST and comparison with LHD forms Chapter 2 of this thesis.

The helicity of the magnetic field in a tokamak is quantified by the safety factor,

$$q = \frac{a}{R}\frac{B_\phi}{B_\theta} \ . \tag{1.27}$$

It is the number of times the magnetic field goes around toroidally per poloidal rotation. Stellarator physics typically uses $1/q$, the rotational transform. In tokamaks, the safety factor must be larger than one everywhere for stability. A safety factor less than one in the central region is associated with an MHD instability called the sawtooth oscillation. The ratio of plasma pressure to magnetic field pressure is an important quantity β,

$$\beta = \frac{p}{B^2/2\mu_0} \ . \tag{1.28}$$

Commercial fusion reactors require $\beta > 1\%$ in order to be economically viable since the the fusion energy output scales with some power of p while the cost of the device depends mainly on the size of the magnetic field coils and scales with some power of B [Chen, 1984].

Currently, the conventional tokamak is the most highly developed design, and on 21st November 2006 officials agreed to fund the creation of the ITER tokamak with the aim of demonstrating ignition for the first time in a magnetically confined plasma.

1.6.3 Edge plasma

The hot plasma required for magnetic fusion must be kept away from the vessel wall in order to prevent melting of the wall and disruption of the plasma. A common way to limit tokamak plasmas is to use a divertor. In this configuration, extra field coils are used in order to create a region of closed magnetic field lines surrounded by open

	LHD	MAST
Major radius, R	3.9m	0.7m
Minor radius, a	0.65m	0.5m
Plasma volume	30m^3	8m^3
Magnetic field strength	2.5T	0.5T
Maximum discharge length	1 hour	1s

Table 1.1: Typical parameters for LHD and MAST.

field lines which are connected to a divertor plate designed to handle large heat and particle fluxes, see figure 1.7. The closed field lines lie on 'flux surfaces' which, in a tokamak, form concentric tori. The last flux surface, radially, on which field lines are closed is called the 'last closed flux surface' (LCFS) and is commonly used to define the plasma edge. The region where field lines are open is referred to as the 'scrape-off layer' (SOL). The magnetic field geometry of stellarators is much more complex, the core region where field lines are closed is surrounded by an 'ergodic layer' where field lines wrap around the device to fill a volume. The edge region of a magnetically confined plasma is thus extremely complicated, containing large pressure gradients and complex magnetic geometry. Considerable numerical and theoretical effort is focused on trying to understand this region.

The edge region plays an important role in the confinement of the whole plasma. For example, in many diverted tokamak plasmas two main confinement regimes, the L-mode and H-mode, have been found (H stands for high confinement, L stands for low). Under certain operating conditions, confinement suddenly improves from L-mode to H-mode and large temperature and density gradients build up near the plasma edge; this can be thought of as the creation of a transport barrier. The H-mode is usually accompanied by the periodic crashing of the edge gradients. This relaxation process, known as the edge-localised mode (ELM), can cause damage to the device due to intense heat loads [Biskamp, 1993] [Wesson, 2004]. The ITER tokamak has been designed to achieve ignition in H-mode and many ELM mitigation techniques have been proposed. An ignited device operating in L-mode would be much larger and therefore more expensive.

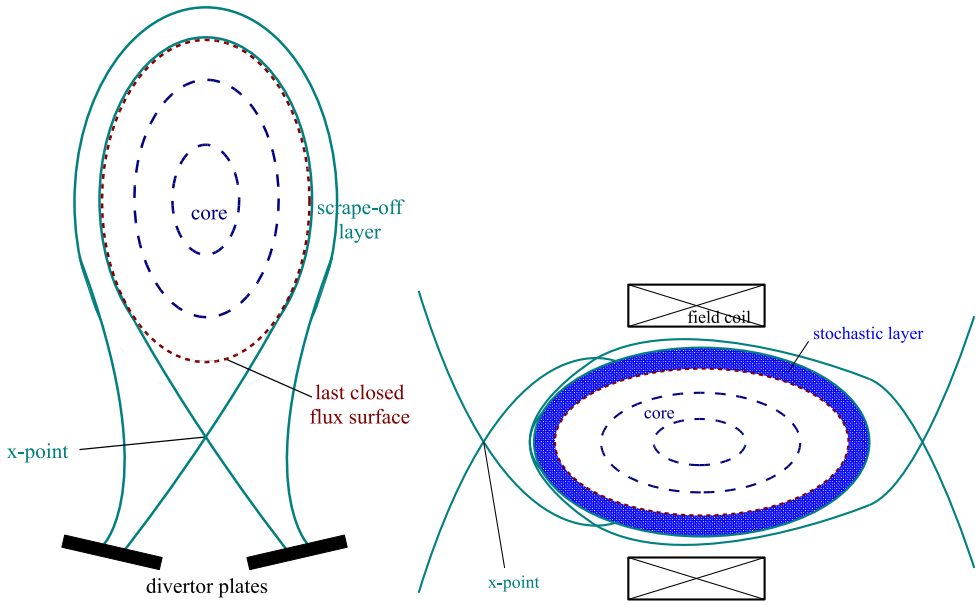

Figure 1.7: Simplified magnetic field structure of a diverted tokamak (left) and heliotron type stellarator (right).

The transition from L-mode to H-mode is not fully understood though it is thought to be related to the suppression of edge turbulence by shear flow. It has been observed that the L-H transition is accompanied by a reduction in turbulent density fluctuations in the region of the transport barrier; this gives evidence that the reduction of turbulence causes the reduction in transport. The mechanism for the reduction of turbulence could be as follows. As edge gradients build up close to the plasma edge, more ions are lost than electrons because of their larger Larmor radius and a negative radial electric field is created. Equation 1.10 tells us that a radial electric field will generate a poloidal drift velocity. Experimentally, an increase in the radial field is observed in the narrow transport barrier region. This means that the total radial electric field is strongly inhomogeneous and the generated poloidal velocity will be sheared. A poloidal shear flow can suppress turbulence by tearing turbulent eddies apart or by consuming some of the turbulent energy [Biskamp, 1993] [Wesson, 2004] [Diamond et al., 2005].

1.7 Classical transport

1.7.1 Classical transport

So far in this introduction to magnetic confinement, collisions between plasma particles have been ignored. In the presence of collisions, particles experience stochastic forces and therefore perform random walks. Collisions cause a resistance to the flow of current and their effect can be understood in the context of MHD by introducing a resistivity η in equation 1.24,

$$\mathbf{E} + \mathbf{u} \times \mathbf{B} = \eta \mathbf{J} \ . \tag{1.29}$$

Taking the cross product with $\mathbf{B}$ and using equation 1.25 we obtain,

$$\mathbf{u}_\perp = \frac{\mathbf{E} \times \mathbf{B}}{B^2} - \frac{\eta_\perp}{B^2} \nabla p \ . \tag{1.30}$$

The first part of this velocity is the $E \times B$ drift that was seen earlier (equation 1.10). The second part is in the $-\nabla p$ direction which is perpendicular to the confining magnetic field. Thus collisions cause a cross-field transport of plasma particles down the pressure gradient, i.e. collisions cause a reduction in the level of confinement. The flux associated with the velocity is

$$\mathbf{\Gamma}_\perp = n\mathbf{u}_\perp = -\frac{n\eta_\perp}{B^2} \nabla p = -\frac{n\eta_\perp T}{B^2} \nabla n \ . \tag{1.31}$$

This is like Fick's law with diffusion coefficient

$$D_\perp = \frac{n\eta_\perp T}{B^2} \ . \tag{1.32}$$

This type of diffusion, caused by particle collisions, is referred to as classical diffusion or classical transport. In general a diffusion coefficient is of the form

$$D \sim \frac{(\triangle x)^2}{\triangle t} \ , \tag{1.33}$$

where $\triangle x$ is a mean spatial step size and $\triangle t$ is a mean step time. In this case, the step size is the Larmor radius ρ and the step time is the electron collision time.

1.7.2 Neoclassical transport

Geometric effects can cause an increase to the level of classical transport and this is referred to as neoclassical transport. For example, the magnetic mirror effect leads to neoclassical banana diffusion. Consider a charged particle in a magnetic field B. It can be shown that the magnetic moment μ is constant for B varying slowly in space or time, in other words μ is adiabatically invariant. This leads to the magnetic mirror effect in the following way. By the definition of μ (equation 1.9), if the particle moves into a region of higher B, $v_\perp$ must increase in order to keep μ constant. Since the total energy of the particle is constant and can be written as

$$E = \frac{mv_\parallel^2}{2} + \frac{mv_\perp^2}{2} \ , \tag{1.34}$$

an increase in $v_\perp$ must be accompanied by a decrease in $v_\parallel$. If B is large enough, there will come a point when $v_\parallel$ goes to zero and the particle is reflected. In tokamaks, the magnetic field strength falls off with the major radius as $1/R$ so that it is higher on the inboard side (near the axis of symmetry) than the outboard side. Thus particles moving in helical orbits experience an increase in magnetic field strength as they move from the outboard side to the inboard side. Particles with insufficient energy will be reflected and trapped in 'banana orbits.' Particles with sufficient energy to complete a full circuit around the tokamak are called passing particles. For the fraction of particles that are trapped in non-circulating 'banana orbits,' the step time $\triangle t$ and step size $\triangle x$ of equation 1.33 become the banana orbit period and width respectively and thus diffusion is increased to neoclassical levels. Other neoclassical effects lead to plateau and Pfirsch-Schluter diffusion [Wesson, 2004].

1.8 Turbulent transport

Neoclassical theory is highly developed, however, experimentally measured transport rates are almost always orders of magnitudes higher than those predicted by it. This

extra transport is referred to as anomalous transport and is generally attributed to the presence turbulence generated by small scale instabilities.

1.8.1 Turbulence

Turbulence is a state of fluid motion characterised by unpredictability over a wide range of temporal and spacial scales. It is often referred to as the last great unsolved problem of classical physics since the governing equations are deterministic and have been studied since the 19th century. Here, we introduce the phenomenology of hydrodynamic turbulence though this is not necessarily a good model for plasma turbulence.

In fluids dynamics a control parameter, called the Reynolds number, can be derived from a simple balance of nonlinear and dissipative terms in the momentum equation,

$$Re = \frac{vL}{\nu} \ , \tag{1.35}$$

where v is a typical fluid velocity, L is a typical length scale and ν is viscosity in the system. Transition from laminar to turbulent flow occurs for large values of Re in hydrodynamics. Similar parameters are often used for magnetised plasmas where one can define the Reynolds number Re and its magnetic counterpart Rm [Biskamp, 1993]. It is important, however, to recognise that these constructs are not identical due to non-diffusive dissipation processes such as Landau damping which act on scales much smaller than the actual collisional dissipation.

The Richardson-Kolmogorov view of three-dimensional hydrodynamic turbulence is a fluid breaking up into large eddies due to instability in the mean flow. These eddies are themselves subject to instability and break up into smaller eddies which also break up and so on. Thus there is an energy cascade from large to small scale. At some very small scale, when $Re \sim 1$, viscosity becomes important and energy is dissipated. The scales at which the cascade occurs k are referred to as the 'inertial range,' $k_i \ll k \ll k_d$, where k_i is the energy injection scale and k_d is the dissipation scale. In order for the turbulence to be stationary, the rate of energy injected must be equal to the rate of

energy dissipated.

Applying critical balance–a scale-by-scale balance between the linear propagation and nonlinear interaction time scales–to isotropic, homogeneous and incompressible turbulence, Kolmogorov famously found that the integrated energy spectrum $E(k)$ in the inertial range should depend on wave number k as $E(k) \sim k^{-5/3}$ [Frisch, 1995]. In the limit of large Re and for time stationary turbulence, the cascade process is unaware of the driving and dissipation mechanisms. Thus its physics is universal and can be characterised, in the simplest case, by a constant energy transfer rate, ϵ. In such a case, fluctuations in the velocity field are self similar, that is they obey a simple scaling relation $du(lx) = l^H du(x)$, where H is the scaling exponent. In other words, fluctuations are statistically self-similar under dilation of the spatial scale l. In reality, the energy transfer rate ϵ can vary in space and time leading to intermittency, which is normally understood as departure of the scaling from the simplest Kolmogorov self-similar prediction. Attempts to include intermittency in Kolmogorov's theory have been made, see [Frisch et al., 1978] for example. Some attempts to obtain the energy spectrum in the plasma context are [Chen, 1965] and famously the Iroshnikov-Kraichnan spectrum for MHD turbulence which predicts $E(k) \sim k^{-3/2}$ [Biskamp, 1993].

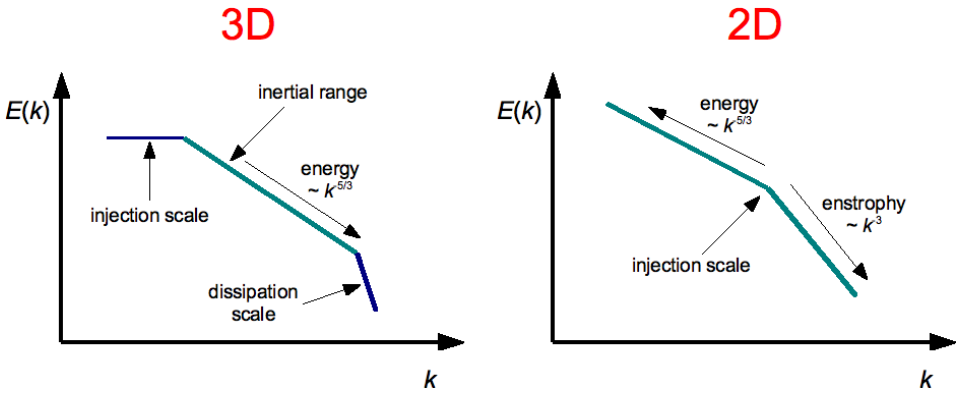

Figure 1.8: Cartoon of the energy spectrum $E(k)$ expected in 3-dimensional (left) and 2-dimensional (right) hydrodynamic turbulence.

In two-dimensional turbulence, which is expected to apply in magnetised plasmas,

the magnitude squared of the vorticity, 'enstrophy' $|\omega|^2$ is conserved. Vorticity is a quantity widely studied in fluid dynamics and is defined as the curl of velocity field $\omega = \nabla \times \mathbf{u}$. Kraichnan showed that this results in enstrophy cascading from large scales to small, in a 'direct cascade'. Energy, however, cascades in the opposite direction–from small scales to large–in a so-called 'inverse cascade' [Kraichnan, 1967]. This combination of inverse energy and direct enstrophy cascade is referred to as a dual cascade. The inverse cascade may lead to the formation of large scale structures, for example vortices and zonal flows. The sign of the third order moment indicates the direction of the turbulent cascade, but in practice this is difficult to measure [Atta and Antonia, 1980].

1.8.2 Wave-wave interaction

Turbulence can also be considered as a superposition of waves. Waves are driven by an underlying linear instability and the linear mode structure of the waves reflects the nature of the instability. When the linear instability has driven waves to sufficiently large amplitudes, waves may interact with each other through nonlinearity in the system. This wave-wave interaction acts to distribute energy in wave vector space, much like the cascade process described in the previous section. In the case of 'weak turbulence,' the nonlinear coupling between waves is weak and energy may be distributed in a relatively narrow range of wavevectors, leading to a broadening of the linear mode structure. In the case of 'strong turbulence,' waves interact strongly and the energy can be distributed to a broadband range of wavevectors, and the linear mode structure may be lost.

If the nonlinearity in the system is quadratic, energy can be distributed through three-wave interactions. In terms of a Fourier decomposition, modes with wavevectors $\mathbf{k}$, $\mathbf{k}_1$, $\mathbf{k}_2$ and frequencies ω, ω_1, ω_2 may interact if they satisfy the resonance condition $\mathbf{k} = \mathbf{k}_1 + \mathbf{k}_2$ and $\omega = \omega_1 + \omega_2$. The presence of such wave-wave interactions within a nonlinear system can be revealed through the study of higher order spectra. In Chapter 4, the bispectrum is used to reveal three wave interaction in the Hasegawa-Wakatani system.

1.8.3 Plasma instabilities

In magnetic confinement, pressure gradients are balanced by a strong magnetic field (see equation 1.25). These pressure gradients provide a source of free energy which can drive instabilities and cause turbulence. The turbulent motions can modify the original gradients due to nonlinear interactions:- we have returned to the notion of self-consistency. Instabilities on a macroscale, such as MHD instabilities, can cause a disruption to the plasma, i.e. the plasma confinement may be completely lost. Smaller scale microinstabilities (on the scale of the ion Larmor radius ρ_i) tend to degrade confinement by driving microscale turbulence. Two instabilities relevant to turbulent transport in the edge region of magnetically confined plasmas are the drift wave instability and the interchange instability. In the core region of the plasma, Ion Temperature Gradient (ITG) modes and Trapped Electron Modes (TEM) are the most important microinstabilities.

Interchange modes

In hydrodynamics, a Rayleigh-Taylor instability occurs if a fluid of density ρ_1 is supported by a fluid of density ρ_2 in the presence of gravity and $\rho_1 > \rho_2$. If $\rho_1 \leq \rho_2$, however, the system is stable. An analogous instability occurs in toroidal magnetised plasmas: the magnetic field acts as a fluid supporting a plasma fluid and 'gravity' is supplied by centrifugal force or by the curvature or non-uniformity of the magnetic field. Interchange modes are unstable in regions where the radius of curvature vector is anti-parallel to the pressure gradient vector: so-called regions of 'bad curvature.' In regions of 'good curvature,' the two vectors are parallel and interchange modes are stable. In tokamaks the curvature vector points outwards along the major radius, while the direction of the pressure gradient changes depending on location: on the inboard side ∇p points outwards and on the outboard side ∇p points inwards. Therefore, interchange modes are unstable on the outboard side of tokamaks and stable on the inboard. The fact that inboard and outboard sides of a tokamak are connected by helical field lines complicates the situation and leads to so-called 'ballooning modes.'

Drift waves

Drift wave instabilities act on the microscale and are thought to be responsible for the majority of anomalous transport in tokamaks. Drift waves are low frequency (compared to the ion cyclotron frequency ω_{ci}) waves which are driven by gradients in density or temperature. They are generally electrostatic in nature, $\mathbf{E} = -\nabla\phi$, and involve two fluid physics; the physics of drift waves is not present in MHD theory. The dynamics of the electron fluid parallel to magnetic field lines plays a crucial role in the phenomenology. To illustrate, we start with the Braginskii momentum equation (1.16) for electrons and simplify by neglecting electron inertia, viscosity, collisions and considering an isothermal and quasi-neutral ($n_e = n_i = n$) plasma. Then the electron fluid parallel equation of motion gives

$$\frac{\delta n}{n} = \frac{e\delta\phi}{T} \ . \tag{1.36}$$

This equation tells us that perturbations in density n are tied to perturbations in electrostatic potential ϕ due to the rapid streaming of electrons parallel to magnetic field lines; in this situation electrons are said to be 'adiabatic'.

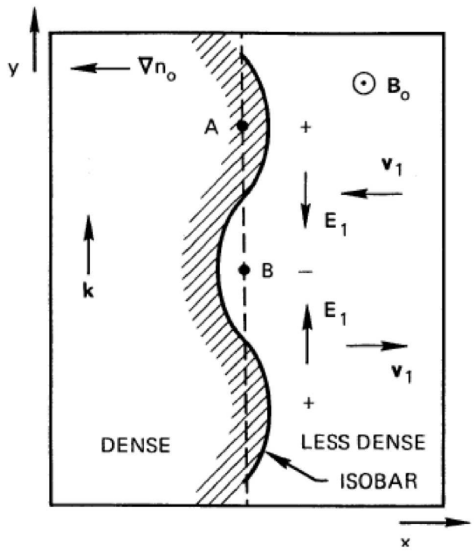

Figure 1.9: The physics of the drift wave. Adapted from [Chen, 1984].

Figure 1.9 shows a plasma in the plane perpendicular to a magnetic field $\mathbf{B}_0$, with a large scale density gradient ∇n_0 pointing in the negative x-direction. A small perturbation in density n is illustrated by a solid line which, due to equation 1.36, also corresponds to a perturbation in potential ϕ. Such a perturbation leads to an electric field, labelled $\mathbf{E}_1$, pointing from positive to negative potential and a corresponding $E \times B$ drift velocity, labelled $\mathbf{v}_1$. The direction of this $E \times B$ velocity varies along the perturbation such that the entire density perturbation is shifted in the positive y-direction. Thus a drift wave can propagate along $\mathbf{k}$, perpendicular to the magnetic field and density gradient.

When the electron parallel response is adiabatic (equation 1.36), the drift wave density and potential fluctuations are in phase and there is no net transport of density. If the electron response is not adiabatic, due to resistivity for example, potential and density fluctuations can become out of phase and drift waves become unstable. This is the drift wave instability which leads, through nonlinear coupling, to drift wave turbulence. When density and potential fluctuations are out of phase, there is an accompanying net flux of density which tends to transport plasma down the density gradient. In tokamaks, this turbulent transport of plasma is strongest in the edge region where gradients are large and is directed radially outwards, thus leading to a reduction of confinement.

1.9 Outline

In Chapter 2, a statistical analysis of density fluctuation data taken from LHD and MAST is presented. The measurements are made by Langmuir probes at the edge of the plasma where turbulence plays a dominant role and the time series are often highly nonlinear and intermittent. Statistical techniques suited to such time series, such as absolute moment analysis, probability density function and conditional averaging are employed. Significant differences are found in the statistics of data taken from three probes, separated by just 6mm, embedded in the divertor plate of LHD and comparison is made to MAST data. Analysis of the LHD data was originally published in [Dewhurst

et al., 2008].

In Chapter 3, a new numerical code developed from scratch by the author as part of this thesis is described. The code, called HAWK, is written in C and solves the Hasegawa-Wakatani equations in two dimensions. The Hasegawa-Wakatani equations form a simple model of drift-wave turbulence, which is thought to be dominant in the edge region of magnetically confined plasmas. Derivation of and modifications to the equations are discussed. The HAWK code is tested using appropriate tests and results of typical simulations are presented.

Chapter 4 presents a statistical analysis of data taken from the HAWK code. We focus on the probability density function of the turbulent flux and investigate the effects of changing the parameters in the Hasegawa-Wakatani model. Structure functions and higher order spectra are also used in order to gain insight into the physics of the model.

In Chapter 5, the results of test particle studies using the HAWK code are presented. The effect of non-uniform magnetic field strength on the transport of passive test particles is studied. An analytic expression linking test particle transport to turbulent flux, in the form of Fick's law, is also derived. A regime of non-diffusive transport is found and is shown to be associated with correlations in the turbulent flow. The effects of zonal flows and finite Larmor radius are also studied. It is found that a subtle interplay between trapping in small scale vortices and entrainment in larger scale zonal flows determines the rate, character and Larmor radius dependence of the test particle transport. When zonal flows are damped, the transport is classically diffusive, with Gaussian statistics, and the rate of transport decreases with increasing Larmor radius. Once the Larmor radius is larger than the typical radius of the turbulent vortices, the rate of transport remains roughly constant. When zonal flows are allowed non-Gaussian statistics are observed. Radial transport (across the zones) is subdiffusive and decreases with the Larmor radius at a slower rate. Poloidal transport (along the zones), however, is superdiffusive and increases with small values of the Larmor radius. This work was originally published in [Dewhurst et al., 2009] and [Dewhurst et al., 2010].

Chapter 2

Statistical description of LHD and MAST edge turbulence

This chapter concerns the statistical characterisation of experimental data measured by probes in the edge region of the Large Helical Device (LHD) stellarator and the Mega-Amp Spherical Tokamak (MAST). Parts of the chapter were published in *Statistical properties of edge plasma turbulence in the Large Helical Device*, J M Dewhurst, B Hnat, N Ohno, R O Dendy, S Masuzaki, T Morisaki and A Komori, Plasma Physics and Controlled Fusion **50**, 095013 (2008).

2.1 Introduction

Improved understanding of plasma transport in the edge and scrape-off layer (SOL) regions of magnetic confinement experiments is important for their design and operation. The ability to model and control plasma transport across the magnetic field in the SOL is critical for the optimal design of divertors and for predicting the lifespan of plasma facing components [LaBombard et al., 2001]. On a more fundamental level, edge and SOL physics influence core plasma transport, for example, through the level of impurities generated by plasma-wall interaction [Dux and Peeters, 2000].

Experimental data from transport studies indicate that the SOL cross-field transport is bursty and intermittent and that the probability distributions of fluctuations in plasma parameters are non-Gaussian, see for example [Zweben et al., 2007; Graves et al., 2005; Xu et al., 2005]. These features make any mean-value based model of SOL transport inaccurate and it is now recognised that a more complete picture must be built by examining higher order statistics. Interestingly, recent experimental evidence suggests that the edge and SOL transport has generic and scale invariant statistical properties which emerge in the functional forms of the probability density functions (PDFs) and the scaling of their higher moments [van Milligen et al., 2005; Antar et al., 2003; Dendy, 1990].

It is widely accepted that drift wave turbulence plays an important part in edge and SOL physics in all confinement systems [Horton, 1999]. Indeed, the bursty character of cross-field transport, dominated by density blobs has been identified in tokamaks and stellarators. While drift wave phenomenology is electrostatic in nature and thus not sensitive to magnetic fluctuations, the edge magnetic field structure could play an important role in some aspects of transport. Numerical simulations show that the inclusion of Alfvénic fluctuations in the drift wave model alters the mode compositions of turbulence and provides additional channels for energy dissipation via magnetic fluctuations [Kendl et al., 2000]. Careful comparison of the statistical features from edge and SOL measurements in tokamaks and stellarators may shed more light on the role of magnetic topology in cross-field transport. In this context, particularly interesting is the identification of generic features that may be shared by edge plasma turbulence in conventional and spherical tokamaks and in stellarators. This requires quantitative comparison of the the measured turbulence properties under different operating regimes for the full range of confinement systems, using modern techniques for the statistical analysis of nonlinear time series.

In this chapter, we analyse ion saturation current (I_{sat}) data taken from the edge region of LHD and MAST. In particular, we apply a novel statistical analysis

method, called absolute moment analysis, in order to quantify the scaling properties of the data. We also study the power spectral density, the probability density function and the conditional average. The rest of this chapter is organised as follows: in the next section the background statistical methods and concepts are introduced; in Section 2.3 the absolute moment analysis is introduced and tested using synthetic time series; analysis of the data is presented in Sections 2.4-2.7; and discussion and conclusions are given in Sections 2.8 and 2.9.

2.2 Statistical analysis background

2.2.1 Probability density function

The probability density function (PDF) of a random variable X, $P(x)$, is defined such that the probability that X lies within δx of x is $P(x)\delta x$. The nth order moment of $P(x)$ is defined as

$$m_n = \langle x^n \rangle = \int_{-\infty}^{\infty} x^n P(x)\, dx \ . \tag{2.1}$$

The $n = 1$th moment is the mean and moments about the mean are defined as

$$\mu_n = \langle (x - \langle x \rangle)^n \rangle = \int_{-\infty}^{\infty} (x - \langle x \rangle)^n P(x)\, dx \ . \tag{2.2}$$

The $n = 2$th moment about the mean is the variance, which measures the spread of $P(x)$ around the mean. The square root of variance is the standard deviation σ and standardised moments are normalised by the standard deviation,

$$M_n = \frac{\mu_n}{\sigma^n} \ . \tag{2.3}$$

The third and fourth order standardised moments are known as skewness, S, and kurtosis, K, respectively. Skewness is a measure of the asymmetry of a PDF; it is zero for symmetric PDFs, negative for negatively skewed PDFs and positive for positively skewed PDFs. Kurtosis is a measure of the 'peakedness' of a PDF or the influence of extreme outliers on the variance of a PDF. Skewness and kurtosis are often used to quantify the

departure of a PDF from Gaussian; the Gaussian PDF has skewness $S = 0$ and kurtosis $K = 3$.

2.2.2 Correlation

A joint PDF of two random variables X and Y, $P(x, y)$, can also be defined such that the probability that X lies within δx of x and Y lies within δy of y is $P(x, y)\delta x\delta y$. Covariance is defined as

$$\mathrm{cov}(X, Y) = \langle (x - \langle x \rangle)(y - \langle y \rangle) \rangle = \langle xy \rangle - \langle x \rangle \langle y \rangle \ , \tag{2.4}$$

and the correlation coefficient,

$$\mathrm{corr}(X, Y) = \frac{\langle (x - \langle x \rangle)(y - \langle y \rangle) \rangle}{\sigma_x \sigma_y} = \frac{\mathrm{cov}(X, Y)}{\sqrt{\mathrm{cov}(X, X)\mathrm{cov}(Y, Y)}} \ , \tag{2.5}$$

is a normalised measure of the degree of dependence of X and Y on each other. If X and Y are independent $\mathrm{corr}(X, Y) = 0$, if X and Y are are perfectly correlated $\mathrm{corr}(X, Y) = 1$ and if X and Y and perfectly anti-correlated $\mathrm{corr}(X, Y) = -1$.

Cross-correlation is a measure of the correlation between two functions offset with respect to each other by a certain lag τ. The cross-correlation of two discrete time series, $f(t)$ and $g(t)$, of length N samples is

$$R(\tau) = \frac{\sum_{t=1}^{N-\tau} [f(t) - \langle f(t) \rangle][g(t + \tau) - \langle g(t) \rangle]}{\sqrt{\sum_{t=1}^{N-\tau} [f(t) - \langle f(t) \rangle]^2} \sqrt{\sum_{t=1}^{N-\tau} [g(t) - \langle g(t) \rangle]^2}} \ . \tag{2.6}$$

Autocorrelation is the cross-correlation of a function with itself and is defined as

$$A_c(\tau) = \frac{\sum_{t=1}^{N-\tau} [f(t) - \langle f(t) \rangle][f(t + \tau) - \langle f(t) \rangle]}{\sum_{t=1}^{N-\tau} [f(t) - \langle f(t) \rangle]^2} \ . \tag{2.7}$$

2.2.3 Power spectral density

The square of the magnitude of Fourier modes is known as the energy spectral density. An alternative and often more useful measure is the power spectral density (PSD). The Wiener-Khinchin theorem states that the PSD is the Fourier transform of the

autocorrelation function. Several methods exist to estimate the PSD from finite time series; in this thesis, we employ the Thomson multitaper method [Thomson, 1982]. The PSD gives the proportion of a signal's power at a certain frequency; peaks in the PSD correspond to coherent modes in the time series. The PSD can be used to distinguish between different types of noise; correlated self-similar noise has a power law dependence $PSD(f) \sim f^{-\beta}$, uncorrelated random noise appears as constant power over all frequencies i.e. $\beta = 0$ [Dudson et al., 2005].

2.3 Absolute moment analysis

2.3.1 Turbulence and fractals

In the previous chapter, the concept of self-similarity was mentioned in the context of turbulence. In the idealised turbulent cascade, the system appears statistically identical on all inertial range scales, i.e. there is a fractal structure. Indeed, a fractal is an object that is invariant under some scale transformation. Self-similar fractals are invariant under isotropic scale transformations and can be described by a power law,

$$N(l) \propto l^{-d_F} \ , \tag{2.8}$$

where

$$d_F = \lim_{l \to 0} \frac{\ln N(l)}{\ln(1/l)} \ , \tag{2.9}$$

is a characteristic number called the fractal dimension.

Self-affine fractals are invariant under anisotropic scale transformations. E.g. for fractals described by a single-valued function, $h(x)$, the vertical rescaling is different to the horizontal rescaling: $x \to bx$, $h \to b^{\alpha}x$ and

$$h(x) \sim b^{-\alpha} h(bx) \ , \tag{2.10}$$

where α is the self-affine exponent and is a measure of the roughness of $h(x)$. In many cases the terms 'self-similar' and 'self-affine' are used interchangeably although strictly self-similarity is a special case of self-affinity.

Whereas self-affine fractals can be described by a single exponent, α, multi-affine fractals require an infinite set of exponents, α_m, to describe the scaling. If a surface is multi-affine, measurement of the mth order correlation function,

$$C_m \equiv <\mid h(x+\triangle x) - h(x) \mid^m>_x \ , \tag{2.11}$$

will give the scaling relation,

$$C_m \propto \triangle x^{m\alpha_m} \ , \tag{2.12}$$

where α_m varies with m. If α_m is independent of m, the object is self-affine. [Barabasi and Stanley, 1995].

For some fractals self-similarity holds exactly, i.e. when part of the fractal undergoes scale transformation it exactly overlaps the original; these are called deterministic fractals. Self-similarity may also hold in a statistical sense only; such objects are called random or statistical fractals [Barabasi and Stanley, 1995]. For example, a time series $x(t)$ is said to be self-similar if it obeys the equation,

$$\langle x(t+\triangle t) - x(t) \rangle = b^{-\alpha} \langle x(t+b\triangle t) - x(t) \rangle \ . \tag{2.13}$$

This equation implies the scaling relation,

$$\langle [x(t+\triangle t) - x(t)]^m \rangle \propto \triangle t^{m\alpha} \ . \tag{2.14}$$

If α is independent of m the time series is self-similar, if α varies with m it is multi-affine [Dudson et al., 2005].

2.3.2 Langmuir probes

Quantitative characterisation of plasma edge turbulence can be achieved with Langmuir probes. A Langmuir probe, in its simplest form, works by inserting an electrode into a plasma and applying a voltage with respect to the surrounding vessel. Measurement of the resulting current allows the determination of electron temperature T_e and density n_e. Langmuir probes are restricted to the edge of fusion plasmas due to the high

temperatures of the central regions. The current I to a probe biased at voltage V is given by,

$$I = J_i(1 - e^{e(V-V_f)/k_B T_e})A \ , \tag{2.15}$$

where J_i is the ion current density, A is the surface area of the probe and V_f is the floating potential (the applied potential at which current drops to zero) [Wesson, 2004].

If the probe is sufficiently negatively biased all electrons within a narrow sheath will be repelled and only an ion current is left. This so-called ion saturation current is independent of voltage [Wesson, 2004],

$$I_{\rm sat} = en_e\sqrt{T_e/m_i} \ . \tag{2.16}$$

$I_{\rm sat}$ is often assumed to be a proxy for density because temperature fluctuations are generally thought to be much smaller than density fluctuations. Fluctuation data from Langmuir probes generally has much higher time resolution than data from other more complicated plasma diagnostics, making it ideal for statistical analysis.

2.3.3 Scaling of absolute moments

We treat $I_{\rm sat}$ fluctuations, measured in the edge region of MAST and LHD, as steps of a random walk $s(t)$ on a temporal scale $\tau_{\rm min}$, the time between consecutive measurements; $\tau_{\rm min} = 4\mu$s for the LHD datasets and $\tau_{\rm min} = 2\mu$s for the MAST datasets that we examine here. Fluctuations on longer time scales are obtained by summing over a window of length τ [Dudson et al., 2005; Yu et al., 2003],

$$\delta I_{\rm sat}(t,\tau) = \sum_{t'=t}^{t+\tau-\tau_{\rm min}} (I_{\rm sat}(t') - < I_{\rm sat} >_t)/\sigma \ , \tag{2.17}$$

where $< I_{\rm sat} >_t$ and σ are the mean and standard deviation of the $I_{\rm sat}$ signal calculated over all times. The scaling properties of the absolute moments of these fluctuations,

$$S_m(\tau) \equiv \langle |\delta I_{\rm sat}(t,\tau)|^m \rangle \ , \tag{2.18}$$

are analysed. If scaling is present, $S_m \propto \tau^{\zeta(m)}$, and a plot of S_m versus τ on a log-log scale will yield a straight line for each m with gradient $\zeta(m)$. In general, owing

to intermittency, $\zeta(m)$ can be a nonlinear function of order m and the time series is multi-affine. If, however, $\zeta(m) = \alpha m$ where α is a constant, the time series is said to be self-affine or self-similar with a single scaling exponent α.

The scaling exponent α is also known as the Hurst exponent H. The Hurst exponent is a measure of long-time correlations and takes values between $0 \leq \alpha \leq 1$ [Carreras et al., 1998]. A value of $\alpha = 0.5$ implies that a signal has no correlations, i.e. each step in the random walk is independent of all others. A value of $0.5 < \alpha < 1$ implies 'persistency' while $0 < \alpha < 0.5$ implies 'anti-persistency,' i.e. if a random walk step is positive, the next step is more likely to be positive than negative when $0.5 < \alpha < 1$ and is more likely to be negative than positive when $0 < \alpha < 0.5$. A value of $\alpha = 0$ corresponds to a signal that does not change with time, while $\alpha = 1$ corresponds to a signal that changes deterministically with time.

2.3.4 Synthetic time series

The presence of a deterministic process such as a coherent mode or sine wave, embedded in an otherwise turbulent time series, is likely to distort the estimate of α. We now test this using synthetic time series because, as we shall see, our LHD datasets sometimes combine turbulent fluctuations with a few strong coherent modes.

Our first test signal is a pure sine wave 100 000 points long and with period $T = 100$ points. The first to fourth order absolute moments S_m are plotted on a log-log scale in figure 2.1(a). Scaling is observed for the region τ less than T; T is indicated on the graph by a vertical dashed line. A linear regression is applied for all S_m and the resulting $\zeta(m)$ is plotted versus m in figure 2.1(b); errors represent the errors of the regression. Figure 2.1(b) shows a linear fit $\zeta(m) = \alpha m$ with $\alpha = 0.99 \pm 0.01$, close to 1 as expected for a sine wave. For values of τ greater than T the absolute moments do not change with τ, in an averaged sense. Thus the scaling exponent $\alpha \approx 0$. This occurs because in (2.17) for $\tau > T$, the summation window is longer than the period so that the sinusoidal nature is effectively ignored and the signal appears not to change

with time. In between these two regions, around $\tau = T$, absolute moments dip. This is because the sum over all points over a sine wave's period is equal to zero. Absolute moments do not go exactly to zero because of the finite signal length.

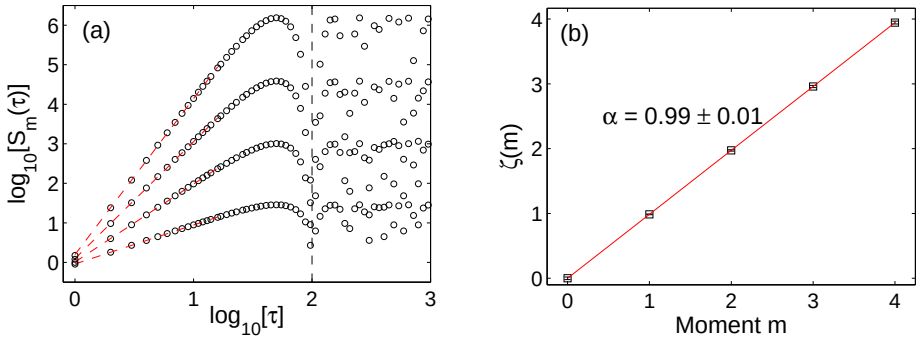

Figure 2.1: (a) Absolute moments of order $1 \leq m \leq 4$ and (b) derived scaling exponents $\zeta(m)$ for a sine wave 100 000 points long. The dashed line in (a) indicates the period of the sine wave, $T = 100$ points.

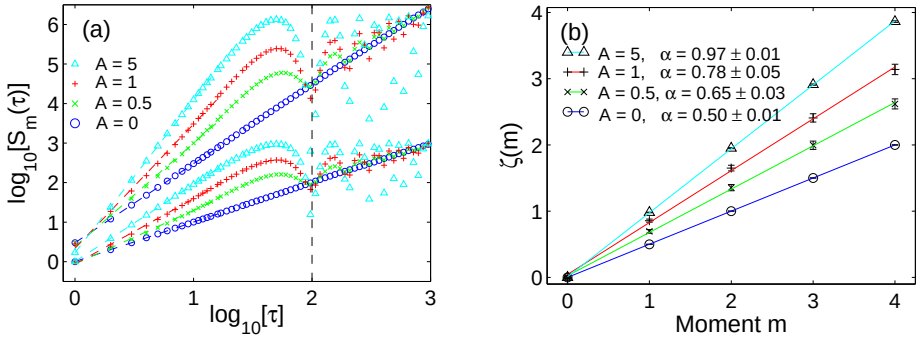

Figure 2.2: (a) Absolute moments of order $m = 2$ and $m = 4$ and (b) derived scaling exponents $\zeta(m)$ for random Gaussian noise added to a sine wave 100 000 points long. Moments $m = 1$ and $m = 3$ are omitted from (a) for clarity. The dashed line in (a) indicates the period of the sine wave, $T = 100$ points. The amplitude of the sine wave relative to to the standard deviation of the Gaussian noise, $A = a/\sigma$, is varied.

Next we consider the highly relevant case where a randomly fluctuating signal of interest is 'contaminated' by a sine wave, representing a coherent mode; for simplicity, we use Gaussian noise as the signal of interest. The total signal is of the form $s_i =$

$a \sin(2\pi t_i/T) + \gamma_i$, where a is a constant and γ_i is a random number taken from a Gaussian distribution with mean 0 and standard deviation σ. We vary the amplitude of the sine wave relative to the standard deviation of the Gaussian noise, $A = a/\sigma$. Figure 2.2(a) shows the absolute moments for signals of this form, 100 000 points long and with period $T = 100$. For clarity, only moments $m = 2$ and $m = 4$ are plotted. Linear regressions are applied and figure 2.2(b) shows the resulting estimates of α. For $A = 0$, i.e. pure Gaussian noise, the absolute moments scale as expected with $\alpha = 0.50$. As the amplitude of the sine wave is increased, the scaling behaviour tends to that of a pure sine wave with scaling exponent α close to 1 for τ less than T and a dip around $\tau = T$. We conclude that the presence of a coherent mode with period T is characterised by scaling in absolute moments for $\tau < T$ and a dip around $\tau = T$.

2.4 LHD scaling

2.4.1 LHD data

We now focus on I_{sat} data taken from LHD. Time series are obtained from three tips in a Langmuir probe array embedded in the divertor plate [Masuzaki et al., 2002] of LHD. The locations of the divertor plate and the Langmuir probe array in LHD are indicated in figure 2.3. The tips, labelled 16, 17 and 18, are separated by 6mm and sample data at 250kHz. The connection length L_c of the magnetic field lines connected to the tips is a few metres for tip 16, a few kilometres for tip 17 and a few tens of metres for tip 18 [Ohno et al., 2006b]. A long connection length means that the magnetic field line rotates around the ergodic layer near to the core plasma [Ohno et al., 2006b]. Connection lengths are calculated by modelling magnetic fields in a vacuum and may be different in the presence of a plasma. Datasets from LHD discharge numbers 44190 and 44191 are found to be statistically almost identical and therefore only 44190 is shown in this chapter. In both discharges the magnetic field strength is $B = 2.5$T and the central value of electron temperature is $T_{\mathrm{e}} = 2.5$keV. The line averaged density

is $\bar{n}_{\mathrm{e}} = 1.5 \times 10^{19}\mathrm{m}^{-3}$ in 44190 and $\bar{n}_{\mathrm{e}} = 1.4 \times 10^{19}\mathrm{m}^{-3}$ in 44191. The data was previously studied from a complementary perspective in [Ohno et al., 2006b] and [Ohno et al., 2006a]. A snapshot of the visible light from discharge 44190 is shown in figure 2.4. The visible light is predominantly D_α line emission due to the interaction of hot plasma with neutral gas in the edge region.

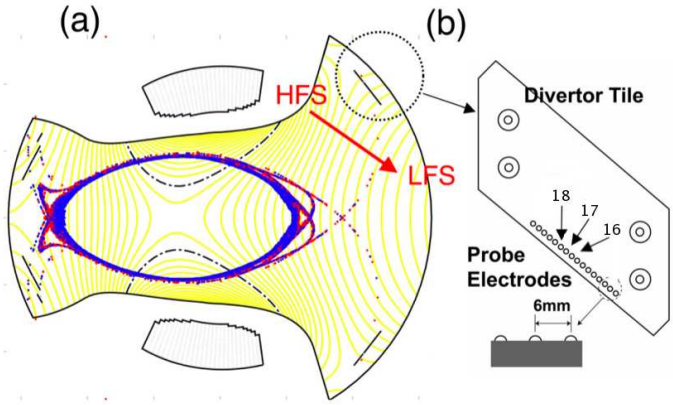

Figure 2.3: (a) Location of the Langmuir probe array within LHD [Ohno et al., 2006b]. (b) Location of probes within probe array [Ohno et al., 2006b].

Figure 2.4: Visible light image of LHD discharge 44190.

We prepare the data by removing linear trends, subtracting the mean and dividing by the standard deviation. Linear trends distort the absolute moment analysis as they are deterministic in nature. Figure 2.5 shows the resulting time series for the three tips in LHD plasma 44190. We see that the three I_{sat} time series are bursty and intermittent

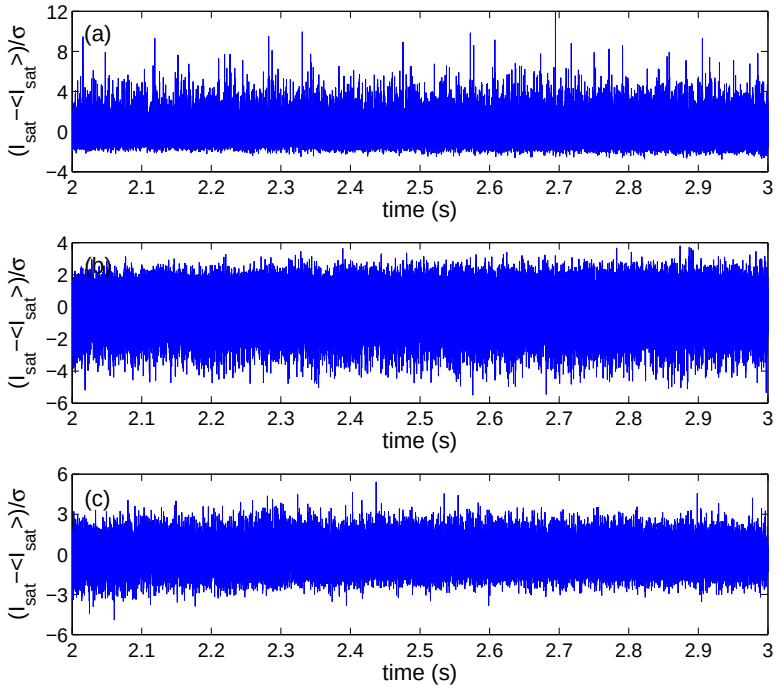

Figure 2.5: I_{sat} signals for LHD plasma 44190: (a) tip 16; (b) tip 17; (c) tip 18.

to varying degrees; significant differences between the tips, separated by 6mm, can be seen. Fluctuations measured by tip 16 are dominated by positive intermittent bursts with large amplitudes; tip 17 is characterised by negative intermittent bursts with smaller amplitudes; and the time series for tip 18 is almost symmetric. Similar behaviour can be observed with a different set of three probes by altering the position of the plasma in LHD [Ohno et al., 2006b].

2.4.2 Scaling properties

We now examine the statistical properties of the LHD I_{sat} signals. We use the power spectral density (PSD) estimated via the Thomson multitaper method [Thomson, 1982] which is then averaged over logarithmically spaced windows. Figure 2.6 shows the absolute moments and PSDs for all three tips in LHD plasma 44190. Scaling is clearly evident in S_m for all tips; linear fits are plotted. Tips 16 and 17 show two distinct

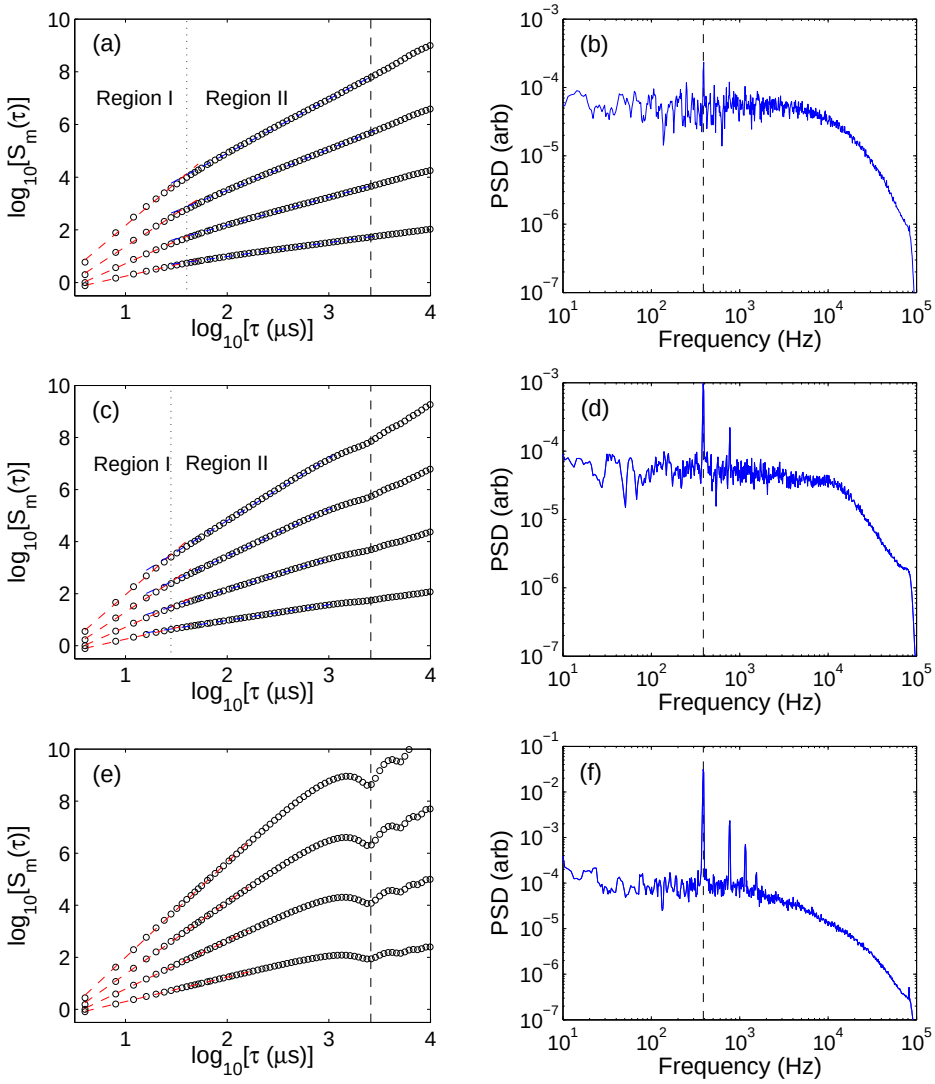

Figure 2.6: Absolute moments of order $1 \leq m \leq 4$ (left) and power spectral density (right) for LHD plasma 44190: (a) and (b) tip 16; (c) and (d) tip 17; (e) and (f) tip 18. The dashed line on each plot of absolute moments corresponds to the reciprocal of the frequency of the coherent mode marked on the power spectral density.

regions of scaling separated at about $\tau = 40\mu$s for tip 16 and $\tau = 30\mu$s for tip 17. Tip 18, however, shows only one region of scaling with scaling exponent α close to 1. In contrast with absolute moments, the PSDs do not exhibit a clear region of scaling, except for tip 17 which shows power-law scaling of the form $\sim f^{-\beta}$ with $\beta = 1.7$ in the region 10-100kHz, corresponding to 10-100μs. A low frequency coherent mode at $f_{cm} \simeq 390$Hz, together with higher harmonics, appears in all PSDs, and is marked by a dashed line in each PSD in figure 2.6. Its amplitude is smallest for tip 16 and largest for tip 18. The reciprocal of the frequency of this coherent mode, $1/f_{cm}$, is also marked on each absolute moment plot by a dashed line.

The scaling behaviour of tip 18 is very close to that of the second test case, figure 2.2(a): absolute moments scale with scaling exponent α close to 1 for τ less than $1/f_{cm}$ and a dip around $\tau = 1/f_{cm}$. It is clear the that signal from tip 18 is strongly affected by the presence of the coherent mode. Absolute moments for tip 17 are also affected but to a lesser degree; there is small flattening around $\tau = 1/f_{cm}$. There appears to be little or no effect on the absolute moments for tip 16; this might be expected as the amplitude of the coherent mode in the PSD is relatively low.

It is clear that the presence of a coherent mode in the signal affects its scaling properties. We have therefore filtered out the coherent modes and harmonics in each time series by applying Chebyshev type I bandstop filters to peaks in the PSD which rise above 2.5×10^{-4} of our arbitrary units. This corresponds to filtering out a single mode at frequency $f_{cm} \simeq 390$Hz for tip 16, 2 modes at f_{cm} and $2f_{cm}$ for tip 17 and 4 modes at f_{cm}, $2f_{cm}$, $3f_{cm}$ and $4f_{cm}$ for tip 18.

An alternative way of illustrating the effect of filtering on the datasets considered here is to compute the autocorrelation function (ACF), which is defined by equation 2.7. Note that the Fourier transform of the ACF is the PSD so oscillations in the ACF correspond to peaks in the PSD. Statistical properties of a signal strongly depend on the level of correlations and the ACF allows one to estimate the temporal scale, τ_A, beyond which correlation effects have no significant impact on the observed statistics.

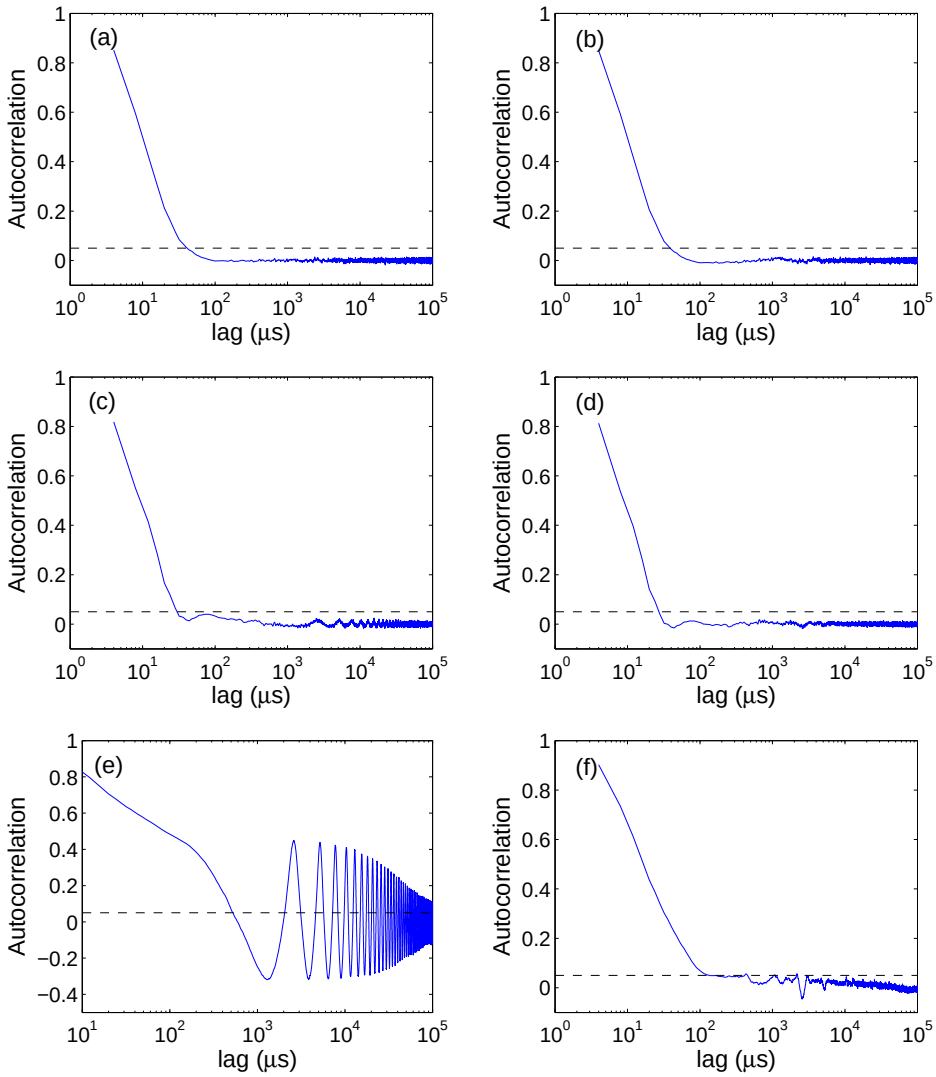

Figure 2.7: Autocorrelation function for LHD plasma 44190 before (left) and after (right) bandstop filtering to remove coherent modes: (a) and (b) tip 16, (c) and (d) tip 17, (e) and (f) tip 18. The horizontal dashed line at 0.05 is used to define τ_{A}.

	LHD 16	LHD 17	LHD 18	MAST
Decorrelation time, τ_A	40μs	30μs	130μs	60μs
S_m break, τ_m	40μs	30μs	45μs	30μs
Half-width of conditional average peak, τ_C	13μs	12μs	15μs	13μs
Skewness time scale, τ_S	220μs	110μs	10μs	500μs

Table 2.1: Measured time scales.

Practically, this is achieved by finding a first crossing of an arbitrary, but small, threshold which in our case we set to 0.05. Figure 2.7 shows the behaviour of the ACF before and after the filtering has been applied. The ACF for tip 18 is particularly affected; before filtering large oscillations appear, after filtering the ACF closely resembles that of the other two tips. Tip 17 is also affected; oscillations in the ACF are reduced for large values of τ. The decorrelation times τ_A obtained from the filtered data are presented in table 2.1. We see that τ_A is about 4 times larger for tip 18 than for tips 16 and 17 due to the slow fall-off of the ACF to zero.

The results of absolute moments analysis of the filtered data are shown in figure 2.8. We note that, in principle, the complete characterisation of a dataset with N samples requires N moments. However, in practice one should only examine as many moments as can be safely computed from the finite size datasets that are studied. We find that the slow convergence of the higher moments prohibits us from computing moments higher than order four. Figures 2.8 (a), (c) and (e) show the first to fourth order absolute moments for fluctuations measured by tips 16, 17 and 18 respectively. All three tips now show two distinct regions of scaling, separated at about 40μs for tip 16, 30μs for tip 17 and 45μs for tip 18. We label this break in absolute moments τ_m and include it in table 2.1.

In figures 2.8 (b), (d) and (f), $\zeta(m)$ versus m is plotted for all pins and in both scaling regions. In all cases, we apply a linear fit $\zeta(m) = \alpha m$ with $\zeta(0) = 0$, to extract a single scaling exponent α. This dual scaling regime has previously been

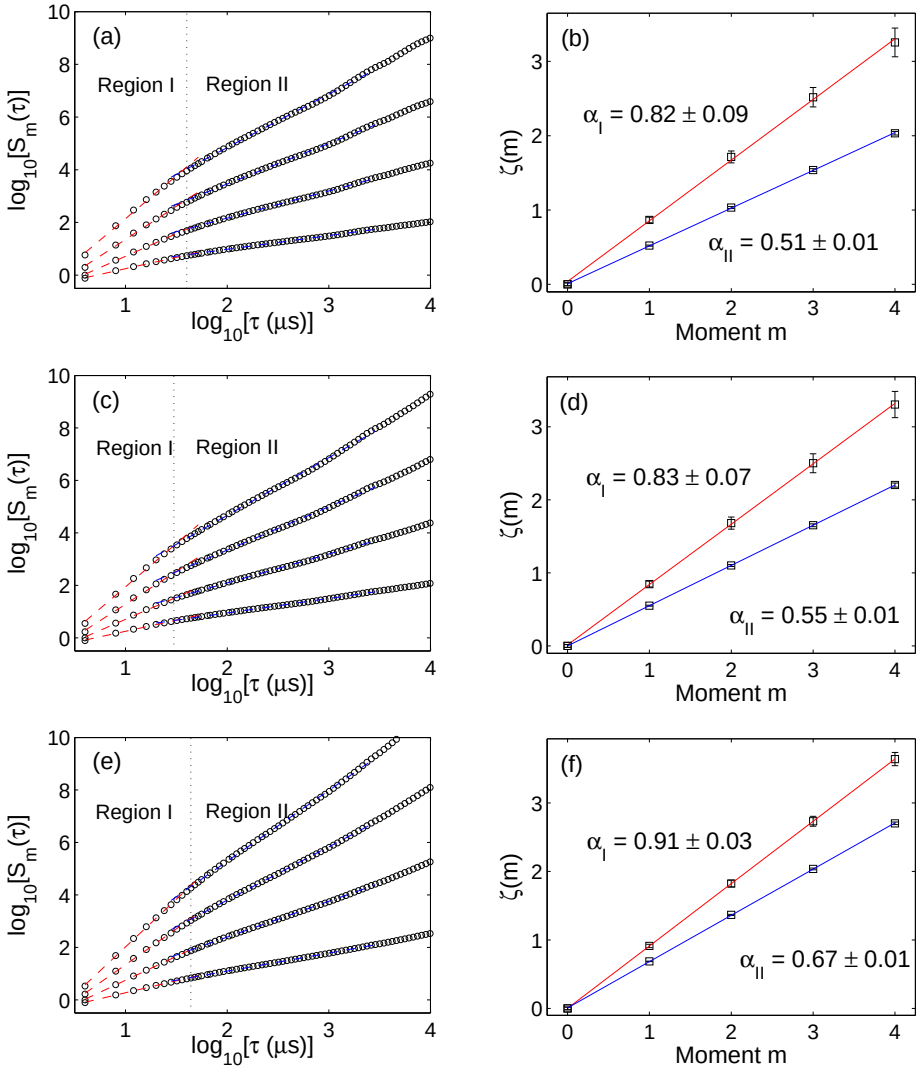

Figure 2.8: Absolute moments of order $1 \leq m \leq 4$ (left) and derived scaling exponents $\zeta(m)$ (right) for I_{sat} signal of LHD plasma 44190 with bandstop filters applied to remove coherent modes: (a) and (b) tip 16; (c) and (d) tip 17; (e) and (f) tip 18.

reported in MAST with the scaling break at 40-60μs [Hnat et al., 2008; Dudson et al., 2005]. It is believed that scaling exponents uniquely characterise time series and, in cases such as Kolmogorov turbulence or critical systems, may offer the connection to phenomenological description. It is therefore of interest to compare the values of the scaling exponent α that are obtained in these two regimes for different confinement systems. The average value for the short time scale scaling parameter α_I obtained from three similar MAST plasmas in [Hnat et al., 2008] is 0.94 ± 0.07, whereas the values of α_I in LHD for tips 16 and 17 fall below this. However, tip 18 has $\alpha_I = 0.91 \pm 0.03$; this value overlaps with that of the Hurst exponent for MAST L-mode plasma 6861, obtained for fluctuating time scales less than 30μs using three different algorithms in [Dudson et al., 2005]. In the longer time scale scaling region there are some notable similarities: MAST plasma 14218 has $\alpha_{II} = 0.59 \pm 0.04$, overlapping with $\alpha_{II} = 0.55 \pm 0.01$ for tip 17 of LHD plasma 44190; MAST plasmas 14219 and 14220 have $\alpha_{II} = 0.64 \pm 0.02$ and $\alpha_{II} = 0.65 \pm 0.02$, overlapping with $\alpha_{II} = 0.67 \pm 0.01$ for tip 18 of LHD plasma 44190. These quantitative matches suggest a degree of universality in the properties of edge turbulence on times scales $\gtrsim 40\mu$s for the different plasmas examined. These results, as well as a larger comparative study of Carreras et al. [Carreras et al., 1998], suggest that exponents characterising long temporal correlations, α_{II}, cluster in the region $0.5 - 0.7$.

2.5 MAST scaling

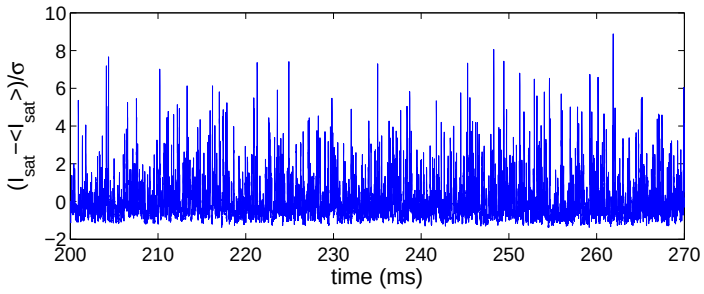

Figure 2.9: $I_{\rm sat}$ signal from MAST plasma 14222.

Here, we apply the absolute moment analysis to data taken from MAST L-mode plasma 14222 as a comparison to the LHD results. The data is taken from a reciprocating Langmuir probe located at the outboard midplane on MAST, and samples at a frequency of 500kHz. We prepare the data by removing linear trends, subtracting the mean and dividing by the standard deviation. Figure 2.9 shows the resulting data which is used in the analysis. The MAST data, like the LHD data, is bursty and intermittent and contains structures on many different time scales.

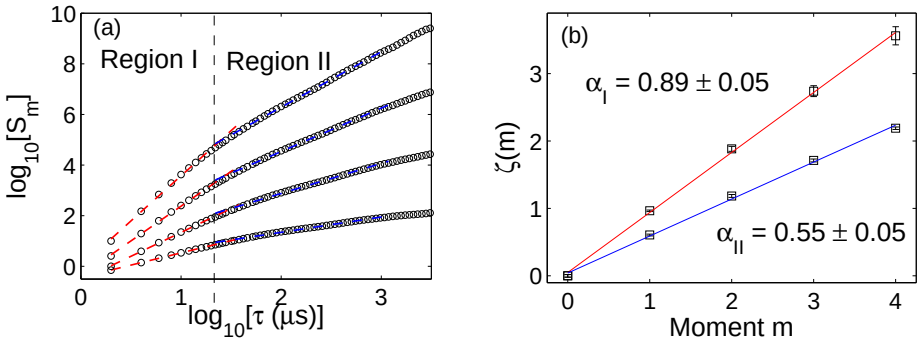

Figure 2.10: (a) 1st to 4th order absolute moments for MAST 14222. Two scaling regions are evident with a break at 30μs. (b) Estimation of α for the two scaling regions.

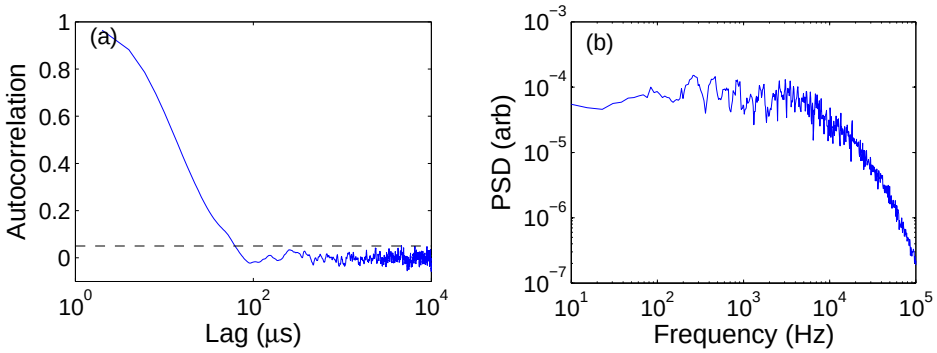

Figure 2.11: (a) Autocorrelation function and (b) PSD for MAST plasma 14222.

Figure 2.10(a) shows the absolute moments of order 1 to 4, calculated using the data in figure 2.9. In common with the LHD results in this chapter and the results in

[Hnat et al., 2008] and [Dudson et al., 2005], two distinct scaling regions can be seen. The break between the scaling regions is at about 30μs. Linear fits are applied and figure 2.10(b) shows the plot of $\zeta(m)$ versus m and the resulting estimate of α for the two scaling regions; the error bars represent the errors of the linear regression. We find for this MAST dataset, $\alpha_I = 0.89 \pm 0.05$ and $\alpha_{II} = 0.55 \pm 0.05$. For completeness, in figure 2.11 we also show the autocorrelation function and PSD for this dataset. The decorrelation time τ_A and the scaling break time τ_m are included in table 2.1.

2.6 Probability density function

2.6.1 LHD

The probability density function (PDF) is less affected by the finite data constraints encountered when calculating moments as moments are powers of the fluctuations. The PDF provides additional information on the behaviour of higher order moments. The PDF of a given dataset can be expressed as an infinite expansion in moments of all orders [Sornette, 2000]. It follows, that two distinct signals may share scaling properties of a single moment, for example the Hurst exponent or a power spectrum. It has been recognised that scaling in a dataset can emerge as a result of temporal correlations or heavy tails of the PDF [Mandelbrot, 2002]. A particular approach is to quantify the departure of the observed distributions from the Gaussian PDF for which all characteristics are known. We use the skewness S and kurtosis K; the Gaussian PDF has $S = 0$ and $K = 3$. Information on the dynamics of the PDFs can be obtained by the use of scaling in S and K on different temporal scales [Dudson et al., 2005; Hnat et al., 2003]. Let us consider the PDF of $\delta I_{\rm sat}(t, \tau)$ for two values of τ lying in different scaling regions determined from figure 2.8. Figure 2.12 shows the PDFs $P(\delta I_{\rm sat}, \tau)$ for $\tau = 4\mu$s and $\tau = 64\mu$s for all three tips. The PDF for $\tau = 4\mu$s is equivalent to the PDF of the original time series (since $\tau_{\rm min} = 4\mu$s) and is in scaling region I; $\tau = 64\mu$s is in scaling region II. We normalise each PDF to the standard deviation of $\delta I_{\rm sat}(t, \tau)$.

Filtered data is used in all cases. Gaussian PDFs with the same mean and standard deviation as the data are plotted for comparison (dashed lines).

On the short time scale, significant differences between the tips, separated by 6mm, can be seen. The PDF for tip 16 shows a large departure from Gaussian, with a large positive skewness $S = 1.0$ and kurtosis $K = 5.8$, indicating that the signal is dominated by large positive events. Tip 17's PDF is negatively skewed with $S = -0.4$ and $K = 3.6$, indicating that there are more negative events than the Gaussian prediction. The PDF for tip 18 is close to Gaussian with a small positive skew $S = 0.1$ and $K = 3.4$. On the longer time scale ($\tau = 64\mu$s), the shape of the PDF changes, particularly for tips 16 and 17: for tip 16 $S = 0.4$ and $K = 3.5$; for tip 17 $S = -0.1$ and $K = 3.0$; and for tip 18 $S = 0.1$ and $K = 3.3$. More generally, we find that the values of S and K vary with τ as shown in figure 2.13. For large τ, S and K do not go to 0 and 3, indicating that the PDFs deviate from Gaussian. This behaviour is in common with results from MAST [Hnat et al., 2008], where the PDFs on long time scales were close to the Gumbel distribution. We define a temporal scale, τ_S, as the time scale at which skewness S falls to within 0.1 of its Gaussian limit, i.e. $S = \pm 0.1$. The threshold is plotted on figures 2.13 (a), (c) and (e) as dotted lines. τ_S is a measure of the time scale on which the PDF changes. The results of this analysis are shown in table 2.1 and discussed in Section 2.8.

For I_{sat} time series which are far from Gaussian, approximating the discrete PDFs generated from data with a continuous functional form becomes an important but difficult problem. Successful fitting yields information on the underlying physics of the turbulence. Following a recent paper analysing the statistics of turbulent fluctuations in the MAST edge plasma [Hnat et al., 2008], we consider the applicability of Fréchet and Gumbel distributions which are derived from extreme value statistics [Sornette, 2000]. We find that this fitting is only appropriate for tip 16 in the short time scale region; see figure 2.12(a), showing Fréchet in red and Gumbel in green. The Fréchet distribution is

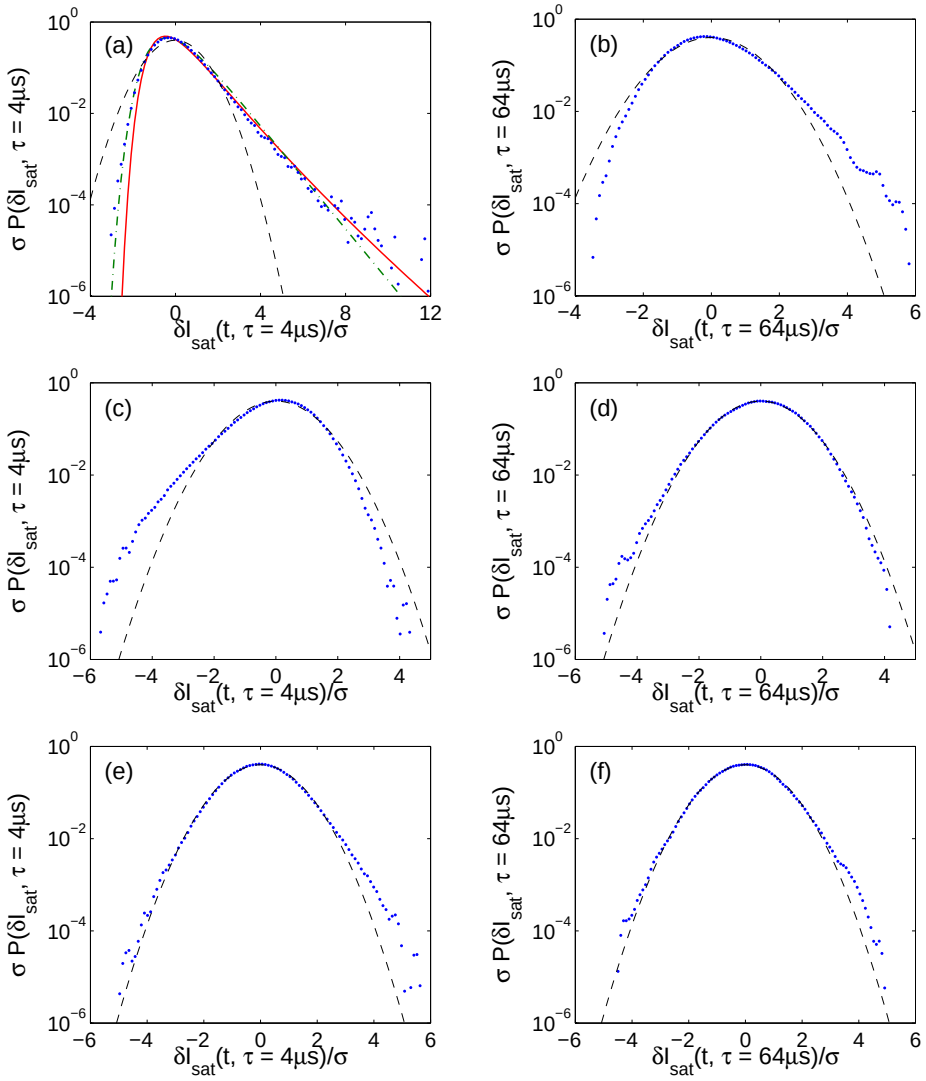

Figure 2.12: Probability density functions $P(\delta I_{\rm sat}, \tau)$ of the filtered data for $\tau = 4\mu$s (left) and $\tau = 64\mu$s (right) normalised to, σ, the standard deviation of $\delta I_{\rm sat}(t, \tau)$: (a) and (b) tip 16; (c) and (d) tip 17; (e) and (f) tip 18. Gaussian PDFs (dashed line) are plotted for comparison. In (a) we show Fréchet (red) and Gumbel (green) fits.

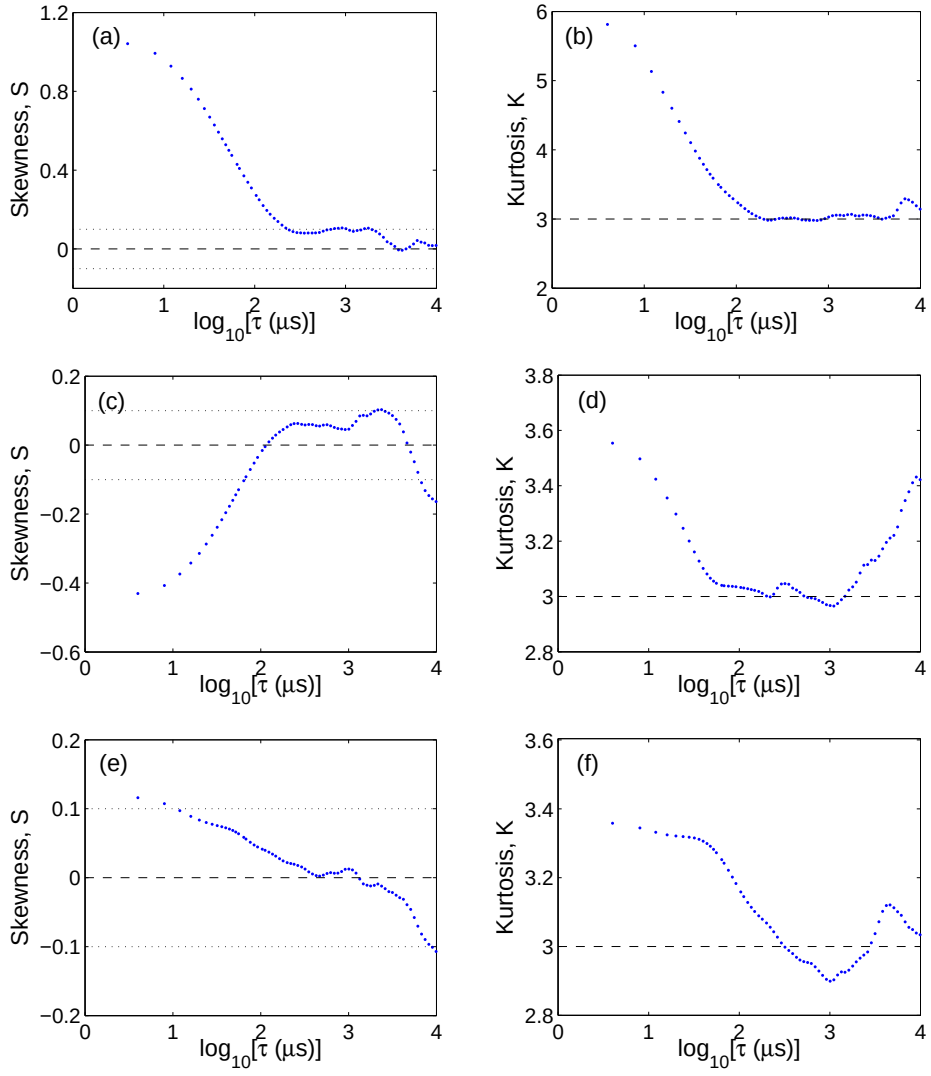

Figure 2.13: Measured skewness and kurtosis as a function of τ for all three tips in LHD plasma 44190, using filtered data for: (a) and (b) tip 16; (c) and (d) tip 17; (e) and (f) tip 18. Horizontal dashed lines mark Gaussian values for skewness ($S = 0$) and kurtosis ($K = 3$) respectively. Horizontal dotted lines mark the threshold $|S| = 0.1$ for the skewness time scale τ_S.

given by

$$P_F(x,k) = C_F \exp(-x^{-k})/(x^{1+k}) \ , \tag{2.19}$$

while the Gumbel distribution is defined as

$$P_G(x,a) = C_G \exp[-a(x+e^{-x})] \ , \tag{2.20}$$

where k and a are fitting parameters. We find the best fits to be $k = 1.025$ and $a = 1.3$ for tip 16. However neither distribution captures the full discrete PDF: the positive tail is better represented by Fréchet while negative values are closer to the Gumbel distribution.

2.6.2 MAST

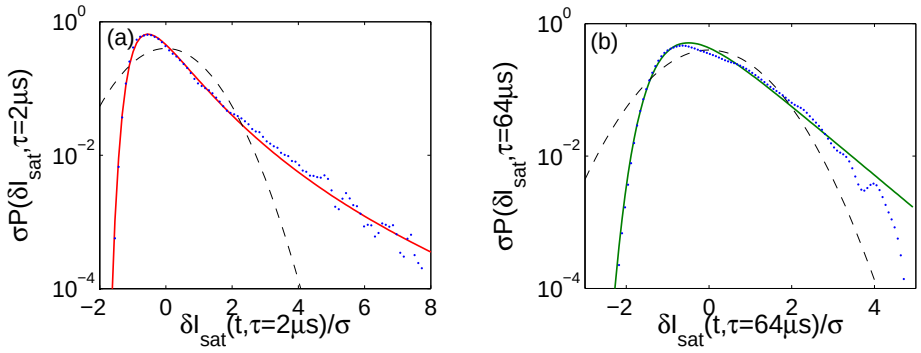

Figure 2.14: Probability density functions $P(\delta I_{\rm sat}, \tau)$ of the MAST data for (a) $\tau = 2\mu$s and (b) $\tau = 64\mu$s normalised to, σ, the standard deviation of $\delta I_{\rm sat}(t,\tau)$. Gaussian PDFs (dashed line) are plotted for comparison. In (a) we show Fréchet fit (red) and in (b) Gumbel fit (green).

The normalised PDFs $P(\delta I_{\rm sat}, \tau)$ for MAST with $\tau = 2\mu$s and $\tau = 64\mu$s are shown in figure 2.14. The PDF for $\tau = 2\mu$s is in scaling region I, while $\tau = 64\mu$s is in scaling region II. Gaussian PDFs with the same mean and standard deviation as the data are plotted for comparison (dashed lines). In common with the data from LHD tip 16, both PDFs are skewed towards positive values of $I_{\rm sat}$ and far from Gaussian. In the short time scale region ($\tau = 2\mu$s) we measure $S = 2.1$ and $K = 10.0$, while in the

longer time scale region ($\tau = 64\mu$s) $S = 0.9$ and $K = 3.6$. The variation of S and K with τ is shown in figure 2.15. We also consider Fréchet and Gumbel fits to the PDFs. We find that in the short time scale region, a Fréchet distribution with $k = 1.2$ is a satisfactory fit, while in the longer time scale region, a Gumbel distribution with $a = 1.5$ fits well. These results compare favourably with a more detailed study of many MAST datasets in [Hnat et al., 2008] which found that the δI_{sat} distribution on short time scales is well fitted by a Fréchet with index $k = 1.25$, while the Gumbel distribution with $a = 1.4$ gives a satisfactory description of the PDF on long time scales. The fitting of positively skewed Fréchet and Gumbel distributions indicates the increased likelihood of positive events as compared to Gaussian. In a large tokamak such as ITER, this may mean large bursts of plasma will reach the vessel wall and potentially cause damage.

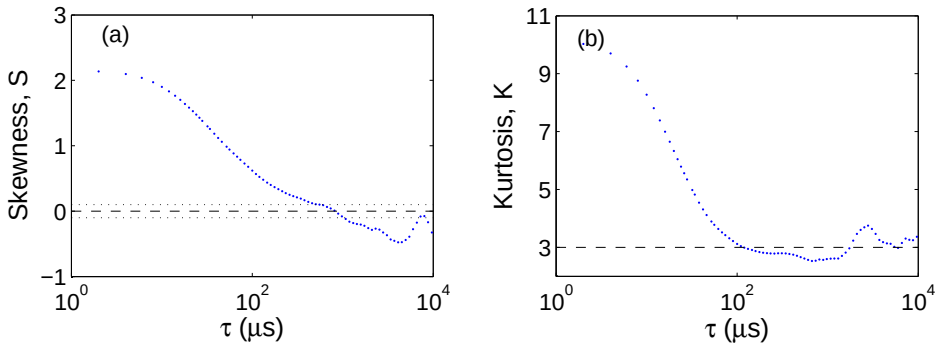

Figure 2.15: Measured skewness and kurtosis as a function of τ for MAST plasma 14222. Horizontal dashed lines mark Gaussian values for skewness ($S = 0$) and kurtosis ($K = 3$) respectively.

2.7 Average temporal shape of large bursts

We now apply conditional averaging techniques [Pecseli and Trulsen, 1989] to characterise the average temporal shape of the largest intermittent bursts. Conditional averaging involves identifying certain bursts in the time series and averaging over their temporal shapes. Here, we identify bursts as parts of the signal which cross a certain

threshold from below, remain above that threshold for a finite time, and finally cross the threshold from above. In the present case, we choose the threshold to be three standard deviations. We take 25 equally spaced data points on either side of the maximum of each burst and use these to define the burst's temporal shape. The conditional average is the mean temporal shape of all selected bursts. The thresholding is performed on the absolute value of the signal so that the selection is not biased towards positive or negative bursts. Only bursts with maxima separated by at least one decorrelation time τ_A are chosen, so as not to include the same coherent structure more than once.

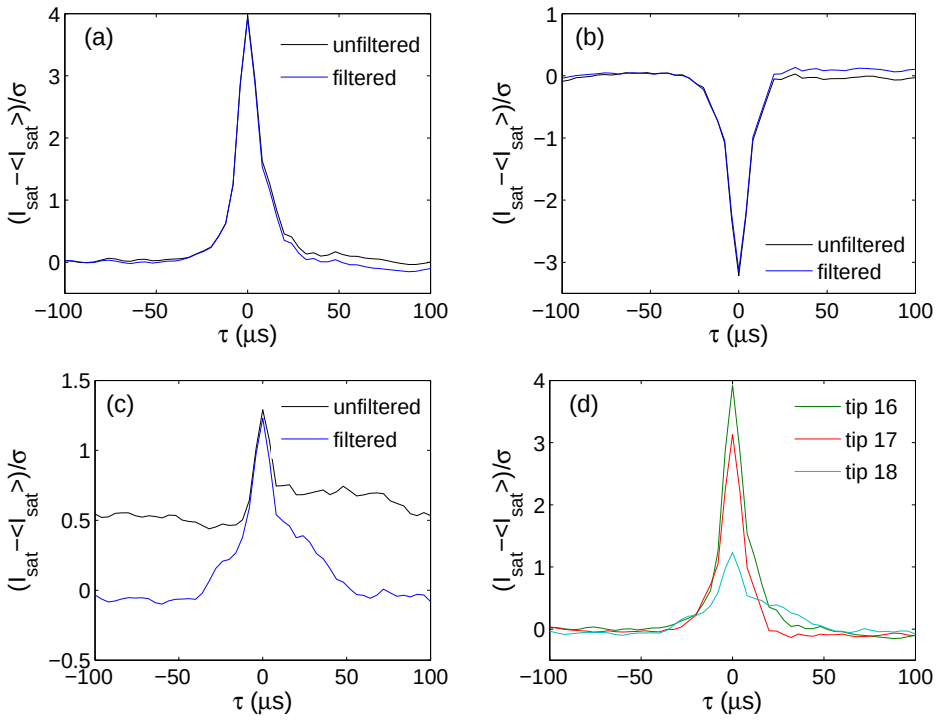

Figure 2.16: Average burst shapes calculated by conditional averaging for LHD plasma 44190 before and after filtering: (a) tip 16; (b) tip 17; (c) tip 18; (d) comparison.

The results of this process for both the filtered and unfiltered data are shown in figure 2.16 (a), (b) and (c). We show in 2.16(d) a comparison of all three average burst shapes using filtered data by reflecting the shape for tip 17 about the x-axis. We see that the effect of filtering on tips 16 and 17 is small, while the filtering of tip 18 uncovers

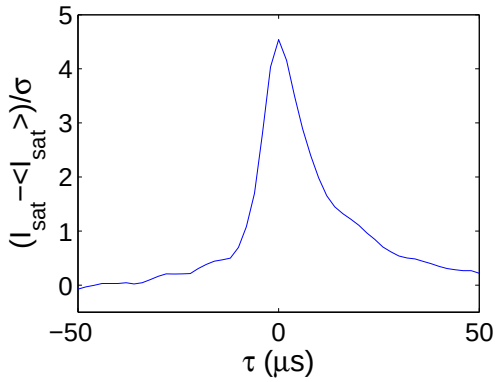

Figure 2.17: Average burst shape calculated by conditional averaging for MAST plasma 14222.

the burst shape. Tips 16 and 18 are dominated by positive bursts, or blobs, whereas tip 17 is dominated by negative bursts, or holes. This agrees with the analysis of time series and PDFs. The shape of the positive blobs, which rise quickly and fall slowly, in this stellarator plasma, is similar to that observed in other magnetic confinement devices; see for example figure 5 in [Antar et al., 2003] which shows the conditional average of I_{sat} signals taken from two different tokamaks, a spherical tokamak and a linear device. Negative holes have been observed in tokamaks [Boedo et al., 2003; Saha and Chowdhury, 2006] and linear devices [Carter, 2006]. The width of the conditional average peak at half its amplitude, τ_C, is 13μs for tip 16, 12μs for tip 17 and 15μs for tip 18.

The same conditional averaging analysis is performed on the MAST data and the results are shown in figure 2.17. We find a positive structure which rises quickly and falls off slowly with a half-width of 13μs. These results are presented for comparison in table 2.1.

2.8 Discussion

Edge and SOL transport is a complex phenomenon and only limited conclusions can be drawn from this pilot study. First, let us discuss qualitatively the observed statistical

properties in the context of other studies of edge and SOL transport in tokamaks and stellarators. The aim is to understand possible mechanisms that could lead to the very pronounced differences in the statistical properties of signals collected in LHD at spatial locations separated by only 6mm. The connection length, L_c, of the magnetic field lines connected to individual probe tips is a possible parameter responsible for the observed differences. Indeed, there is a monotonic dependence of the observed statistics on L_c: the skewness is positive for tip 16 (small L_c), tends to zero for tip 18 (medium L_c) and reverses to a negative value for tip 17 (long L_c). Similar statistical changes have previously been reported in tokamak and stellarator studies, where moving probes were used to measure the ion saturation current inside and outside of the last closed flux surface (LCFS) and in the vicinity of a velocity shear region [Boedo et al., 2003; Sanchez et al., 2000; Zoletnik et al., 1999]. It has been shown that the skewness of $I_{\rm sat}$ is positive in the SOL region and negative inside the LCFS. A value of skewness close to zero is often associated with the presence of velocity shear in the region where the signal originated from. Such shear destroys large coherent structures generated by the inverse energy cascade of 2D edge turbulence, hence one would expect the observed signal to be nearly Gaussian, as it is indeed in the case of tip 18 here. Thus one could explain the observed statistical differences in the analysed datasets by assuming that the short magnetic field line connected to tip 16 explores only an edge region of plasma, the magnetic field line of tip 18 penetrates a region of plasma where velocity shear is large and the field line of tip 17 explores a region of plasma closer to the core. We stress, however, that the rapid dissipation of structures should also lead to decorrelation in the signal. This is contradicted by our analysis of the autocorrelation function which gives largest decorrelation times for tip 18.

The above interpretation is not unique and other parameters may play an equally important role in the observed statistics. For example, the influence of the complex edge magnetic field topology and the presence of low order rational surfaces on edge and SOL transport is another possibility in explaining the observed features. We note that, unlike

the tokamak where the LCFS is well defined, a clear separatrix between closed and opened magnetic field lines does not exist in stellarators. Rather, the edge magnetic field is dominated by magnetic islands and the field lines may ergodically fill a finite volume. It has been observed that the direction of particle flux changes from outwards to inwards near rational surfaces in the TJ-II stellarator [Pedrosa et al., 2001]. This is manifested in the reversal of skewness in time series of probe measured flux, similar to the change in the sign of $I_{\rm sat}$ skewness recorded by tips 16 and 17. Similarly, numerical simulations of tokamak plasmas in the presence of ergodic magnetic field perturbations show the reversal of the local radial $E \times B$ flux close to resonances and the suppression of blob amplitudes [Reiser, 2007].

Turning to a quantitative discussion, we now examine the time scales measured for LHD. Table 1 gives a comparison of the decorrelation time, τ_A, the break in absolute moments τ_m, the half-width of the conditional average peak, τ_C and the skewness time scale τ_S. The first three measurements, τ_A, τ_m and τ_C, are largest for tip 18, smallest for tip 17 and in between for tip 16. This suggests that they are in some way related to each other. The width of the conditional average peak, τ_C, gives a characteristic time scale of blobs in the time series. It is reasonable to say that the decorrelation time and break in absolute moments are also due to blobs and that the relatively high value of the scaling exponent α_I in the first region is due to the coherent nature of these blob structures. The value of the decorrelation time, τ_A, for tip 18 is around four times larger than those for tips 16 and 17. We note that τ_A is highly sensitive to any periodic signal which may remain in the filtered time series and may also be strongly affected by quasi-periodic features resulting from plasma rotation [Carreras et al., 1998]. In the case of stellarators, where the edge magnetic field is ergodised, the spatio-temporal correlation of the local magnetic field may limit the observed decorrelation times, in that the ergodic magnetic field will not allow the field-aligned blobs to be fully developed.

While the presence of plasma blobs is consistent with the statistical features on small temporal scales, it is also important to examine larger temporal scales. This

could provide more information on the evolution and interaction of plasma blobs as well as the background fluctuations that they are embedded in. The scaling exponents α_{II} indicate that, in terms of long temporal correlations, tip 18 is the most interesting, being significantly different from the Gaussian case. We can further study these long temporal scales by examining the asymmetry of these signals, as given by skewness. Skewness estimates nonlinear interactions in the time series and, in the context of turbulent studies, is related to the rate of cascade for the quantity of interest. In that respect, τ_S can be thought of as a maximum scale at which nonlinear interactions are still significant. Thus τ_S is related to the distribution of the observed fluctuations, while both τ_A and τ_m are more sensitive to linear temporal correlations within the time series. We find that the nonlinear interactions of fluctuations for tip 16 are strong for nearly all of the temporal scales examined, they are less relevant for tip 17 and are very weak for tip 18.

2.9 Conclusions

We have analysed measurements of ion saturation current, $I_{\rm sat}$, made by three tips in a Langmuir probe array in the edge plasma of the LHD heliotron. Statistical methods such as absolute and signed moment analysis, PDF dynamics and conditional averaging have been used to quantify differences in the properties of the turbulence measured at each tip. The same analysis has been applied to a dataset taken from the Mega-Amp Spherical Tokamak for comparison purposes.

A monotonic change in the skewness of the analysed LHD signals with the connection length of the magnetic field lines attached to each tip is observed. We have discussed this statistical feature with reference to similar results from other experiments.

Absolute moment analysis is shown to be strongly affected by the presence of coherent modes in some of the datasets. Following filtering, however, absolute moment analysis reveals dual scaling regimes for all tips with the transition between different scaling at $30 - 45\mu$s. This transition could be due to the dominance of coherent blob structures in the short time scale region. More detailed studies are required in order to

understand the blob generation mechanisms and energetics.

Scaling exponents obtained for small and large temporal scales suggest clustering around similar values. For small temporal scales, we find strong correlations and scaling exponents in the range $0.8 - 0.9$. On long temporal scales, scaling exponents fall within the superdiffusive range $0.55 - 0.7$. These values are in good agreement with studies of other devices where long range correlations were found to be characterised by scaling exponents between $0.52 - 0.72$ [Carreras et al., 1998; Dudson et al., 2005; Hnat et al., 2008]. This suggests a degree of universality in the properties of edge turbulence across different confinement systems.

Chapter 3

The Hasegawa-Wakatani equations and the HAWK code

3.1 Introduction

Due to the extreme conditions encountered in fusion plasmas, their diagnosis is extremely challenging and experimental data on the temporal and spatial scales of interest is not always available. This problem can be avoided with the use of analytical and numerical modelling, and these tools also allow the development of further physical insight. Generally speaking, there are two approaches to modelling: 'top down' and 'bottom up'. In the top down approach, the physics is modelled in as much detail as is numerically possible in order to produce the most accurate results possible. As well as being computationally expensive, in this approach it may not always be clear which physical effects are responsible for the observed results. In the bottom up approach, a starting point is chosen where most of the physics is fairly well understood and extra complications are added one at a time. In this approach, physical effects can be studied in isolation. In this thesis, we follow the bottom up approach and choose the Hasegawa-Wakatani model [Hasegawa and Wakatani, 1983] as our starting point. The Hasegawa-Wakatani (HW) model is a paradigmatic description of drift wave turbulence in the edge

region of a tokamak plasma that has a non-uniform background density and uniform equilibrium magnetic field. A new numerical code, HAWK (HAsegawa-WaKatani), has been developed by the author as part of this thesis in order to solve the HW equations numerically.

In the next section the HW equations are derived from the Braginskii two fluid equations, which were introduced in Chapter 1. The numerical methods employed in the HAWK code to solve the HW equations are discussed in Section 3.3. The HAWK code is tested in Section 3.4 and a typical run of the code is demonstrated in Section 3.5. Modifications to the HW equations to include zonal flows and non-uniform magnetic field strength are discussed in Sections 3.6 and 3.7.

3.2 Derivation of Hasegawa Wakatani equations

The Hasegawa Wakatani equations can be derived from the Braginskii fluid equations [Braginskii, 1965] for a plasma with one electron species and one ion species. The physical setting is the edge region of a plasma magnetically confined by a uniform magnetic field $\mathbf{B}$ in the presence of a background density gradient ∇n_0, see figure 3.1. The equations provide a simple model of the drift wave instability and include nonlinear terms which lead to saturation and turbulence.

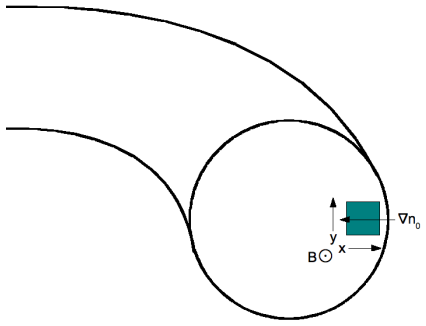

Figure 3.1: Physical setting of the Hasegawa-Wakatani equations. The shaded square represents the computational domain.

In order to dramatically simplify the equations, the ions are assumed to be

cold $T_i = 0$ and the plasma is assumed to be isothermal $T_e = \text{const} = T$. This first assumption is highly questionable in the edge region of tokamaks. However, retaining ion temperature leads to much more complicated equations (see [Scott, 2000], for example, for the gyrofluid equations) and it is thus neglected in many reduced fluid models. Experimental evidence suggests that fluctuations in the edge region of many magnetically confined plasmas are close to electrostatic and thus it is assumed, for the HW model, that electric fields can be expressed in terms of an electrostatic potential ϕ, $E = -\nabla\phi$. Since the electron mass is much smaller than the ion mass, electron inertia is neglected. Furthermore, all anisotropic pressure tensor terms (viscosity) are ignored and quasineutrality is assumed $n_e = n_i = n$.

Perpendicular ion momentum

Applying the above assumptions and resolving in the direction perpendicular to the magnetic field, the ion equation of motion becomes

$$mn\left(\frac{\partial}{\partial t} + \mathbf{v}\cdot\nabla_\perp\right)\mathbf{v} = ne(-\nabla_\perp\phi + \mathbf{v}\times\mathbf{B}) \ . \tag{3.1}$$

The lowest order ion perpendicular velocity is found by setting the left hand side to zero and taking the cross product with $\mathbf{B}$, giving the $E \times B$ drift velocity

$$\mathbf{v_E} = \frac{\mathbf{b}\times\nabla_\perp\phi}{B} \ , \tag{3.2}$$

where $\mathbf{b}$ is a unit vector pointing in the direction of $\mathbf{B}$. The next order correction is found by substituting v_E back into the momentum equation and taking the cross product with $\mathbf{B}$, giving the polarisation drift velocity

$$\mathbf{v}_p = \frac{m_i}{e}\frac{\mathbf{b}\times\left(\frac{\partial}{\partial t} + \mathbf{v_E}\cdot\nabla_\perp\right)\mathbf{v_E}}{B} \ . \tag{3.3}$$

The ion perpendicular equation of motion is thus reduced to a velocity, $\mathbf{v}_{i\perp} = \mathbf{v_E} + \mathbf{v}_p$.

Perpendicular electron momentum

In a similar way, the electron equation of motion perpendicular to the magnetic field is replaced with a velocity. With the assumptions above, we have for the electron

perpendicular equation of motion

$$0 = -ne(-\nabla_\perp \phi + \mathbf{v} \times \mathbf{B}) - T\nabla_\perp n \ . \tag{3.4}$$

Taking the cross product with $\mathbf{B}$ gives the electron perpendicular velocity

$$\mathbf{v}_{e\perp} = \frac{\mathbf{b} \times \nabla_\perp \phi}{B} - \frac{\mathbf{b} \times T\nabla_\perp n}{neB} = \mathbf{v}_\mathbf{E} + \mathbf{v}_{de} \ , \tag{3.5}$$

where $\mathbf{v}_\mathbf{E}$ is the same $E \times B$ velocity that was seen for ions and $\mathbf{v}_{de}$ is the electron diamagnetic drift velocity. We note that the polarization drift is neglected for electrons because of their small mass and the diamagnetic drift is neglected for ions because of the assumption that $T_i = 0$.

Parallel momentum

We now turn to the equations of motion parallel to the magnetic field. Due to the electron/ion mass ratio, electrons are much more mobile than ions in the parallel direction and accordingly ions are assumed to be immobile, $v_{i\parallel} = 0$. Thus the parallel dynamics are governed by the electrons alone. The parallel electron equation of motion is written as

$$0 = ne\nabla_\parallel \phi - T\nabla_\parallel n - \eta e^2 n^2 \mathbf{v}_{e\parallel} \ , \tag{3.6}$$

where the last term models collisions between the electrons and the immobile ions, and η is a resistivity. Note that if we assumed zero resistivity, the equation would lead to the so-called adiabatic electron response that was discussed in Section 1.8.3, equation 1.36, and there would therefore be no drift wave instability in the model. This assumption leads to the Hasegawa-Mima equation [Hasegawa and Mima, 1978]. Retaining the collisions term allows deviations from adiabaticity which produce the drift wave instability. Equation 3.6 can be re-written as a parallel current density,

$$\mathbf{J}_\parallel = \frac{T}{e\eta}\left[\frac{\nabla_\parallel n}{n} - \frac{e\nabla_\parallel \phi}{T}\right] \ . \tag{3.7}$$

Electron continuity

The Hasegawa-Wakatani equations are built by plugging the above results into the Braginskii continuity equations. First we write the electron continuity equation as

$$\frac{\partial n}{\partial t} + \mathbf{v}_{e\perp} \cdot \nabla_\perp n + n\nabla_\perp \cdot \mathbf{v}_{e\perp} - \frac{1}{e}\nabla_\parallel \cdot \mathbf{J}_\parallel = 0 \ , \tag{3.8}$$

and then substitute in the electron velocity from above $\mathbf{v}_{e\perp} = \mathbf{v}_\mathbf{E} + \mathbf{v}_{de}$. Some terms vanish, $\nabla_\perp \cdot \mathbf{v}_\mathbf{E} = 0$, $\nabla_\perp \cdot \mathbf{v}_{de} = 0$, and $\mathbf{v}_{de} \cdot \nabla_\perp n = 0$, leaving

$$\left(\frac{\partial}{\partial t} + \mathbf{v}_\mathbf{E} \cdot \nabla_\perp\right) n - \frac{1}{e}\nabla_\parallel \cdot \mathbf{J}_\parallel = 0 \ . \tag{3.9}$$

Ion continuity

Similarly, we write the ion continuity equation as

$$\frac{\partial n}{\partial t} + \mathbf{v}_{i\perp} \cdot \nabla_\perp n + n\nabla_\perp \cdot \mathbf{v}_{i\perp} = 0 \ , \tag{3.10}$$

and substitute in $\mathbf{v}_{i\perp} = \mathbf{v}_\mathbf{E} + \mathbf{v}_p$. Again, there are terms which vanish and the nonlinear term $v_p \cdot \nabla_\perp n$ is neglected leaving

$$\left(\frac{\partial}{\partial t} + \mathbf{v}_\mathbf{E} \cdot \nabla_\perp\right) n + n\nabla_\perp \cdot \mathbf{v}_p = 0 \ . \tag{3.11}$$

Invoking quasineutrality, the electron and ion continuity equations (3.9 and 3.11) are equated to give

$$n\nabla_\perp \cdot \mathbf{v}_p = -\frac{1}{e}\nabla_\parallel \cdot \mathbf{J}_\parallel \ . \tag{3.12}$$

Next, the term on the left hand side is written as

$$\nabla_\perp \cdot \mathbf{v}_p = -\frac{m_i}{e}\frac{1}{B^2}\left(\frac{\partial}{\partial t} + \mathbf{v}_\mathbf{E} \cdot \nabla_\perp\right)\nabla^2\phi \ , \tag{3.13}$$

thus we have

$$\left(\frac{\partial}{\partial t} + \mathbf{v}_\mathbf{E} \cdot \nabla_\perp\right)\nabla^2\phi = \frac{B^2}{nm_i}\nabla_\parallel \cdot \mathbf{J}_\parallel \ . \tag{3.14}$$

The quantity $\nabla^2\phi \equiv \omega$ is known as vorticity since it is equal to the curl of the $E \times B$ velocity.

Reduction

Equations 3.7, 3.9 and 3.14 form the three-dimensional Hasegawa Wakatani equations for density n and electrostatic potential ϕ. In this section, these equations are reduced further in order to make them easier to solve numerically. Firstly, the variables are split into background and fluctuating components $n = n_0 + \tilde{n}$, where time and spatial scale separation ensures $n_0 \gg \tilde{n}$ and $\partial n_0/\partial t = 0$ and $\nabla_\parallel n_0 = 0$. The background potential is assumed to be zero, thus $\phi = \tilde{\phi}$. Now the equation for parallel current density (3.7) becomes

$$J_\parallel = \frac{T}{e\eta}\left[\frac{\nabla_\parallel \tilde{n}}{n_0} - \frac{e\nabla_\parallel \tilde{\phi}}{T}\right] \ . \tag{3.15}$$

Secondly, the model is made two-dimensional by assuming a single parallel wavenumber k so that $\nabla_\parallel^2 \to -k^2$ and the divergence of $J_\parallel$ becomes

$$\nabla_\parallel \cdot J_\parallel = \frac{Tk^2}{e\eta}\left[\frac{e\tilde{\phi}}{T} - \frac{\tilde{n}}{n_0}\right] \ . \tag{3.16}$$

Thirdly, slab geometry is used with the magnetic field pointing in the z-direction $\mathbf{b} = \hat{\mathbf{z}}$ and a background density gradient pointing in the negative x-direction of the form $\nabla n_0 = -\hat{\mathbf{x}} n_0/L_n$, where L_n is the lengthscale of the gradient. Thus the x and y directions may be identified with the radial and poloidal directions respectively in a tokamak. In this geometry, nonlinear terms can be written using the Poisson bracket notation $\mathbf{v_E} \cdot \nabla_\perp \to \frac{1}{B}\left[\tilde{\phi},\ \right]$, where

$$[A, B] = \frac{\partial A}{\partial x}\frac{\partial B}{\partial y} - \frac{\partial A}{\partial y}\frac{\partial B}{\partial x} \ . \tag{3.17}$$

Normalisation

The final step in order to make the equations easier to solve numerically is to normalise them. We use the following mappings

$$\frac{e\tilde{\phi}}{T} \to \phi \ , \ \frac{\tilde{n}}{n_0} \to n \ , \ \omega_{ci} t \to t \ , \ \frac{x}{\rho_s} \to x \ , \tag{3.18}$$

where ω_{ci} is the ion gyrofrequency and $\rho_s = \sqrt{m_i T}/eB$ is the hybrid Larmor radius. The Hasegawa-Wakatani equations can now be written as

$$\frac{\partial n}{\partial t} = -\kappa \frac{\partial \phi}{\partial y} + \alpha(\phi - n) + [n, \phi] \ , \tag{3.19}$$

$$\frac{\partial}{\partial t}(\nabla^2 \phi) = \alpha(\phi - n) + \left[\nabla^2 \phi, \phi\right] \ , \tag{3.20}$$

where the two parameters of the model are

$$\alpha = \frac{Tk^2}{n_0 e^2 \eta \omega_{ci}} \text{ and } \kappa = -\frac{\partial \ln n_0}{\partial x} \ . \tag{3.21}$$

The parameter α contains the parallel wavenumber k and resistivity η. It controls the adiabaticity of the electrons and the strength of the resistive coupling between n and ϕ through the parallel current. In the limit $\alpha \gg 1$ the coupling is adiabatic ($n = \phi$ in our normalised units) and the HW equations reduce to the HM equation. The parameter κ characterises the background density gradient which drives the system.

In the HW model, the potential vorticity

$$\Pi = (\nabla^2 \phi - n + \kappa x) \ , \tag{3.22}$$

is a Lagrangian conserved quantity, $d\Pi/dt = 0$ where $d/dt = \partial/\partial t + [\phi, \ ]$ is the convective derivative associated with $E \times B$ drift.

3.3 Numerical methods

In this section, the numerical methods used in the HAWK code to solve the HW equations are described.

3.3.1 Dissipation

When numerically solving nonlinear fluid equations such as the Hasegawa-Wakatani equations, dissipation terms must be added to the equations by hand in order to ensure numerical stability. Dissipation terms act to remove energy from the small spatial

scales of the system which are beyond the limit of the numerical resolution and mimic viscocity. We add dissipation operators to each equation $\partial/\partial t \rightarrow \partial/\partial t - \mathcal{D}$. The form of the operator is either Newtonian viscocity $\mathcal{D} = D\nabla^2$ or hyperviscocity $\mathcal{D} = -D\nabla^4$. Hyperviscocity tends to preserve more of the turbulent inertial range than Newtonian, but requires an additional calculation in every time step.

3.3.2 Spatial discretisation

For simplicity, we perform calculations on a square and periodic grid which is discretised using the well-known finite difference method. The nonlinear Poisson bracket terms are discretised according to the method derived by Arakawa [Arakawa, 1966],

$$[\phi, f] = \frac{1}{3}(J^{++} + J^{+\times} + J^{\times+}) \ , \tag{3.23}$$

where

$$J^{++} = \frac{1}{4\Delta^2}\left[(\phi_{+0} - \phi_{-0})(f_{0+} - f_{0-}) - (\phi_{0+} - \phi_{0-})(f_{+0} - f_{-0})\right] \ , \tag{3.24}$$

$$J^{+\times} = \frac{1}{4\Delta^2}\left[\phi_{+0}(f_{++} - f_{+-}) - \phi_{-0}(f_{-+} - f_{--}) - \phi_{0+}(f_{++} - f_{-+}) + \phi_{0-}(f_{+-} - f_{--})\right] \ , \tag{3.25}$$

$$J^{\times+} = \frac{1}{4\Delta^2}\left[\phi_{++}(f_{0+} - f_{+0}) - \phi_{--}(f_{-0} - f_{0-}) - \phi_{-+}(f_{0+} - f_{-0}) + \phi_{+-}(f_{+0} - f_{0-})\right] \ . \tag{3.26}$$

Here, Δ is the grid spacing, the first and second subscripts refer to the x and y directions respectively and the '$-$' subscript denotes the previous grid node, the '0' subscript denotes the current grid node and the '$+$' subscript denotes the next grid node. This method is known to be well suited to solving the HW equations and conserves energy and enstrophy [Naulin and Nielsen, 2003].

3.3.3 Temporal discretisation

In order to evolve the equations in time, the equations are integrated using the Karniadakis 3rd order multi-step method [Karniadakis et al., 1991]. In this method $\partial x/\partial t =$

$f(x,t)$ is expressed as a linear combination of previous steps,

$$\frac{11}{6}x_n - 3x_{n-1} + \frac{3}{2}x_{n-2} - \frac{1}{3}x_{n-3} = 3f_{n-1} - 3f_{n-2} + f_{n-3} \ , \tag{3.27}$$

where the n subscript refers to the current time step, the $n-1$ subscript refers to the previous time step and so on. This method requires only one calculation per time step; however, since three previous time steps must be remembered, the memory requirements are relatively large. This Arakawa-Karniadakis combination of numerical methods was introduced in [Naulin, 2003], thoroughly tested in [Naulin and Nielsen, 2003] and described in detail in [Scott, 2008].

3.3.4 Poisson's equation

In the Hasegawa-Wakatani equations, the density n and vorticity $\omega = \nabla^2\phi$ are evolved, and not the potential ϕ. Therefore, at every time step the potential must be calculated from the vorticity, i.e. a solution to Poisson's equation must be found. When the boundary conditions are periodic in both dimensions, a 2D Fourier transform can be employed to compute ϕ from ω. This involves calculating the Fourier transform of the vorticity, ω_k, by using a fast-Fouier transform (FFT) algorithm; in the HAWK code the FFTW3 library is used [FFTW, 2009]. The potential can then be solved for in Fourier space using [Press et al., 1993]

$$\phi_k = \frac{\Delta^2\omega_k}{2\cos\left(\frac{2\pi m}{M}\right) + 2\cos\left(\frac{2\pi n}{N}\right) - 4} \ , \tag{3.28}$$

where m and n are the Fourier mode numbers and M and N give the size of the grid. The solution ϕ is obtained by applying an inverse fast-Fourier transform (IFFT) to ϕ_k. When the boundary conditions are periodic in only one dimension, it is possible to apply 1D FFT in that direction. The solution ϕ can then be found by inverting the resulting tri-diagonal matrix and applying a 1D IFFT [Press et al., 1993].

3.4 Testing the HAWK code

A new numerical code called HAWK has been written in C by the author. HAWK employs the above numerical techniques to solve the HW equations. In order to test the accuracy of the code, two tests have been employed. Firstly, the linear dispersion relation has been derived analytically and compared to the simulation results. Secondly, conservation laws for energy and enstrophy like quantities have been derived and used to check conservation by the code. The first test is a good test of the linear properties of the code while the second is a good test of the nonlinear properties.

3.4.1 Linear dispersion relation

We calculate the linear dispersion relation for plane waves of the form

$$n, \phi \sim \exp(ik_x x + ik_y y - i\omega t) \ , \tag{3.29}$$

by neglecting nonlinear terms and applying a Fourier transform. Using a Newtonian dissipation operator, the equations become

$$-i\omega n_k = -\kappa i k_y \phi_k + \alpha(\phi_k - n_k) - Dk^2 n_k \tag{3.30}$$

and

$$i\omega k^2 \phi_k = \alpha(\phi_k - n_k) + Dk^4 \phi_k \ , \tag{3.31}$$

where $k^2 = k_x^2 + k_y^2$. Rearranging and combining these two equations in such a way as to eliminate ϕ_k/n_k, we obtain the dispersion relation

$$\omega^2 + i\omega \left[\alpha(1 + 1/k^2) + 2Dk^2)\right] - \alpha D(1 + k^2) - D^2 k^4 - i\frac{\alpha\kappa k_y}{k^2} = 0 \ . \tag{3.32}$$

In the limit of no dissipation $D = 0$, this becomes

$$\omega^2 k^2 + i\omega\alpha(k^2 + 1) - i\alpha\kappa k_y = 0 \ , \tag{3.33}$$

and in the limit $\alpha \to \infty$, the normal drift wave dispersion relation,

$$\omega = \frac{\kappa k_y}{k^2 + 1} \ , \tag{3.34}$$

is obtained. Taking the long wavelength limit ($k^2 \to 0$) gives $\omega = \kappa k_y$, which implies that the drift waves propagate in the poloidal y direction with phase velocity $U = \kappa$ (normalised units). The quadratic dispersion relation, equation 3.33, can be solved to give a real and imaginary part,

$$\omega = \omega_R + i\gamma \ , \tag{3.35}$$

where the real part is

$$\omega_R = \frac{1}{2\sqrt{2}}\sqrt{a}\sqrt{\sqrt{a^2+b^2}-a} \ , \tag{3.36}$$

and the imaginary part, or growth rate, is

$$\gamma = -\frac{1}{2}a + \frac{1}{2\sqrt{2}}\sqrt{a}\sqrt{\sqrt{a^2+b^2}+a} \ , \tag{3.37}$$

with

$$a = \alpha(1 + 1/k^2) \ , \tag{3.38}$$

and

$$b = \frac{4\kappa k_y}{1+k^2} \ . \tag{3.39}$$

In the following example, the analytical solution to the dispersion relation is compared to simulation results. The parameters of the HW model are set to $\alpha = 0.5$ and $\kappa = 1$, figure 3.2 shows the resulting real and imaginary parts of the solution to the analytical dispersion relation (equations 3.36 and 3.37). As can be seen, the largest amplitude wave and largest growth rate are located close to $k_x = 0$ and $k_y = 1$.

The same parameters are used in a run of the HAWK code. The time step is set to $\Delta t = 0.01$ and the grid is doubly periodic with 512×512 points spaced by $\Delta = 0.125$. The initial condition is a sum of low amplitude Fourier modes with amplitudes such that $|\phi_k| \sim k^{-3}$. Since we are interested in the linear dispersion relation, nonlinear terms in the code are switched off and viscocity is not applied ($D = 0$). The growth rate is calculated using the ratio of the amplitudes of the Fourier modes ϕ_k at time t_2 and t_1,

$$\gamma(k_x, k_y) = \frac{1}{t_2 - t_1} \log\left(\frac{|\phi_k(k_x, k_y; t_2)|}{|\phi_k(k_x, k_y; t_1)|}\right) \ . \tag{3.40}$$

Figure 3.3 shows the calculated linear growth rate. The agreement with the analytical results (figure 3.2(b)) is excellent, indicating that the HAWK code is working well.

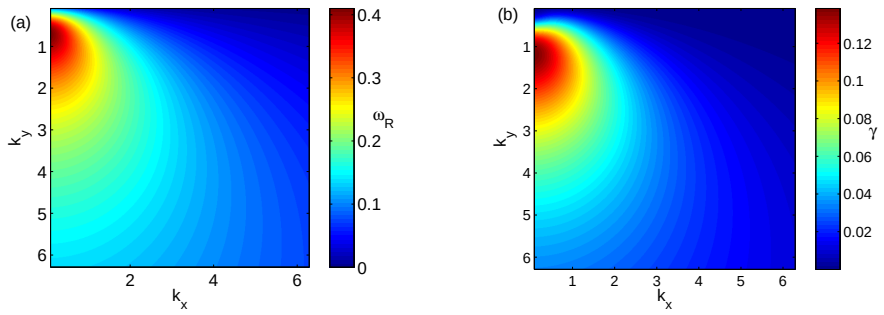

Figure 3.2: (a) Real and (b) imaginary parts of the solution to the HW analytical dispersion relation (equation 3.33) with $\alpha = 0.5$ and $\kappa = 1.0$.

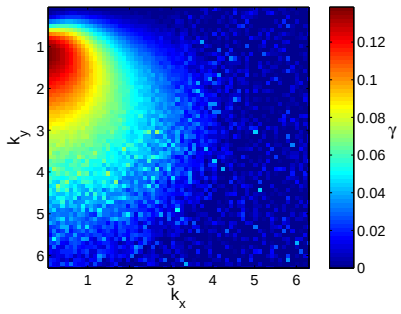

Figure 3.3: Linear growth rate measured in the HAWK code using parameters $\alpha = 0.5$ and $\kappa = 1.0$.

3.4.2 Energy and enstrophy conservation

Evolution equations for the energy E,

$$E = \frac{1}{2}\int \left(n^2 + (\nabla\phi)^2\right)\, dV \ , \tag{3.41}$$

and generalised enstrophy W,

$$W = \frac{1}{2}\int (n - \nabla^2\phi)^2\, dV \ , \tag{3.42}$$

can be obtained by manipulation and integration of the Hasegawa-Wakatani equations,

$$\frac{d}{dt}E = \kappa\Gamma_{n0} - D_\alpha + D_E \ , \tag{3.43}$$

$$\frac{d}{dt}W = \kappa\Gamma_{n0} + D_W \ . \tag{3.44}$$

Here,

$$\Gamma_{n0} = -\int n\frac{\partial\phi}{\partial y}\, dV \ , \tag{3.45}$$

is the total radial $E \times B$ density flux, which acts as the system's source, while

$$D_\alpha = \alpha\int (\phi - n)^2\, dV \ , \tag{3.46}$$

is a sink term due to the parallel current. D_E and D_W are sink terms due to the numerical dissipation and their form depends on the type of dissipation used,

$$D_E = \int \left[n\mathcal{D}(n) - \phi\mathcal{D}(\nabla^2\phi)\right]\, dV \ , \tag{3.47}$$

$$D_W = \int (n - \nabla^2\phi)\mathcal{D}(n - \nabla^2\phi)\, dV \ . \tag{3.48}$$

The energy E can be split into components which we refer to as potential energy $E_P = 1/2\int n^2\, dV$ and kinetic energy $E_K = 1/2\int(\nabla\phi)^2\, dV$.

In the following example, the parameters of the HW model are set to $\alpha = 0.5$ and $\kappa = 1$ and the viscocity is Newtonian with coefficient $D = 0.01$. The time step is $\Delta t = 0.01$ and the grid is doubly periodic with 512×512 points spaced by $\Delta = 0.125$. The simulation is initialised with low amplitude ($\sim 10^{-3}$) random noise in density and

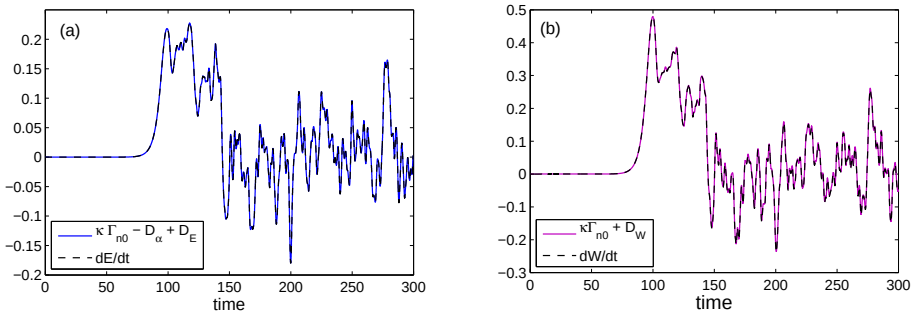

Figure 3.4: (a) Energy and (b) enstrophy conservation in the HAWK code: equations 3.43 and 3.44.

potential and is run for 300 normalised units of time (i.e. 30000 time steps). At each time step, the quantities in equations 3.43 and 3.44 are recorded. In figure 3.4(a) $\kappa\Gamma_{n0} - D_\alpha + D_E$ and dE/dt are plotted as functions of time and in figure 3.4(b) $\kappa\Gamma_{n0}+D_W$ and dW/dt are plotted. In both cases the time series overlap, indicating that the relations 3.43 and 3.44 are holding, and the code is conserving energy and enstrophy well. Error time series are estimated by calculating the differences and dividing by the standard deviation. In this case and in the rest of this thesis, the error is typically below 1%. For the narrow range of parameters used in this thesis, the code has been checked for convergence by doubling and halving the grid resolution and size and comparing the power spectra.

3.5 HAWK simulation

The aim of this section is to demonstrate the typical output of the HAWK code. Figure 3.5 shows snapshots of the density n and potential ϕ along with the time series of energy E taken from the run of the HAWK code described in the previous section. The energy time series begins to rise exponentially after a short transient which is due to the initial conditions. The rise in E is due to the excitation of drift waves by the drift wave linear instability. At time $t = 10$, density and potential have begun to form coherent structures from the random initial conditions. At time $t = 30$ drift waves, extended in

the x direction and propagating in the y direction are observed. The amplitude of these drift waves continues to increase exponentially until around $t = 100$ when nonlinear effects become important and E saturates. The nonlinear terms act to distribute energy in k space by wave-wave interactions and by time $t = 300$ quasi-stationary turbulence dominated by turbulent vortices is observed.

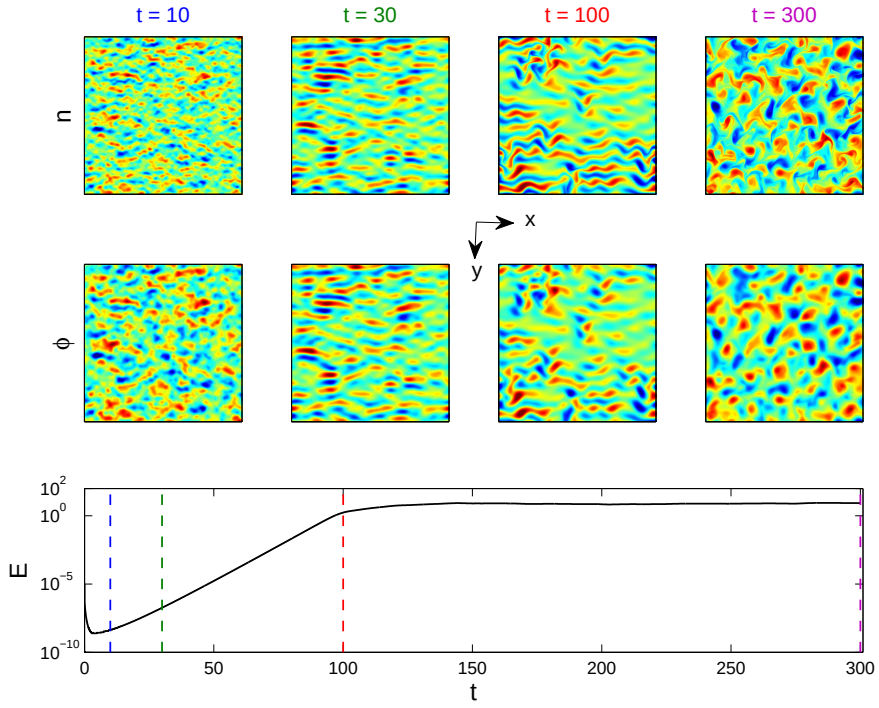

Figure 3.5: Snapshots of density n and potential ϕ and time series of energy E taken from the HAWK code. The dashed lines in the E time series correspond to the times at which snapshots are taken.

The HW equations can be modified to include extra physics and the effect of the modification can be determined by comparison. In the next sections, we consider the effects of non-uniform magnetic field strength and zonal flows.

3.6 Zonal flows

The nonlinear nature of drift wave turbulence dynamics distributes energy extracted from the background density gradient into modes with different wave numbers. It has been observed that some of the energy is deposited into small wave number modes, generating large flows which in tokamaks manifest as poloidally extended and radially localised coherent structures. These modes, with finite radial wave numbers but vanishing poloidal and toroidal numbers ($m = n = 0$), have been termed zonal flows. Importantly, zonal flows emerge as a generic feature of many models independent of plasma conditions or the geometry, and are a good example of self-organisation that can occur in complex systems with nonlinear interactions on many spatio-temporal scales [Diamond et al., 2005].

It has been noted that in tokamaks, the zonal components of the potential and density do not contribute to the parallel current [Dorland and Hammett, 1993] and in the standard formulation of the equations (3.19 and 3.20), zonal flows are damped. Modified equations, which allow the self-generation of zonal flows, are obtained by removing the zonal components from the parallel coupling terms [Numata et al., 2007]:

$$\frac{\partial n}{\partial t} = -\kappa \frac{\partial \phi}{\partial y} + [n, \phi] + \alpha(\tilde{\phi} - \tilde{n}) \ , \tag{3.49}$$

$$\frac{\partial \omega}{\partial t} = [\omega, \phi] + \alpha(\tilde{\phi} - \tilde{n}) \ , \tag{3.50}$$

where $\tilde{\phi} = \phi - \langle \phi \rangle$ and $\tilde{n} = n - \langle n \rangle$ are the non-zonal components and angular brackets denote the zonal components. In 2D the zonal component is simply the average over the poloidal y direction,

$$\langle f \rangle = \frac{1}{L_y} \int f dy \ . \tag{3.51}$$

We refer to equations 3.49 and 3.50 as the zonal-Hasegawa-Wakatani (ZHW) equations. The ZHW equations were used to study the generation and stability of zonal flows in Numata et al. [2007] and the interaction between drift wave turbulence and zonal flows in Scott [2005].

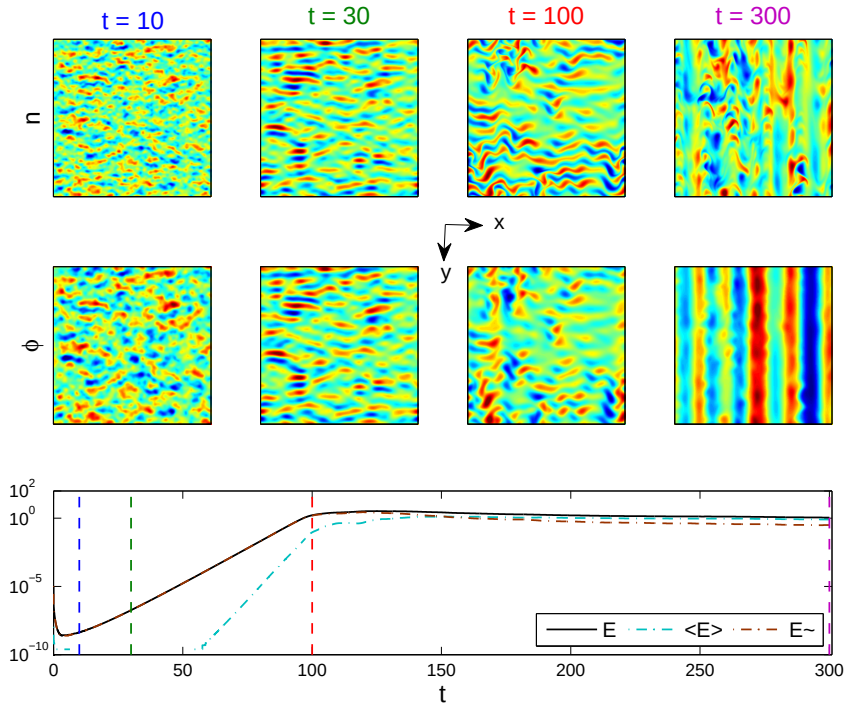

Figure 3.6: Snapshots of density n and potential ϕ and time series of energy E, zonal energy $\langle E \rangle$ and non-zonal energy $\tilde{E}$ taken from a HAWK simulation of the ZHW model (equations 3.49 and 3.50). The dashed lines in the E time series correspond to the times at which snapshots are taken.

Figure 3.6 shows snapshots of the density and potential taken from a HAWK simulation of the ZHW equations with the same parameters as the previous section. In the energy time series, the total energy E defined by equation 3.41 is plotted as well as the zonal energy

$$\langle E \rangle = \frac{1}{2} \int \left[\langle n \rangle^2 + \left(\frac{\partial \langle \phi \rangle}{\partial x} \right)^2 \right] dV \ , \tag{3.52}$$

and the non-zonal energy

$$\tilde{E} = E - \langle E \rangle = \frac{1}{2} \int \left[\tilde{n}^2 + (\nabla \tilde{\phi})^2 \right] dV \ . \tag{3.53}$$

The simulation begins in the same way as for the standard HW equations: linear drift waves grow exponentially until nonlinear effects become important. At around $t =$

100 the total energy saturates and turbulent vortices are observed. As the simulation develops, zonal flows are generated by some secondary instability. At around $t = 150$ the zonal energy $\langle E \rangle$ grows larger than the non-zonal energy $\tilde{E}$, by $t = 300$ zonal flows are dominant and are clearly observed in the snapshot of potential.

3.6.1 Zonal flow damping

In these 2D simulations of the ZHW model, the majority of the energy finds its way into zonal flows and zonal flows are dominant. This follows from the efficiency of the zonal flow generation in 2D turbulence [Scott, 2005]. In 3D, however, energy tends to find an equilibrium between zonal flows and turbulence [Peeters, 2009]. In order to mimic this in a 2D simulation, we artificially set the kinetic energy of the zonal flows equal to the kinetic energy of the non-zonal drift wave turbulence at each time step in the saturated turbulent state of the ZHW model,

$$\langle E \rangle_K \equiv \frac{1}{2} \int \left(\frac{\partial \langle \phi \rangle}{\partial x} \right)^2 dV = \frac{1}{2} \int (\nabla \tilde{\phi})^2 \, dV \equiv \tilde{E}_K \ . \tag{3.54}$$

Numerically, this is achieved by multiplying the zonal component of potential $\langle \phi \rangle$ by a factor of A at every time step, once the zonal energy has grown equal to the non-zonal energy where

$$A = \sqrt{\frac{E_K}{\langle E \rangle_K} - 1} \ . \tag{3.55}$$

Figure 3.7 shows snapshots of the potential and density taken from a HAWK simulation of this damped-zonal-Hasegawa-Wakatani (DZHW) model, using the same parameters as before. The total zonal energy $\langle E \rangle$ remains lower than the non-zonal energy $\tilde{E}$ throughout the simulation. By time $t = 300$, zonal flows and turbulent vortices coexist in a quasi-stationary state.

3.6.2 Zonal flows as transport barriers

Zonal flows are thought to act as transport barriers in that they improve the confinement of plasma. Here, we illustrate this effect using a simple modification to the HW

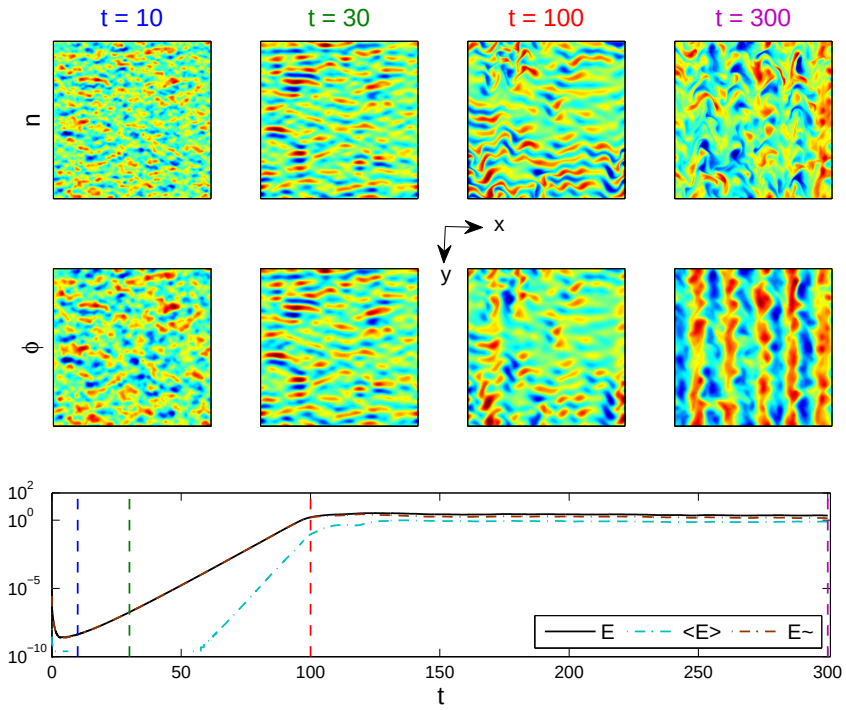

Figure 3.7: Snapshots of density n and potential ϕ and time series of energy E, zonal energy $\langle E \rangle$ and non-zonal energy $\tilde{E}$ taken from a simulation of the DZHW model (equations 3.49 and 3.50 with the constraint of equation 3.54). The dashed lines in the E time series correspond to the times at which snapshots are taken.

equations. The equations we consider are

$$\frac{\partial n}{\partial t} = \alpha(\phi - \tilde{n}) + [n, \phi] \ , \tag{3.56}$$

and

$$\frac{\partial}{\partial t}(\nabla^2 \phi) = \alpha(\phi - \tilde{n}) + \left[\nabla^2 \phi, \phi\right] \ , \tag{3.57}$$

where n now includes background and fluctuating parts, $n = n_0 + \tilde{n}$ and

$$n_0 = \frac{1}{L_y} \int n dy \ . \tag{3.58}$$

We also consider the equations

$$\frac{\partial n}{\partial t} = \alpha(\tilde{\phi} - \tilde{n}) + [n, \phi] \ , \tag{3.59}$$

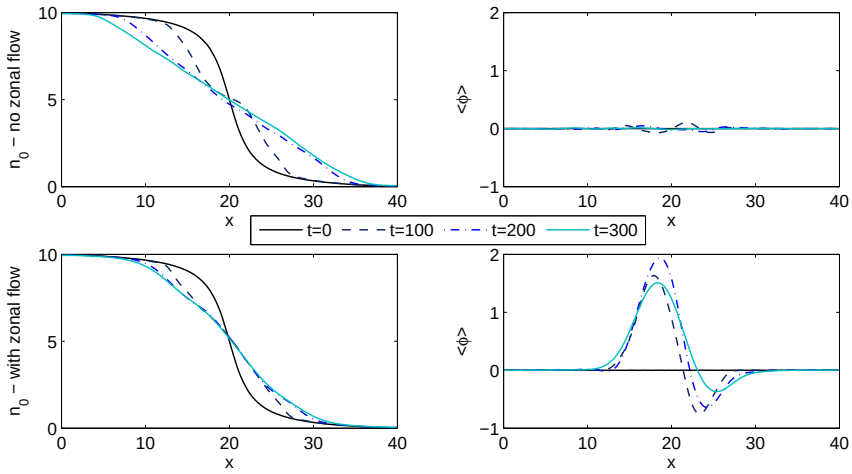

Figure 3.8: Density profile n_0 relaxation with (bottom) and without (top) zonal flows.

and

$$\frac{\partial}{\partial t}(\nabla^2\phi) = \alpha(\tilde{\phi} - \tilde{n}) + \left[\nabla^2\phi, \phi\right] \ , \tag{3.60}$$

which allow the generation of zonal flows. Here $\tilde{\phi}$ represents the non-zonal components of ϕ, $\tilde{\phi} = \phi - \langle\phi\rangle$. The simulation is initialised with a background density profile of the form $n_0 \sim \arctan(ax + b)$, where a and b are constants. The poloidal boundary conditions are periodic, while the vorticity $\nabla^2\phi$ is set to zero and the density n has no-flux ($\partial n/\partial x = 0$) at the radial boundaries. This allows the density profile n_0 to evolve freely by itself. A square grid of side $L = 40$ with 256×256 grid points is used, the parameter α is set to 0.5 and the viscosity is Newtonian with constant $D = 0.01$.

Two simulations are run, one with zonal flows allowed to self-generate and one with zonal flows damped. In figure 3.8 the evolution of the density profile n_0 is plotted along with the zonal component of potential $\langle\phi\rangle$ for both cases. In both cases, the density profile relaxes in time as density is transported down the gradient. At the end of the simulation $t = 300$, the density profile n_0 is steeper for the case with zonal flows present. This is due to the zonal flow acting as a barrier to the transport of density. In the presence of zonal flows, the radial flux of density is reduced.

A shear flow such as a zonal flow can stabilise the original instability. The drift wave instability is suppressed in the HW model when there is poloidal flow U that satisfies

$$\frac{\partial^2 U}{\partial x^2} \geq \kappa k^2 \ , \tag{3.61}$$

where k is the wavenumber of the turbulent fluctuations.

3.7 Non-uniform magnetic field strength

When deriving the HW equations, the magnetic field is assumed to be uniform. In tokamaks, however, the toroidal magnetic field strength declines with radial distance from the axis of symmetry. Thus we repeat the derivation of the HW equations with the assumption that the magnetic field strength varies in the radial x-direction, $\mathbf{B} = B(x)\hat{\mathbf{z}}$. With this assumption, the divergence of the $E \times B$ and diamagnetic velocities, $\nabla \cdot \mathbf{v_E}$ and $\nabla \cdot \mathbf{v}_{de}$, no longer vanish, leading to extra terms in the equations. We obtain

$$\frac{\partial n}{\partial t} = -\kappa \frac{\partial \phi}{\partial y} + \alpha(\phi - n) + [n, \phi] + C\frac{\partial}{\partial y}(\phi - n) \ , \tag{3.62}$$

and

$$\frac{\partial}{\partial t}(\nabla^2 \phi) = \alpha(\phi - n) + \left[\nabla^2 \phi, \phi\right] - C\frac{\partial n}{\partial y} \ , \tag{3.63}$$

where $C = -\partial \ln B / \partial x$ is assumed to be constant and characterises the gradient of $B(x)$. We refer to equations 3.62 and 3.63 as the curvature-Hasegawa-Wakatani (CHW) equations, since in tokamaks the non-uniform magnetic field strength is associated with toroidal curvature. The standard HW equations are recovered from the CHW equations when $C = 0$. The extra terms at finite C represent interchange forcing due to the non-uniform magnetic field and compressibility of the $E \times B$ and diamagnetic velocities.

Linearising and Fourier decomposing the CHW equations, we obtain for plane waves $\sim \exp\left[i(k_x x + k_y y - \omega t)\right]$,

$$\omega n_k = (\kappa - C)k_y \phi_k + C k_y n_k + i\alpha(\phi_k - n_k) \ , \tag{3.64}$$

and

$$\omega k^2 \phi_k = -C k_y n_k - i\alpha(\phi_k - n_k) \ . \tag{3.65}$$

Eliminating n_k/ϕ_k we obtain the dispersion relation,

$$\omega^2 k^2 + \omega \left[i\alpha(1+k^2) - C k_y k^2 \right] + k_y(\kappa - C)\left[C k_y - i\alpha \right] = 0 \ , \tag{3.66}$$

which, in the limit $\alpha \gg 1$, becomes

$$\omega = \frac{(\kappa - C)k_y}{1+k^2} \ , \tag{3.67}$$

which is the usual drift-wave dispersion relation, modified by a factor of $(\kappa - C)/\kappa$. In the long wavelength limit ($k^2 \to 0$), the linear drift waves propagate in the poloidal y direction with phase velocity

$$U = \kappa - C \ . \tag{3.68}$$

Restoring the units, $U = u_{de} - u_{\nabla B}$, where $u_{de} = -(T_e/eBn_0)(\partial n_0/\partial x)$ is the electron diamagnetic drift velocity and $u_{\nabla B} = -(T_e/eB^2)(\partial B/\partial x)$ is the modification due to ∇B effects. Since the ratio of two complex numbers can be expressed as an amplitude and a phase shift, an expression for the linear phase shifts between n and ϕ can be found by eliminating ω in equations 3.64 and 3.65 instead of n_k/ϕ_k. In the long wavelength limit, we obtain

$$\theta = \arctan\left(\frac{C k_y}{\alpha}\right) \ . \tag{3.69}$$

Thus, in the linear regime, the parameter C alters the poloidal velocity of the drift waves and the phase shift between density n and potential ϕ. In the nonlinear regime, these features are retained.

The evolution equation for the generalised enstrophy W (equation 3.44) is also modified for the CHW model,

$$\frac{d}{dt} W = (\kappa - C)\Gamma_{n0} + D_W \ . \tag{3.70}$$

This equation requires $\kappa > C$, so that Γ_{n0} is a source of W. The Lagrangian conserved quantity, potential vorticity, becomes

$$\Pi = (\nabla^2 \phi - n + (\kappa - C)x) \ . \tag{3.71}$$

The approximate conservation of this quantity plays an important role in the dynamics of turbulent structures, as described in the next section.

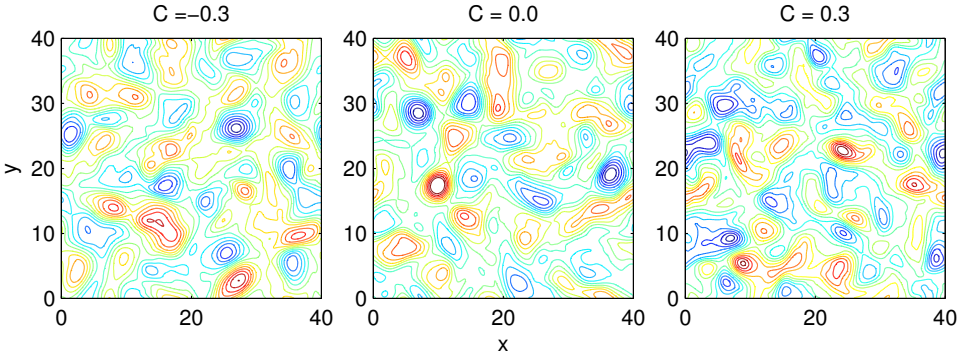

Figure 3.9: Contours of potential ϕ in the quasi-stationary saturated turbulent state of the CHW system for different values of $C = -\partial \ln B/\partial x$.

Figure 3.9 shows typical snapshots of the potential ϕ in the quasi-stationary saturated turbulent state for $C = [-0.3, 0, 0.3]$ with $\alpha = 0.5$ and $\kappa = 1$. Unlike the zonal flow case, snapshots of potential and density do not illustrate well the effect of the parameter C. In fact, the main effects of C are to change the dynamics of the turbulent vortices and to change statistical properties of the turbulence. The statistical changes are explored in the next chapter. In the next section, we consider the dynamics of a single nonlinear structure in the CHW model in order to illustrate the effect of C.

3.7.1 Propagation of nonlinear structures

We are interested in the effect of changing the magnetic field inhomogeneity (i.e. changing the value of the parameter C in equations 3.62 and 3.63), and choose the set $C = [-0.3, 0, 0.3]$ as representative of different locations with respect to an equilibrium magnetic field. When the parameters κ and C are opposite in sign, the gradients of magnetic field strength and of background density point in opposite directions; as is the case on the inboard side of a tokamak. When κ and C share the same sign, the gradients of magnetic field strength and of background density point in the same direction; as is the case on the outboard side of a tokamak. In the latter case, perturbations in density

lead to radial $E \times B$ motion due to the ∇B plasma polarization and the plasma is said to be interchange unstable. In the former case, the plasma is interchange stable. In reality, the inboard and outboard sides of a tokamak are connected by helically wound magnetic field lines. This three dimensional effect results in ballooning type modes and is beyond the scope of this model. Other parameters in the CHW model are set to $\alpha = 0.5$ and $\kappa = 1$, viscocity is Newtonian with $D = 0.01$ and the grid has 256×256 points space by $\Delta = 40/256$.

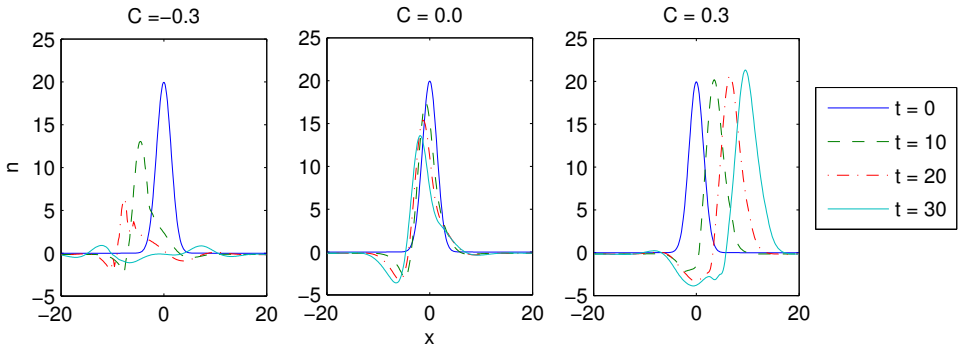

Figure 3.10: Radial evolution of density n of nonlinear structures for different values of $C = -\partial \ln B/\partial x$. The directions of the gradients of background magnetic field and density are opposed for negative C and coincident for positive C.

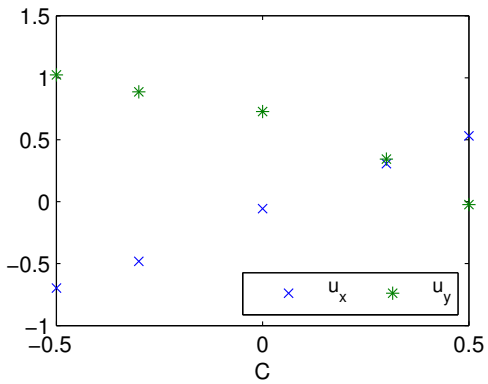

Figure 3.11: Radial u_x and poloidal u_y velocity components of positive amplitude nonlinear structures shown in Fig. 3.10 for different values of C.

The simulation is initialised with a Gaussian pulse monopole structure, shown as a dark blue solid line in figure 3.10, with $n = \phi$ in the centre of the computational

box, whose positive amplitude is large enough to cause nonlinear effects. We follow this structure and in figure 3.10 show the radial evolution of its density n for $C = [-0.3, 0.0, 0.3]$. For the standard HW case ($C = 0$) the structure propagates slowly in the negative x direction and exponentially decays slowly with time, in agreement with a similar study in [Naulin, 2002]. For CHW with $C = -0.3$ the structure propagates in the negative x direction but decays at a much faster rate. For $C = 0.3$ the structure propagates in the positive x direction – down the background density gradient – and grows in time. When $C = 0.3$, negative amplitude nonlinear structures propagate in the negative x direction and grow in time; when $C = -0.3$ they propagate in the positive x direction and decay with time. Thus when $C = 0.3$, nonlinear perturbations of density and radial velocity are correlated, and when $C = -0.3$ they are anticorrelated.

Figure 3.11 shows how the radial u_x and poloidal u_y velocities of the positive amplitude structure, shown in figure 3.10, change for a wider range of C. We find that the radial velocity increases with C while the poloidal velocity decreases with C. We note that in the radial x direction, positive and negative amplitude structures propagate in opposite directions, so that the radial velocity of a negative amplitude structure is approximately $-u_x$. In the poloidal y direction, however, positive and negative amplitude structures propagate in the same direction with the same velocity u_y. Thus the change in u_y with C may be understood in terms of the linear approximation embodied in equation 3.68: increasing C decreases the poloidal flow velocity. In the fully developed turbulence we also find that increasing C decreases the poloidal flow velocity. Further understanding of the radial propagation of structures can be obtained by considering the potential vorticity Π defined in equation 3.71 [Naulin, 2002; Basu et al., 2003a]. Taking the time derivative of equation 3.71 gives

$$\frac{d}{dt}x \equiv u_x = -\frac{\partial \phi}{\partial y} = -\frac{1}{\kappa - C}\frac{d}{dt}\zeta \ , \tag{3.72}$$

where $\zeta = \nabla^2\phi - n$ is the fluid part of the potential vorticity and u_x is the radial component of the $E \times B$ velocity of the structure. We note that $(\kappa - C)$ must be positive by equation 3.44, and negative vorticity $\nabla^2\phi$ is associated with positive density

structures and vice-versa [Naulin, 2002]. In the inviscid limit, a fluid structure will propagate consistent with equation 3.72, in order to keep Π constant.

3.7.2 Computations in polar coordinates

It is also possible to perform HAWK simulations in an annulus using polar coordinates (r, θ). The CHW equations in this geometry are

$$\frac{\partial n}{\partial t} = -\kappa \frac{1}{r}\frac{\partial \phi}{\partial \theta} + \alpha(\phi - n) + \frac{1}{r}\left[n, \phi\right] + C\left[\frac{1}{r}\frac{\partial}{\partial \theta}(\phi - n)\cos\theta + \frac{\partial}{\partial r}(\phi - n)\sin\theta\right] , \tag{3.73}$$

and

$$\frac{\partial}{\partial t}(\nabla^2 \phi) = \alpha(\phi - n) + \frac{1}{r}\left[\nabla^2\phi, \phi\right] - C\left[\frac{1}{r}\frac{\partial n}{\partial \theta}\cos\theta + \frac{\partial n}{\partial r}\sin\theta\right] . \tag{3.74}$$

Note that the curvature terms are now functions of both coordinates, r and θ. This leads to turbulent structures localised on the 'outboard side' of the annulus, as shown in figure 3.12.

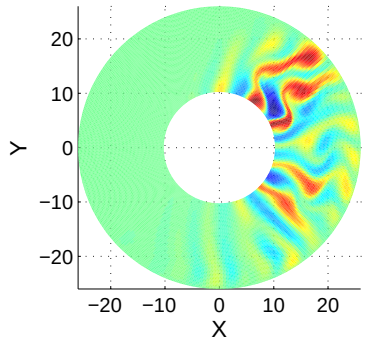

Figure 3.12: Snapshot of density fluctuations from HAWK simulation of the CHW equations in polar coordinates.

Chapter 4

Statistical properties of drift wave turbulence

4.1 Introduction

In this chapter, the statistical properties of the turbulent fluctuations produced by HAWK simulations are characterised. Turbulent fluctuations are difficult to describe in the dynamical sense, but statistical features are often robust and reproducible. Modelling turbulence with mean value quantities may not be suitable due to the presence of long lived coherent structures and more appropriate methods must be used. Here, we study the probability density function, structure functions, the bispectrum and transfer functions. The drawback of statistical analyses is the difficulty in connecting the observe statistics with the physical processes involved.

4.2 Turbulent flux PDF

In experiment, properties of turbulence are often determined by probe measurements of the turbulent $E \times B$ radial density flux,

$$\Gamma_n = nv_x = -n\frac{\partial \phi}{\partial y} \ . \tag{4.1}$$

We therefore record this quantity along with density n, potential ϕ and radial velocity $v_x = -\partial\phi/\partial y$ at one grid-node (i.e. point-wise) for the entire duration of the quasi-stationary turbulent state of the HW system. From the Γ_n time series we compute its probability density function (PDF) $P(\Gamma_n)$, and quantify departures of the distribution from Gaussian with skewness S and kurtosis K.

We are interested in the effect of the parameters of the HW model, κ and α, as well as the parameter C of the CHW model, on the PDF $P(\Gamma_n)$. In the following sections we consider a base case with parameters $\kappa = 1$, $\alpha = 0.5$ and $C = 0$, using a doubly periodic grid with 256×256 grid points spaced by $\Delta = 40/256$, a time step of $\Delta t = 0.01$ and Newtonian viscosity with $D = 0.01$. The effects of altering the various parameters are then determined by varying one parameter and comparing with this base case.

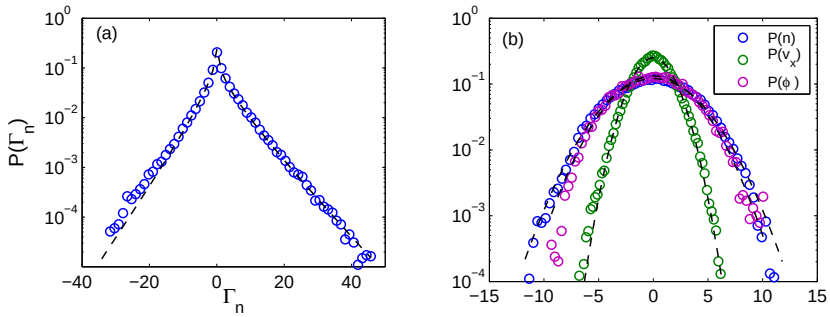

Figure 4.1: (a) PDF of point-wise radial density flux $\Gamma_n = nv_x$ for the base case, as described in the text. The dashed lines are the PDFs calculated using equations 4.2 and 4.3 and probe data from the simulation. (b) PDF of point-wise density n, radial velocity v_x and potential ϕ for the base case. The dashed lines are Gaussian fits to the data.

The PDF of turbulent flux $P(\Gamma_n)$ for the base case is shown in figure 4.1(a) along with the PDFs of density $P(n)$, radial velocity $P(v_x)$ and potential $P(\phi)$ in figure 4.1(b). In figure 4.1(b) Gaussian PDFs fitted to the data are overlaid with dashed lines demonstrating that n, v_x and ϕ are close to Gaussian. It is clear, however, that Γ_n is non-Gaussian. For the case where the amplitudes of the fluctuations in radial velocity v_x and density n are exactly Gaussian, the PDF of radial turbulent flux $\Gamma_n = nv_x$ can

be shown to be [Carreras et al., 1996]

$$P(\Gamma_n) = \frac{1}{\pi}\frac{\sqrt{1-\gamma^2}}{\sigma_v \sigma_n} K_0\left(\frac{|\Gamma_n|}{\sigma_v \sigma_n}\right) \exp\left(-\gamma \frac{\Gamma_n}{\sigma_v \sigma_n}\right) , \tag{4.2}$$

where σ_v and σ_n are the standard deviations of velocity and density fluctuations, K_0 is the modified Bessel function of the second kind and γ is a parameter that measures the correlation between v_x and n,

$$\gamma = -\frac{\langle v_x n \rangle}{\langle v_x^2 \rangle^{1/2} \langle n^2 \rangle^{1/2}} \equiv -\cos\Phi , \tag{4.3}$$

where Φ is the average relative phase between v_x and n. The skewness of the PDF can be calculated [Carreras et al., 1996] as

$$S = -2\gamma \frac{3+\gamma^2}{(1+\gamma^2)^{3/2}} , \tag{4.4}$$

which depends on the parameter γ only. The shape of this PDF therefore depends on the standard deviation of the density and velocity fluctuations as well as the degree of their correlation. In figure 4.1(a) we overlay with dashed lines the PDFs calculated using equations 4.2 and 4.3 and probe data from the simulation. Good agreement is found, indicating that the quantities v_x and n are indeed close to Gaussian.

4.2.1 Varying κ

We are interested in the effect on the PDF $P(\Gamma_n)$ of changing the parameter κ and therefore, all other parameters are set to base case values. In figure 4.2(a) we plot $P(\Gamma_n)$ for three different values of κ. All three PDFs are clearly non-Gaussian and are skewed towards positive radial flux. We note that non-Gaussian PDFs of the turbulent flux and/or density are regularly measured in the edge region of experiments. We also show in figure 4.2(b), the relative phase between n and v_x, Φ, in figure 4.2(c) the average total flux Γ_{n0} and in figure 4.2(d) the rms values of n and v_x. We see that while the average flux Γ_{n0} and rms values $\langle v_x^2 \rangle^{1/2}$ and $\langle v^2 \rangle^{1/2}$ clearly increase with κ, the phase Φ does not change much with κ. This may be expected as the parameter κ controls the strength of the driving of the turbulence and should have no effect on the phase.

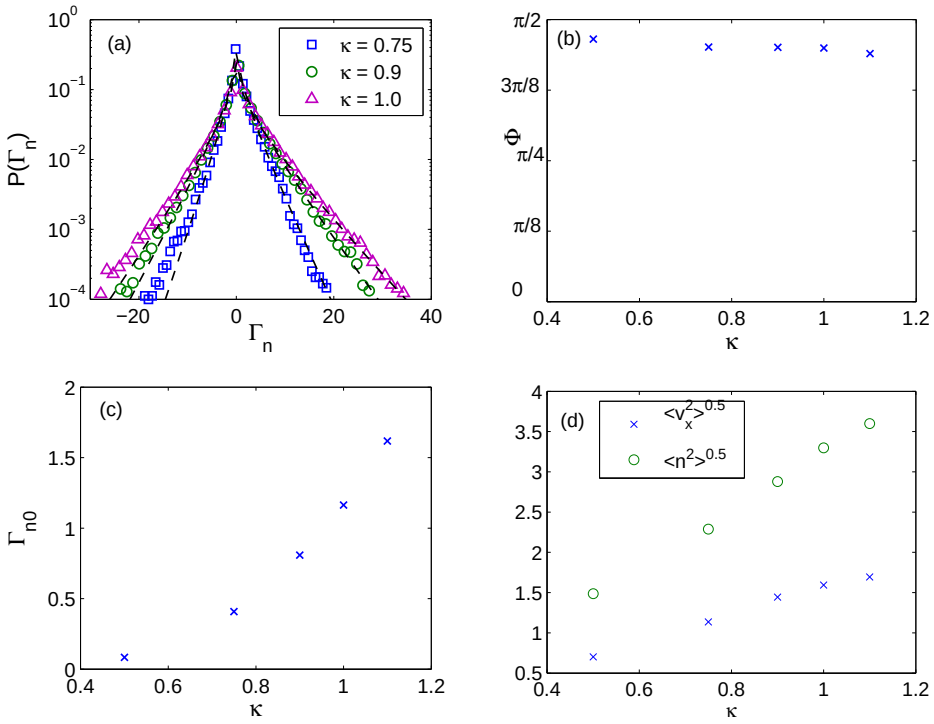

Figure 4.2: (a) PDF of point-wise radial density flux $\Gamma_n = nv_x$ for different values of κ. The dashed lines are the PDFs calculated using equations 4.2 and 4.3 and probe data from the simulation. (b) Relative phase between n and v_x, for different values of κ. (c) Average total flux Γ_{n0} for different κ. (d) rms values of n and v_x fluctuations.

4.2.2 Varying α

In figure 4.3(a) we plot $P(\Gamma_n)$ for three different values of α. We also show in figure 4.3(b), the relative phase between n and v_x, Φ, in figure 4.3(c) the average total flux Γ_{n0} and in figure 4.3(d) rms values of v_x and n. Interestingly, the average flux Γ_{n0} decreases with α, while the phase Φ does not change much. One might expect that the phase Φ would change with α since a large value of α effectively ties together fluctuations in density n and potential ϕ. The results here suggest that the main effect of increasing α is to decrease the average flux Γ_{n0}. However, the parameter α has not been varied very much because of restrictions due to numerical stability. A study using a wider range of α would be of benefit here.

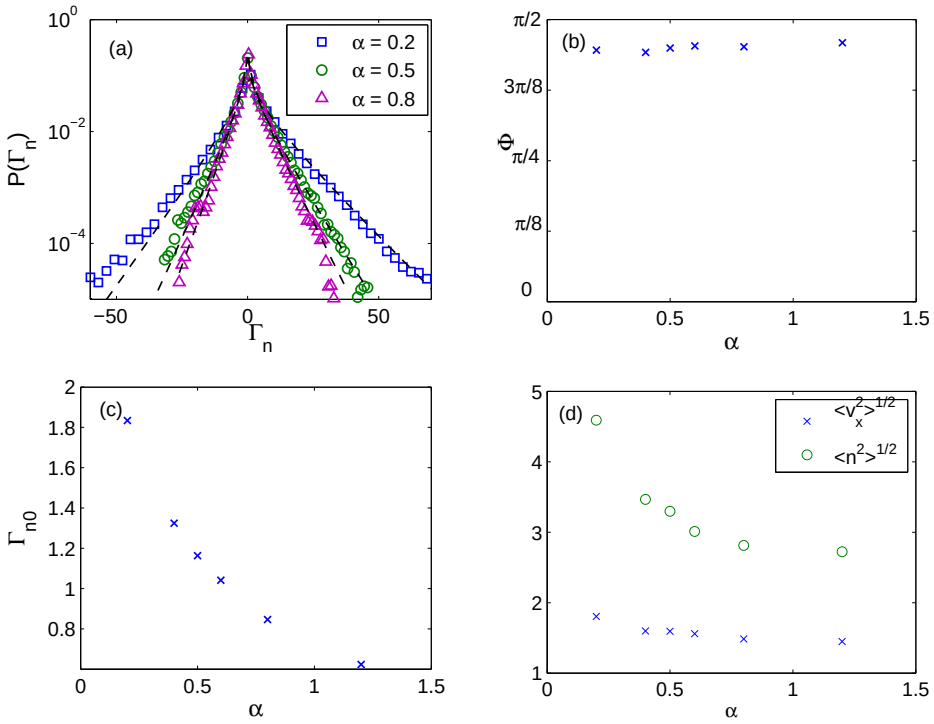

Figure 4.3: (a) PDF of point-wise radial density flux $\Gamma_n = nv_x$ for different values of α. The dashed lines are the PDFs calculated using equations 4.2 and 4.3 and probe data from the simulation. (b) Relative phase between n and v_x, for different values of α. (c) Average total flux Γ_{n0} for different α. (d) rms values of n and v_x fluctuations.

4.2.3 Varying C

We now focus on how the distribution of turbulent radial density flux Γ_n changes with the parameter controlling the magnetic field inhomogeneity $C = -\partial \ln B/\partial x$. Figure 4.4(a) shows the PDFs $P(\Gamma_n)$ for three different values of $C = [-0.3, 0.0, 0.3]$. All three PDFs are clearly non-Gaussian and are skewed towards positive radial flux. In figure 4.4(b), we plot the skewness S of the PDFs for a wider range of C. Increasing the parameter C, which corresponds to steepening the decline in magnetic field strength with radial distance, monotonically increases the positive radial skewness of Γ_n.

In figure 4.4(c) we plot the skewness and kurtosis of the distributions of point-wise measurements of density n, potential ϕ and radial velocity v_x for different values

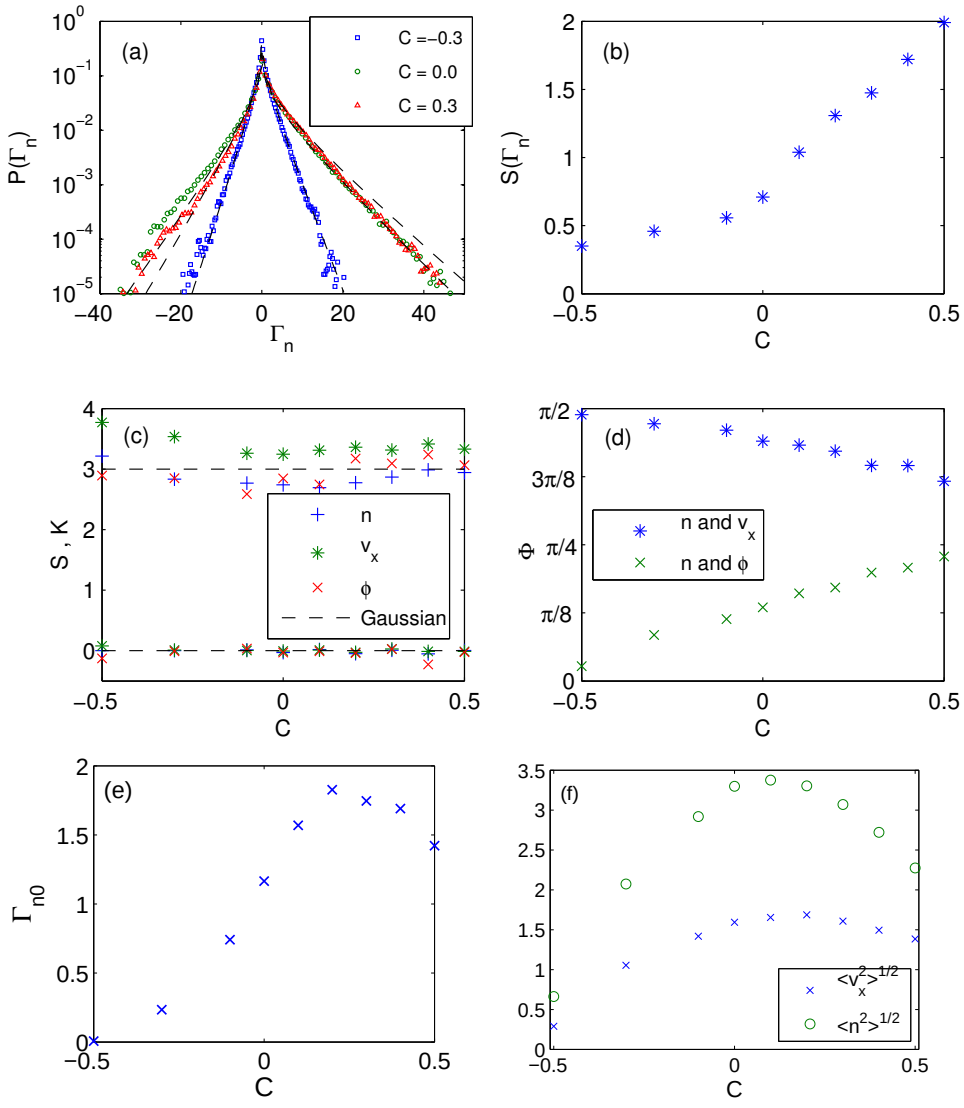

Figure 4.4: (a) PDFs and (b) skewness of PDFs of the point-wise radial density flux $\Gamma_n = nv_x$ for different values of C. The dashed lines over the PDFs are the PDFs calculated using equations 4.2 and 4.3 and probe data from the simulation. (c) Skewness and kurtosis of PDFs of point-wise density n, radial velocity v_x and potential ϕ. (d) Relative phase between n and v_x, and between n and ϕ, for different values of C. (e) Average total flux Γ_{n0} for different C. (f) rms values of n and v_x fluctuations.

of C in the CHW system. These quantities are very close to Gaussian for the full range of C, with radial velocity v_x showing the largest departure from Gaussian in its kurtosis. In figure 4.4(d) we plot the relative phase Φ between v_x and n, and also between ϕ and n, showing that Φ changes roughly linearly with C. We conclude that changing C alters the relative phase between fluctuations in density n and potential ϕ, which leads to the observed change in the skewness of the flux PDF. We note from equation 3.45 that an increase in the phase difference between n and ϕ should lead to an increase in the rate of radial $E \times B$ transport. A plot of the average flux Γ_{n0} as a function of C is displayed in figure 4.4(e). In figure 4.4(a) we overlay with dashed lines the PDFs calculated using equations 4.2 and 4.3 and probe data from the simulation. Moderately good agreement is found, with the biggest departures occurring for large positive values of Γ_n when $C = 0.3$ and large negative values of Γ_n when $C = 0$. This indicates that the quantities v_x and n are indeed close to Gaussian; however, large fluctuations may follow a different distribution.

In Section 3.7.1 it was concluded, from the propagation of nonlinear structures, that when $C = 0.3$, nonlinear perturbations of density and radial velocity are correlated, and when $C = -0.3$ they are anticorrelated. Insofar as the fully developed turbulence approximates to Gaussian statistics, it follows from equations 4.3 and 4.4 that the positive correlation of density and radial velocity will lead to a positive event in the time series of radial flux Γ_n and an increase in the skewness of the PDF $P(\Gamma_n)$. Similarly, negative correlation leads to negative flux events and lower skewness.

4.3 Structure function analysis

The analysis of the flux PDF in the previous section revealed that changing the parameter C in the CHW model fundamentally changes the properties of the turbulence. In this section, we apply structure function analysis to the same datasets. The mth order

structure function is defined as

$$S_m(d) = <\mid f(\mathbf{x} + d\hat{\mathbf{x}}) - f(\mathbf{x}) \mid^m> \quad . \tag{4.5}$$

When scaling is present $S_m \propto \tau^{\zeta(m)}$, and a plot of S_m versus d on a log-log scale will yield a straight line for each m with gradient $\zeta(m)$. Here, we perform the analysis using multiple snapshots of density or potential taken from the same HAWK simulation used in the previous section. The structure functions are therefore calculated using an average over space and time.

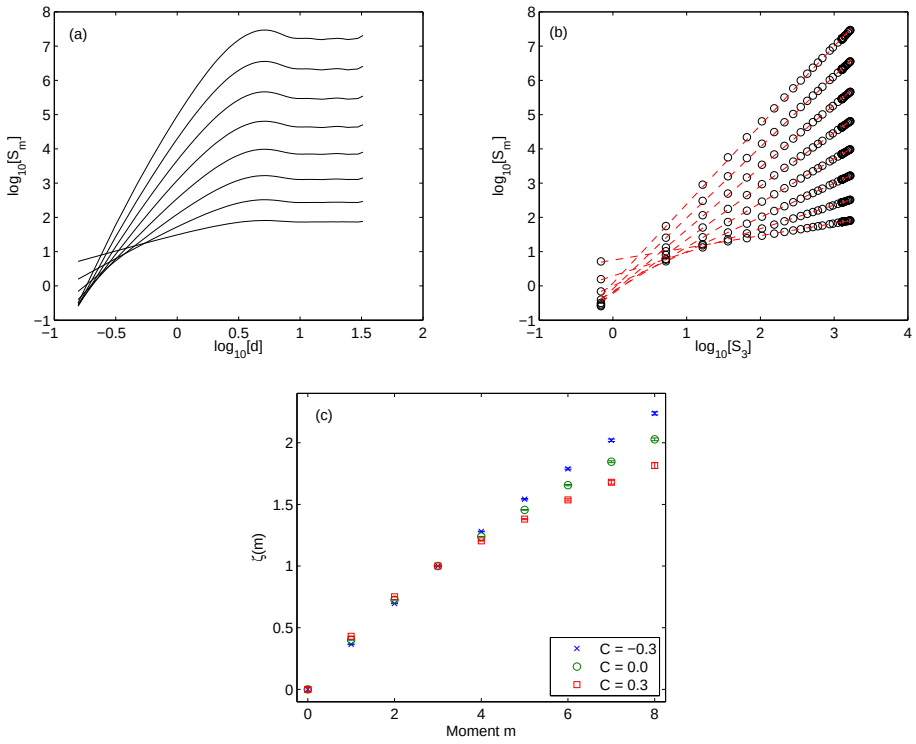

Figure 4.5: Structure function analysis of density data taken from the HAWK code. (a) Structure functions S_m of order $m = 1$ to $m = 8$ as a function of d for $C = -0.3$. (b) Extended self-similarity (ESS) analysis: structure functions S_m as a function of S_3 for $C = -0.3$. (c) Scaling exponents $\zeta(m)$ calculated using ESS structure functions for different values of C.

In figure 4.5(a) we plot structure functions S_m of order $m = 1$ to $m = 8$ as a function of d on a log-log scale for $C = -0.3$ using density n data. Scaling is present

for small values of d and is followed by saturation at large values of d. In order to extract scaling exponents $\zeta(m)$, we employ the extended self-similarity (ESS) technique [Benzi et al., 1993]. ESS was used in a structure function analysis of HW turbulence in [Futatani et al., 2008]. Here, we apply the technique to the CHW model. ESS involves plotting structure functions S_m as a function of S_3 instead of d and can significantly extend the region of scaling. In figure 4.5(b) we plot S_m as a function of the third order structure function S_3 and find that an extended region of scaling is revealed. Scaling exponents are obtained by linear regression of the ESS structure functions. The ESS analysis is performed for $C = [-0.3, 0.0, 0.3]$ and the scaling exponents $\zeta(m)$ are plotted in figure 4.5(c). We find that the functional form of $\zeta(m)$ is nonlinear and changes with C.

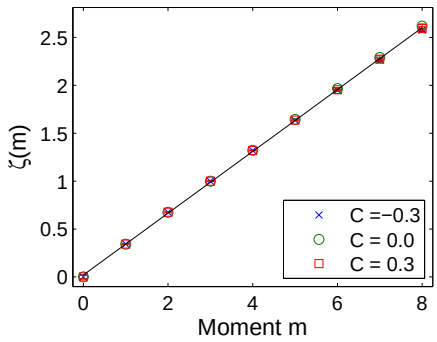

Figure 4.6: Structure function analysis of velocity data taken from the HAWK code: scaling exponents $\zeta(m)$ calculated using ESS structure functions for different values of C.

An identical analysis is performed using velocity $v(x, y) = (-\partial\phi/\partial y, \partial\phi/\partial x)$ data taken from the same set of HAWK simulations. Figure 4.6 shows the scaling exponents $\zeta(m)$ for different values of C. In contrast to the density results, $\zeta(m)$ is close to a linear function in m and does not change with C. The same results are found for structure functions of velocity components $v_x = -\partial\phi/\partial y$ and $v_y = \partial\phi/\partial x$ and potential ϕ. We conclude that, while velocity fluctuations remain self-similar for different values of C in the CHW model, the statistics of density fluctuations vary. This

may point towards the importance of density fluctuations in this system.

4.4 Higher order spectra

Higher order spectra can be used to look for the presence of wave-wave interactions, which are a signature of turbulence. The bispectrum measures the coherence of three wave interactions. Systems of the form

$$\frac{\partial u(x,t)}{\partial x} = f(u(x,t)) \ , \tag{4.6}$$

are considered, where u is the quantity of interest and f is a nonlinear function. Performing a Fourier transform, it is assumed that the system can be represented in terms of a Volterra series,

$$\frac{\partial u_p}{\partial x} = \Gamma_p u_p + \sum_{a,b} \Gamma_{ab} u_a u_b \delta_{a+b,p} + \sum_{a,b,c} \Gamma_{abc} u_a u_b u_c \delta_{a+b+c,p} + \cdots \ , \tag{4.7}$$

where δ is the Dirac delta function. In this representation, it is clear that the action of the system's nonlinearity is to couple each Fourier mode to every other through three-wave interactions, four-wave interactions and so on. For waves to interact, a resonance condition must be satisfied. For example, three-wave interactions between waves of frequency ω, ω_1, ω_2 and wavenumber $\mathbf{k}$, $\mathbf{k}_1$, $\mathbf{k}_2$ must satisfy the selection criteria $\omega = \omega_1 + \omega_2$ and $\mathbf{k} = \mathbf{k}_1 + \mathbf{k}_2$.

Multiplying equation 4.7 by the complex conjugate u_p^* and taking an expectation value gives [de Wit, 2003]

$$\langle \frac{\partial u_p}{\partial x} u_p^* \rangle = \Gamma_p \langle u_p u_p^* \rangle + \sum_{a+b=p} \Gamma_{ab} \langle u_a u_b u_{a+b}^* \rangle + \sum_{a+b+c=p} \Gamma_{abc} \langle u_a u_b u_c u_{a+b+c}^* \rangle + \cdots \ . \tag{4.8}$$

In this equation, the power spectrum is,

$$P(k_p) = \langle u_p u_p^* \rangle \ , \tag{4.9}$$

the bispectrum is

$$B(k_a, k_b) = \langle u_a u_b u_{a+b}^* \rangle \ , \tag{4.10}$$

and the trispectrum is

$$T(k_a, k_b, k_c) = \langle u_a u_b u_c u^*_{a+b+c} \rangle \ . \tag{4.11}$$

Higher order spectra determine the degree of phase coherence between waves which satisfy the selection criteria. Normalised quantities are the bicoherence,

$$b^2(k_a, k_b) = \frac{|B(k_a, k_b)|^2}{\langle |u_a u_b|^2 \rangle \langle |u_{a+b}|^2 \rangle} \ , \tag{4.12}$$

and tricoherence

$$t^2(k_a, k_b, k_c) = \frac{|T(k_a, k_b, k_c)|^2}{\langle |u_a u_b u_c|^2 \rangle \langle |u_{a+b+c}|^2 \rangle} \ , \tag{4.13}$$

which can take values between 0 and 1.

4.4.1 Bispectral analysis of HAWK data

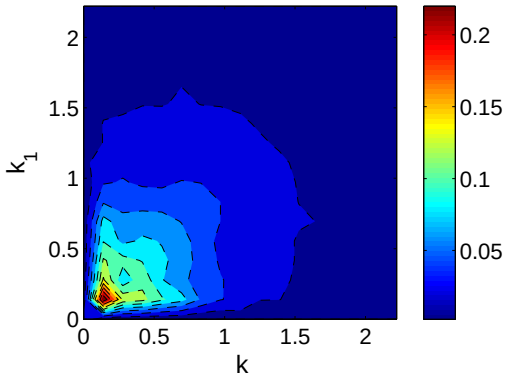

Figure 4.7: Bicoherence calculated using multiple snapshots of potential from a HAWK simulation of the HW equations.

We now calculate the bicoherence using data from a HAWK simulation. The data is taken from the base case HW run that was used in previous sections. The parameters of the HW model are set to $\alpha = 0.5$ and $\kappa = 1$, using a square box of side length $L = 40$ with 256×256 grid points and dissipation is Newtonian with $D = 0.01$. The

bicoherence is calculated using snapshots of potential in the quasi-stationary turbulent regime, with the average being taken in time.

With this two-dimensional data, the bispectrum is a four dimensional quantity: each of the $\mathbf{k}$ has components k_x and k_y, $B(k_x, k_y, k_{1x}, k_{1y})$. It is difficult, therefore, to plot the data in two-dimensional space. In figure 4.7 we plot the bicoherence $b^2(k, k_1)$ where $\mathbf{k} = \mathbf{k}_1 + \mathbf{k}_2$ and the data has been averaged over components k_x, k_y and k_{1x}, k_{1y}. Figure 4.7 confirms the presence of nonlinear wave-wave interactions in the HW model, with the strongest interactions occurring at low k.

4.4.2 Nonlinear transfer function

Having established that nonlinear wave-wave interactions are indeed present in the HW model, we now attempt to learn more about the nature of these interactions. We employ the method proposed by Camargo et al. [1995] which quantifies the spectral transfer of fluctuation energy between different k. This method has been used, for example, to give evidence of the dual-cascade in the HW model in [Manz et al., 2009a]. Here, we apply the technique to the CHW and ZHW models.

The evolution of the potential energy E_P, kinetic energy E_K and enstrophy W– which were introduced in Section 3.4.2–are separated into linear and nonlinear terms. In Fourier space,

$$\frac{\partial E_K(\mathbf{k})}{\partial t} = \sum_{\mathbf{k}_1} T_K(\mathbf{k} \leftarrow \mathbf{k}_1) + \text{ linear terms}, \tag{4.14}$$

$$\frac{\partial E_P(\mathbf{k})}{\partial t} = \sum_{\mathbf{k}_1} T_P(\mathbf{k} \leftarrow \mathbf{k}_1) + \text{ linear terms}, \tag{4.15}$$

and

$$\frac{\partial W(\mathbf{k})}{\partial t} = \sum_{\mathbf{k}_1} T_W(\mathbf{k} \leftarrow \mathbf{k}_1) + \text{ linear terms}. \tag{4.16}$$

Here, the terms $\sum_{\mathbf{k}_1} T(\mathbf{k} \leftarrow \mathbf{k}_1)$ are the nonlinear transfer functions which describe the nonlinear transfer of fluctuation energy to or from mode $\mathbf{k}$ due to interaction with

modes $\mathbf{k}_1$ and $\mathbf{k}_2$, where $\mathbf{k} = \mathbf{k}_1 + \mathbf{k}_2$. The functional forms, as given in [Camargo et al., 1995] are

$$T_K(\mathbf{k} \leftarrow \mathbf{k}_1) = 2\mathrm{Re}\left[(k_x k_{1y} - k_{1x} k_y)\phi^*_{\mathbf{k}} \omega_{\mathbf{k}_2} \phi_{\mathbf{k}_1}\right] \ , \tag{4.17}$$

$$T_P(\mathbf{k} \leftarrow \mathbf{k}_1) = 2\mathrm{Re}\left[(k_x k_{1y} - k_{1x} k_y)n^*_{\mathbf{k}} \phi_{\mathbf{k}_2} n_{\mathbf{k}_1}\right] \ , \tag{4.18}$$

and

$$T_W(\mathbf{k} \leftarrow \mathbf{k}_1) = 2\mathrm{Re}\left[(k_x k_{1y} - k_{1x} k_y)\omega^*_{\mathbf{k}} \phi_{\mathbf{k}_2} \omega_{\mathbf{k}_1}\right] \ , \tag{4.19}$$

where ω is the vorticity. These quantities are four-dimensional $T(k_x, k_y, k_{1x}, k_{1y})$ and therefore averaging must be performed in order to plot the data.

Curvature-Hasegawa-Wakatani

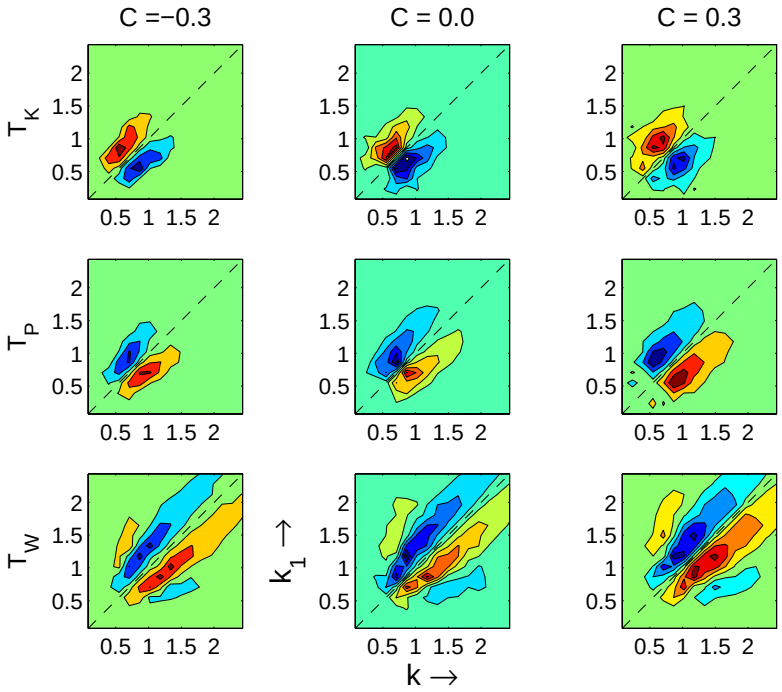

Figure 4.8: Nonlinear transfer functions for different values of C.

In figure 4.8 we plot T_K, T_P and T_W for three different values of C, using the same CHW datasets as in the previous section. The data is averaged over components k_x, k_y and k_{1x}, k_{1y}. Negative values (blue) indicate that energy is transferred from

mode k to mode k_1, while positive (red) values indicate that energy is transferred from mode k_1 to mode k. In the case of T_K we find that the dominant transfer of kinetic energy is from larger to smaller values of k, in an inverse cascade. In the case of T_P and T_W we find that the dominant transfer of potential energy and enstrophy is from smaller values of k to larger values of k, in a direct cascade process. Thus there is a dual cascade process operating in the CHW model. The same result was found for the HW model in [Manz et al., 2009a]. As C is increased, the range of coupled wavenumbers becomes wider.

Zonal-Hasegawa-Wakatani

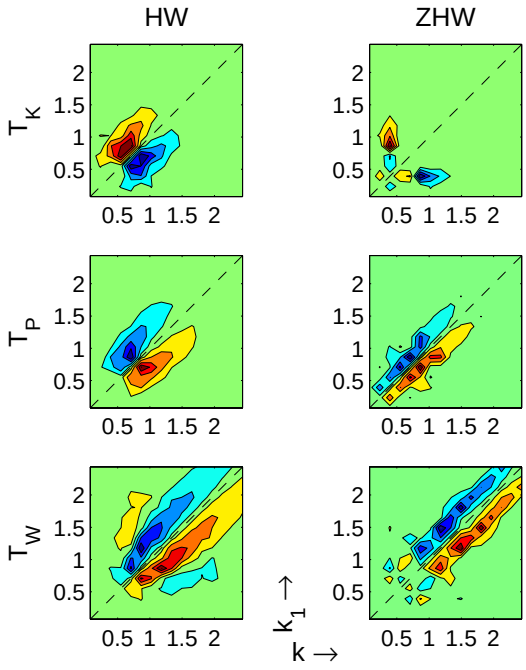

Figure 4.9: Nonlinear transfer functions for the HW and ZHW models.

We perform the same analysis on ZHW model data, using the same numerical parameters. Figure 4.9 shows a comparison of the transfer functions T_K, T_P and T_W calculated for the HW model (which is equivalent to CHW with $C = 0$) and ZHW model. Interestingly, the form of each transfer function is changed by the presence of the zonal flow. The range of coupled wavenumbers is much narrower in the ZHW than

the HW case.

Although the previous analysis provides interesting results, the role of the zonal flow is not clear since every wavenumber is treated equally. Theoretically, the energy of the zonal flow ($k_y = 0$) should come from the drift-wave turbulent fluctuations ($k_y \neq 0$) [Diamond et al., 2005] and we would like to illustrate this process using the transfer functions. Following the representation used in [Manz et al., 2009b] we plot T_K, T_P and T_W as functions of k_{1y} and k_{2y} in figure 4.10 for the HW and ZHW models. The transfer functions are thus averaged over k_{1x} and $k_{2x} \neq 0$. The contribution corresponding to the zonal flow is $k_y = 0$ which appears on the figure at $k_{1y} = -k_{2y}$ and is indicated by dashed lines. We find that, in the ZHW case, a large proportion of the drift-wave energy ($k_{1y} \neq 0$) is transferred into zonal flows. In the HW case, the zonal flow contribution is small and is not apparent in the figure. This is in agreement with theory and experiment [Diamond et al., 2005; Manz et al., 2009b].

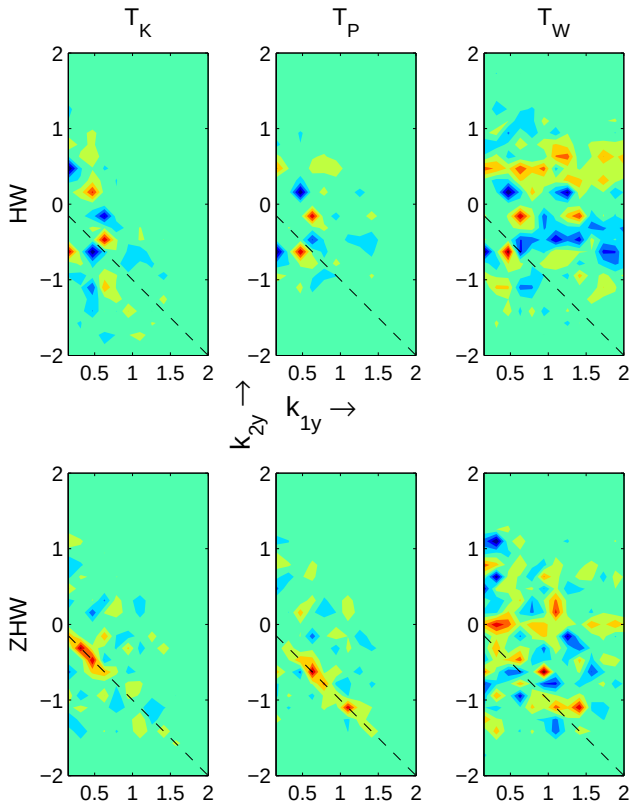

Figure 4.10: Nonlinear transfer functions for the HW and ZHW models. The dashed lines indicate the zonal flow contribution ($k_y = 0$).

Chapter 5

Test particle transport

This chapter is concerned with the study of passive test particles in order to understand the transport properties of plasma turbulence. Parts of the chapter were originally published as *The effects of nonuniform magnetic field strength on density flux and test particle transport in drift wave turbulence*, J.M. Dewhurst, B. Hnat and R.O. Dendy, Phys. Plasmas **16**, 072306 (2009) and *Finite Larmor radius effects on test particle transport in drift wave-zonal flow turbulence*, J.M. Dewhurst, B. Hnat and R.O. Dendy, Plasma Phys. Control. Fusion **52**, 025004 (2010).

5.1 Introduction

Understanding the transport of particles and energy in turbulent plasma is fundamentally important to the goal of magnetically confined nuclear fusion. This is particularly true in the edge region of a tokamak, where turbulent transport responds to, and also determines, the radial density and temperature profiles. Edge turbulence, together with magnetohydrodynamic instabilities, also determines the flux of particles and energy across the last closed magnetic flux surface, and hence to the divertor or the first wall.

The majority of cross-field particle and energy transport can be attributed to low frequency turbulent fluctuations. The drift instability provides a mechanism for

the generation of such fluctuations in the presence of a background density gradient perpendicular to the magnetic field. The edge region of magnetically confined plasmas, with increased collisionality and large density gradients, offers ideal conditions for the drift instability to occur.

Perspective on the turbulence can be obtained through the study of passive tracer particles, see [Manfredi and Dendy, 1996, 1997; Annibaldi et al., 2000, 2002; Gustafson et al., 2008; Pedersen et al., 1996; Naulin et al., 1999; Basu et al., 2003a,b; Futatani et al., 2008; Naulin et al., 2008, 2006; Angioni and Peeters, 2008] for example. In this chapter, we study the transport of passive tracer particles in the Hasegawa-Wakatani (HW) model using output of the HAWK code. We are interested in the effects on the transport of modifying the HW equations to include extra physical effects. Using the Hasegawa-Mima (HM) equation as the turbulence model, the transport of passive test particles was studied in [Manfredi and Dendy, 1996, 1997; Annibaldi et al., 2000, 2002; Gustafson et al., 2008]. Test particle transport in the HW model was studied in [Pedersen et al., 1996; Naulin et al., 1999; Basu et al., 2003a,b; Futatani et al., 2008], and a recent overview can be found in [Naulin et al., 2008].

5.2 Test particle evolution

As discussed in the derivation of the Hasegawa-Wakatani equations in Section 3.2, the equation of motion for ions is $\mathbf{v}_\perp = \mathbf{v}_\mathbf{E} + \mathbf{v}_p$, where $\mathbf{v}_\mathbf{E}$ is the $E \times B$ velocity, $\mathbf{v}_p$ is the polarization velocity and the subscript $\perp$ indicates motion perpendicular to the confining magnetic field $\mathbf{B}$. This equation results from the assumption that the ions are cold, $T_i = 0$. If in addition, the mass of the test particle ions is negligible, the equation of motion reduces to

$$\frac{\partial \mathbf{r}}{\partial t} = \mathbf{v}_\mathbf{E} \ , \tag{5.1}$$

and in the normalised units of the HW model $\mathbf{v}_\mathbf{E}$ can be written

$$\mathbf{v}_\mathbf{E} = \left(-\frac{\partial \phi}{\partial y}, \frac{\partial \phi}{\partial x} \right) \ . \tag{5.2}$$

This simplified equation of motion, involving only the electrostatic potential ϕ, is used for the evolution of test particles in this chapter. In using this equation, we are also making the assumption that the test particles are passive, in that they react to but do not generate electrostatic fields.

Time integration of equation 5.2 is performed using the third order Karniadakis scheme [Karniadakis et al., 1991]. The potential ϕ is taken from output of the HAWK code. An interpolation scheme must be employed to calculate ϕ since test particles will not always be exactly on grid points. Here, we employ bilinear interpolation.

We solve the HW equations (or variations there of) on a square of length $L = 40$ using 256×256 grid nodes with periodic boundary conditions. We consider a base case with parameters $\kappa = 1$, $\alpha = 0.5$ and $C = 0$, a time step of $\Delta t = 0.01$ and Newtonian viscosity with $D = 0.01$. The effects of altering the various parameters are then determined by varying one parameter and comparing with this base case.

Runs of the HAWK code are initialised with low-amplitude random noise. Linear drift waves are excited and grow exponentially until nonlinear effects become important. Eventually, a quasi-stationary turbulent state is reached. Ten thousand particles are initialised at random positions throughout the computational domain once a quasi-stationary turbulent state has been reached by HAWK, i.e. once the energy E and enstrophy W saturate. The positions of these test particles then change according to the equation of motion above, as the turbulence evolves.

We note from equation 5.2 that contours of equipotential ϕ are stream lines of $\mathbf{v_E}$. Therefore, on time scales shorter than their life time, coherent turbulent structures are impervious to test particles. Conversely, test particles can be trapped by structures and the dynamics of the structures will affect the dispersion of the test particles.

In order to quantify the diffusion of the test particles, we record the trajectory of each particle and calculate a running diffusion coefficient in the radial x and poloidal y directions separately,

$$D_x(t) = \frac{X(t)^2}{2t} \ , \ D_y(t) = \frac{Y(t)^2}{2t} \ . \tag{5.3}$$

Here $X(t)^2 = \langle [x(t) - \langle x(t) \rangle]^2 \rangle$, $Y(t)^2 = \langle [y(t) - \langle y(t) \rangle]^2 \rangle$ and $(x(t), y(t))$ is the position of the particle with respect to its initial position; angular brackets denote an ensemble average over the $10,000$ test particles. For an ordinary diffusive process the running diffusion coefficient will reach a value independent of time since $X(t)^2 \sim t$. More generally the transport may be 'anomalous' and $X(t)^2 \sim t^\sigma$, where $0 < \sigma < 1$ implies subdiffusion, $1 < \sigma < 2$ implies superdiffusion and $\sigma = 2$ is ballistic.

In [Naulin et al., 1999] it was shown that passive test particle transport in the HW model is essentially a normal diffusive process due to trapping and detrapping of the test particles by the turbulent structures. It was also shown that poloidal diffusion is stronger than radial, $D_y > D_x$. In [Basu et al., 2003a] increasing the coupling parameter α was shown to decrease the rate of radial test particle transport. The effect of finite ion inertia and the polarization drift $\mathbf{v}_p$ was studied in [Basu et al., 2003b], and the intermittent nature of test particle transport in the HW model was studied in [Futatani et al., 2008]. Here, we focus on the effects of the magnetic field inhomogeneity incorporated in the CHW model and the zonal flows incorporated in the ZHW model.

5.3 Non-uniform magnetic field strength

5.3.1 Introduction

Drift wave phenomenology is purely electrostatic, and generally the magnetic field is assumed to be uniform. In tokamaks, however, the toroidal magnetic field strength is non-uniform and declines with radial distance from the axis of symmetry. The inclusion of this magnetic field gradient leads to a non-vanishing divergence of diamagnetic velocity, associated with compressible effects, and the appearance of the interchange instability. In toroidal geometry, interchange modes have destabilising effects in the region where the vectors ∇B and the radius of curvature are parallel to the pressure gradient (low field side) and have stabilising effects on the high field side. This alters the properties of the turbulence, allowing the excitation of interchange-type ballooning modes. Plasma

particles, following helical magnetic field lines, experience both interchange-stable and interchange-unstable regions and their behaviour is averaged over these different regimes of turbulence.

In this section we investigate the effects of non-uniform background magnetic field strength on the turbulence and the transport of passive test particles, using direct numerical simulation of a 2D turbulent system. Our model of drift wave turbulence is an extended form of the HW equations [Hasegawa and Wakatani, 1983] that includes magnetic field inhomogeneity in the radial direction and the resulting interchange driven modes [Chen et al., 1980]. The model, which we refer to this as the curvature-Hasegawa-Wakatani (CHW) model, was introduced in Section 3.7. The model was studied in 3D by Sugama, Wakatani and Hasegawa [Sugama et al., 1988] and in 2D in [Scott, 2005] and [Vergote et al., 2006] for example; see also [Horton, 1999].

We are interested in the effect of changing the magnetic field inhomogeneity (i.e. changing the value of the parameter C in equations 3.19 and 3.20) on the transport of test particles. We therefore set $\alpha = 0.5$, $\kappa = 1$ and $D = 0.01$ with Newtonian viscosity throughout and vary the parameter $C = -\partial \ln B/\partial x$ which characterises the gradient of $B(x)$. Typical snapshots of the potential ϕ in the quasi-stationary saturated turbulent state for $C = [-0.3, 0, 0.3]$ are shown in figure 3.9 in Section 3.7. In each case, the turbulence is dominated by vortex structures. Contours represent $E \times B$ velocity stream lines which test particles follow exactly.

5.3.2 Running diffusion coefficients

A set of simulations of the CHW model are run with the parameter C being varied. In figure 5.1 we plot the calculated running diffusion coefficients D_x and D_y as functions of time for $C = [-0.3, 0.0, 0.3]$. In all cases, after a short initial ballistic phase, the running diffusion coefficient asymptotically tends to a value independent of time, indicating diffusive processes. Increasing the parameter C tends to increase the radial diffusion coefficient D_x and decrease the poloidal one D_y. For $C = 0$ and $C = -0.3$ we find that

the poloidal diffusion is stronger than the radial, in agreement with [Naulin et al., 1999]; however, for $C = 0.3$ this anisotropy is reversed and the radial diffusion dominates.

In figure 5.2 we plot $X^2/t^{0.45}$ and $Y^2/t^{1.7}$ versus time for $C = -0.5$. We find that, after an initial phase, these quantities become time independent, indicating that the radial test particle transport is subdiffusive with exponent $\sigma \approx 0.45$ and the poloidal transport is superdiffusive with $\sigma \approx 1.7$. Interestingly, poloidal superdiffusion with $\sigma = 1.7$ was found for test particle transport in quasistationary HM turbulence; see figure 2(b) of [Annibaldi et al., 2000].

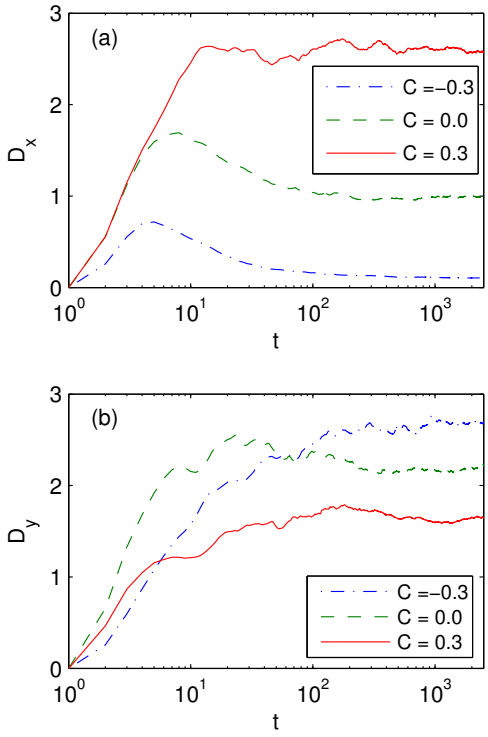

Figure 5.1: Plots of running diffusion coefficient (a) D_x, and (b) D_y versus time for different values of C.

5.3.3 Fick's law

Figure 5.3(a) displays the time-independent values of D_x and D_y for a wider range of C (for cases where the transport is diffusive). We find that D_x increases and D_y

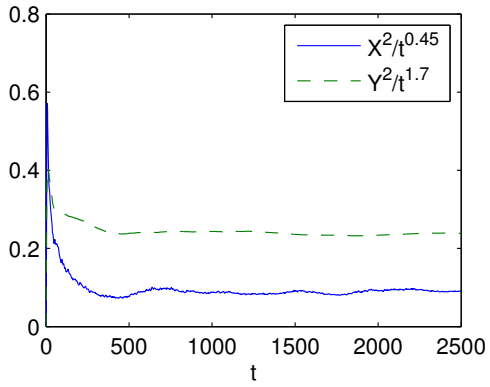

Figure 5.2: Plots of $X^2/t^{0.45}$ and $Y^2/t^{1.7}$ versus time for $C = -0.5$ showing subdiffusion in x and superdiffusion in y.

decreases with C. We also plot the total radial density flux Γ_{n0} (defined in equation 3.45) averaged over the computational box in figure 5.3(b).

Extending the arguments in [Basu et al., 2003a], Γ_{n0} and D_x can be linked through conservation of potential vorticity $\Pi = (\nabla^2\phi - n + (\kappa - C)x)$. It follows from equation 3.72 that $\langle (dx/d\zeta)^2 \rangle = (\kappa - C)^{-2}$, from equation 5.3 that $d\langle x^2 \rangle = 2D_x dt$, and from equation 3.42 and 3.70 and the definition of $\zeta = \nabla^2\phi - n$ that $d\langle \zeta^2 \rangle = 2(\kappa - C)\Gamma_{n0}dt$. Combining these three expressions, we infer

$$\Gamma_{n0} = (\kappa - C)D_x \ , \tag{5.4}$$

which is in the form of Fick's law. Since the steady-state value of D_x is found to scale approximately linearly with with C, for the values considered in figure 5.3(a) we infer empirically that equation 5.4 is approximately quadratic in C, leading to the maximum in Γ_{n0} seen in figure 5.3(b). In figure 5.3(b) we also plot $(\kappa - C)D_x$ which closely matches Γ_{n0}. Thus we may use equation 5.4 to link the radial diffusive transport of test particles to the underlying turbulence. This relation is valid only in the inviscid limit ($D = 0$) since the conservation of potential vorticity Π only applies in this limit. Therefore, some departure for larger values of dissipation D is expected. We have verified this with our code and, for the case of $C = 0$, we obtain results similar to those presented in [Basu et al., 2003a]. For $C = \pm 0.3$ the agreement is similar or better for same range of

examined dissipation coefficients.

Interestingly, the expression includes the factor $\kappa - C$, which we have shown in Section 3.7 is related to poloidal flow velocity. Thus the radial diffusion of test particles D_x is linked to the radial turbulent flux Γ_{n0} and poloidal flow. The effect of a homogeneous poloidal flow on test particle transport was discussed in [Hauff and Jenko, 2007].

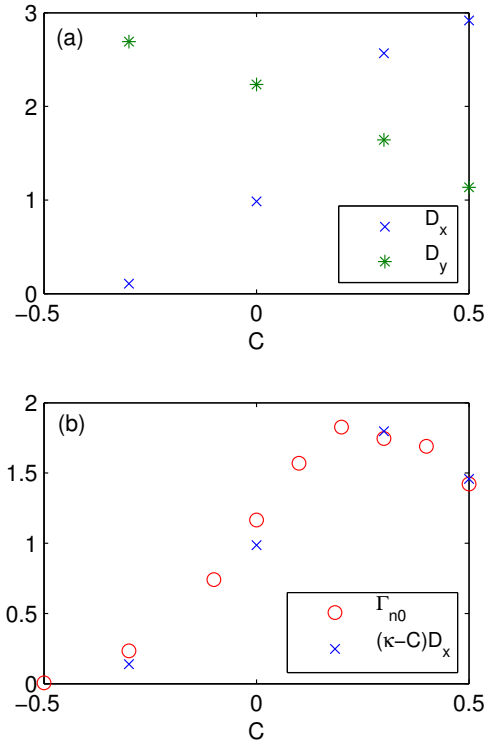

Figure 5.3: (a) Time independent diffusion coefficients D_x and D_y for different values of C. (b) Average radial density flux Γ_{n0} and $(\kappa - C)D_x$ for different values of C.

If correlations between ζ and its initial value ζ_0 do not vanish, it follows that $d\langle\zeta^2\rangle$ and hence the diffusion coefficient can be functions of time, leading to non-diffusive transport. In figure 5.4 we show how the normalized correlation $\langle\zeta_0\zeta\rangle/\sqrt{\langle\zeta_0^2\rangle\langle\zeta^2\rangle}$ evolves with time in the saturated turbulent state for $C = [-0.5, -0.3, 0]$. In all cases, there is an initial phase where correlations decay, corresponding to the initial ballistic phase of the test particle transport. After this phase, for the $C = -0.3$ and $C = 0$ cases,

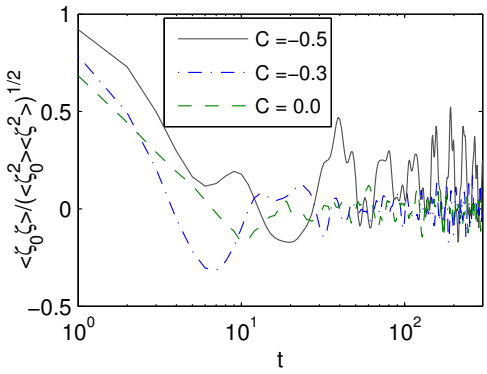

Figure 5.4: Normalised correlation between fluid potential vorticity ζ_0 at $t = 0$, and fluid potential vorticity ζ at time t, for different values of C.

the correlation fluctuates around zero and the test particle transport is diffusive. For the $C = -0.5$ case, however, correlations persist for long times and the test particle transport is non-diffusive.

5.3.4 Summary

We have studied an extended form of the Hasegawa-Wakatani model that includes the effects of a magnetic field inhomogeneity in the radial direction $B(x)$. With the parameter controlling the background density gradient set to $\kappa = 1$ throughout, we have established that the parameter C, controlling the radial gradient of the magnetic field $B(x)$, alters the dispersion of test particles. Measurements of diffusion coefficients show that the rate of radial transport of test particles increases and the rate of poloidal transport decreases monotonically with C. For large negative values of C, correlations in the flow persist for long times and the radial transport becomes subdiffusive while the poloidal transport becomes superdiffusive. The rate of radial diffusive test particle transport and the average $E \times B$ density flux can be linked by a simple expression, in the form of Fick's law.

5.4 Zonal flow and finite Larmor radius

5.4.1 Introduction

In this section we study particle transport in magnetically confined fusion plasma using a modified HW model which produces drift wave turbulence that self-organises into zonal flows. We study the transport of passive test particles which are advected by the $E \times B$ velocity. Our flexible model allows us to compare the case where zonal flows are absent to the case where zonal flows are self-generated and also to an intermediate state where the kinetic energy is shared equally between the zonal flows and drift wave turbulence. We also consider the effects of finite Larmor radius.

The presence of zonal flows can modify drift wave turbulence transport via two mechanisms. First, simple energy balance suggests that the level of turbulence must decrease since the energy of the zonal flows is acquired directly from the turbulence through nonlinear interactions. Second, zonal flows naturally evolve into long-lived coherent structures that support stationary shear layers [Smolyakov et al., 2000]. Spatially intermittent regions of high velocity shear exhibit decreased levels of transport since the shear distorts and destroys turbulent eddies. We recall here that, in a simple random walk approximation for the particle diffusion coefficient across the magnetic field, the eddy size represents the smallest step of the transport process. Thus zonal flows may be one of the important ingredients in the development of transport barriers which are observed during the transition from low to high confinement mode plasma states.

The response of particles to turbulent fields can greatly differ depending on the Larmor radius. High frequency gyromotion effectively smooths out small fluctuations leading, intuitively, to a lower rate of transport. A reduction in radial transport with increasing Larmor radius was shown in [Manfredi and Dendy, 1996, 1997; Annibaldi et al., 2000, 2002] using the Hasegawa-Mima (HM) equation [Hasegawa and Mima, 1978] as the turbulence model. More recently it was found that, in the limit of large Kubo number, $K > 1$, this reduction in transport is less dramatic and in some cases, the

rate of transport may actually increase with the Larmor radius [Vlad and Spineanu, 2005; Vlad et al., 2005; Hauff and Jenko, 2006, 2007]. The Kubo number, $K = \langle v^2 \rangle^{1/2} \tau_c / \lambda$, is a measure of the average distance covered by a test particle $\langle v^2 \rangle^{1/2} \tau_c$, in one correlation time τ_c, relative to the typical spatial scale of the turbulent fluctuations λ. In [Hauff and Jenko, 2007] it was reported that the zonal flow may have a strong influence on the rate of transport and on the Larmor radius dependence.

We compare the diffusion of test particles using three related turbulence models: the standard Hasegawa-Wakatani (HW) model (3.19 and 3.20), the zonal-Hasegawa-Wakatani (ZHW) model (3.49 and 3.50) and the damped-zonal-Hasegawa-Wakatani (DZHW) model which were introduced in Chapter 3. The parameters are set to $\kappa = 1$, $\alpha = 0.5$ and the viscosity is Newtonian with $D = 0.01$ for every case considered.

5.4.2 Properties of the turbulence

Saturated turbulent state

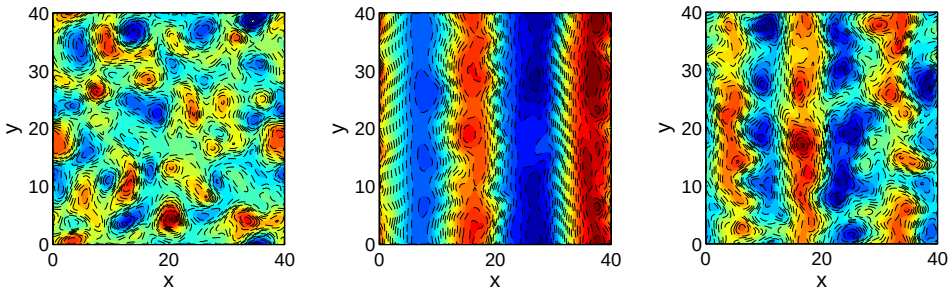

Figure 5.5: Snapshot of potential ϕ in the saturated quasi-stationary turbulent state for three related models: (left) HW defined by equations 3.19 and 3.20 where zonal flows are damped; (centre) ZHW defined by equations 3.49 and 3.20 allowing the self-generation of zonal flows; (right) intermediate state DZHW where total kinetic energy of zonal flows is set equal to that of non-zonal drift wave turbulence at each time step.

In figure 5.5 we show typical snapshots of the potential ϕ in the quasi-stationary saturated turbulent state for the three cases considered. For the HW model, turbulent vortices dominate. For the ZHW model, zonal flows dominate; while the zonal flows

visible in figure 5.5 persist throughout the simulation time, inspection of the power spectrum reveals the presence of higher frequency broadband turbulence, because the drift wave turbulence has been suppressed but not eliminated. The intermediate DZHW state is generated by artificially setting the kinetic energy of the zonal flows equal to the kinetic energy of the non-zonal drift wave turbulence at each time step in the saturated turbulent state of the ZHW model. We find that zonal flows and turbulent vortices then coexist in a quasi-stationary state; the zonal flows in figure 5.5 persist throughout the simulation time.

Weiss field

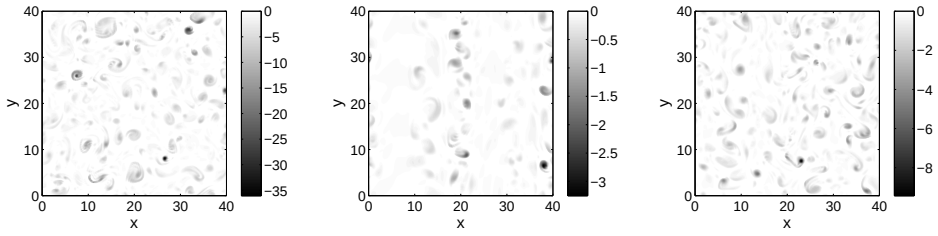

Figure 5.6: Weiss field, Q, calculated from data in figure 5.5: (left) HW; (centre) ZHW; (right) intermediate DZHW state. Only negative values of Q are shown.

Before the effects of finite Larmor radius on particle transport are considered in the next section, it is useful to provide a quantitative measure of the interaction between test particles and the coherent structures of the turbulent flow. For this purpose we employ the Weiss field, Q, [Weiss, 1991] which is a local measure of stress s compared to vorticity ω. In the 2D velocity field provided by our model, Q is defined as:

$$Q = \frac{1}{4}(s^2 - \omega^2) \ , \tag{5.5}$$

where the stress s is given by

$$s^2 = \left(\frac{\partial v_x}{\partial x} - \frac{\partial v_y}{\partial y}\right)^2 + \left(\frac{\partial v_y}{\partial x} + \frac{\partial v_x}{\partial y}\right)^2 \ , \tag{5.6}$$

and the vorticity is $\omega = \nabla^2\phi$. The $E \times B$ velocity field is given by equation 5.2. Thus

Q may be expressed as

$$Q = \left(\frac{\partial^2 \phi}{\partial x \partial y} \right)^2 - \frac{\partial^2 \phi}{\partial x^2} \frac{\partial^2 \phi}{\partial y^2} \ , \tag{5.7}$$

which is equivalent to the second derivative test discriminant in calculus. Weiss showed [Weiss, 1991] that if the strain rate varies slowly with respect to the vorticity gradient, the sign of Q determines whether two initially close fluid elements will separate ($Q > 0$) or not ($Q < 0$), following the frozen streamlines. From the calculus point of view, $Q > 0$ implies a local saddlepoint in ϕ while $Q < 0$ implies a maximum or minimum. Evaluating Q at the position of a test particle has been used to determine whether or not the particle is trapped in a nonlinear structure ($Q < 0$) or not ($Q > 0$) [Annibaldi et al., 2002; Naulin et al., 1999]. In figure 5.6 we show the negative Weiss field, $Q < 0$, calculated from the data in figure 5.5. Vortical structures are clearly distinguished by large negative values of Q. The probability density function (PDF) of Q, $P(Q)$, was shown in [Bos et al.,

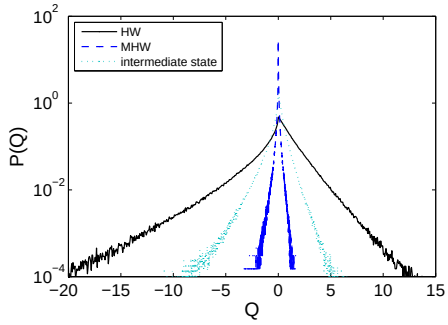

Figure 5.7: PDF of Weiss field, $P(Q)$, for the three turbulence regimes of figure 5.5.

2008] to distinguish between different regimes of turbulence. Here, we calculate Q at all grid points using multiple snapshots of the potential in time; $P(Q)$ is then calculated by binning the resulting data. Figure 5.7 shows $P(Q)$ on a semi-logarithmic scale for the three cases considered in figure 5.5, which $P(Q)$ clearly distinguishes. The negative tail, $Q < 0$, of the PDF falls off slowest for the HW case, fastest for the ZHW case and is intermediate in the intermediate DZHW case. Therefore, we may expect trapping effects to be strongest in the HW case which has no zonal flows, weakest in the ZHW case which has strong zonal flows, and intermediate in the intermediate DZHW case.

5.4.3 Test particle transport

We now turn to test particle transport and finite Larmor radius (FLR) effects. The form of the $E \times B$ velocity field, equation 5.2, gives an indication of the FLR effects one would expect from our model. From equation 5.2 we conclude that contours of equipotential ϕ are stream lines of $\mathbf{v}_E$. Therefore, on time scales shorter than their life time, the turbulent structures – implying closed contours of ϕ – are impervious to test particles with zero Larmor radius. Conversely, test particles can be trapped by the structures, and the dynamics of the structures will affect the dispersion of the test particles. When the Larmor radius is finite, test particles are able to permeate turbulent structures, so that the effect of the structures on the transport is lessened.

For each value of Larmor radius ρ, a population of 10 000 test particles is initialised at random positions throughout the domain once the quasi-stationary turbulent state has been reached. The Larmor radius ρ is measured in the dimensionless units of the model, i.e. normalised to ρ_s. Provided that the frequency of the gyro-motion is much faster than the frequency of the turbulence, FLR effects can be included [Manfredi and Dendy, 1996] simply by spreading the particle over a ring of (Larmor) radius ρ centred on the particle's guiding centre. This is implemented numerically by averaging over N_{gyro} ($= 16$ in this case) points. Each test particle has the equation of motion $\partial \mathbf{r}/\partial t = \hat{\mathbf{v}}_E$, where $\hat{\mathbf{v}}_E$ is the gyro-averaged $E \times B$ velocity given by equation 5.2.

5.4.4 Test particle displacements

In figure 5.8 we plot the PDFs of the displacements Δx and Δy of test particles in the x and y directions for the three turbulence regimes represented by the three cases specified in figure 5.5. The PDFs $P(\Delta x)$ and $P(\Delta y)$ are plotted normalised to the standard deviation σ and are calculated using the jumps made by the particles over one normalised time unit for the case where $\rho = 0$ for all test particles. We quantify departures of the distributions from Gaussian with skewness $S = \langle \Delta^3 \rangle / \langle \Delta^2 \rangle^{3/2}$, measuring asymmetry, and kurtosis $K = \langle \Delta^4 \rangle / \langle \Delta^2 \rangle^2$, measuring peakedness; a Gaussian PDF has $S = 0$ and

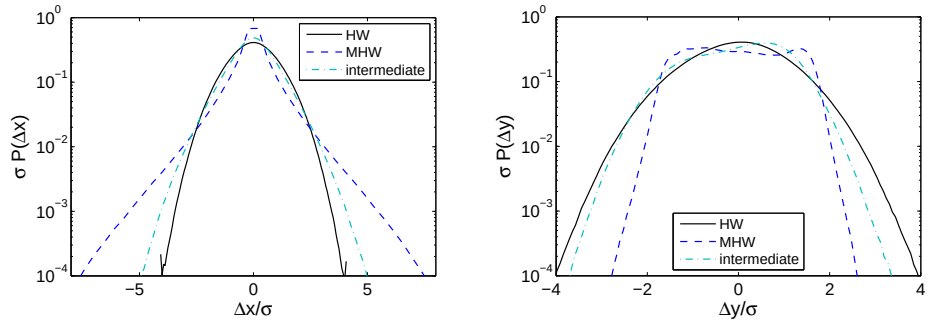

Figure 5.8: PDFs of jumps Δx (left) and Δy (right) made by particles for $\rho = 0$ in the HW, ZHW and intermediate DZHW cases.

$K = 3$. In the HW case we find $S = -0.01$ and $K = 3.00$ in the x direction, and $S = -0.06$ and $K = 2.98$ in the y direction; i.e. the PDFs are close to Gaussian. For the ZHW case the PDFs are radically different and very far from Gaussian with $S = 0.00$ and $K = 8.06$ in the x direction, and $S = 0.01$ and $K = 1.87$ in the y direction. The PDFs for the intermediate DZHW state are indeed intermediate between the HW and ZHW cases with $S = 0.00$ and $K = 4.01$ in the x direction, and $S = -0.03$ and $K = 2.47$ in the y direction. Similar PDFs are found when $\rho \neq 0$.

5.4.5 Test particle diffusion

The Gaussian distribution of particle steps identified for the HW turbulence allows the assumption of diffusive transport in this regime. The significant departure of the PDFs from the normal distribution for the ZHW and DZHW cases raises intriguing questions about the nature of transport for these regimes. In this section, the nature of the test particle transport is established by examining running diffusion coefficients in the radial D_x and poloidal D_y directions. Our goal is to establish whether a diffusive transport model can be used for the test particles in the ZHW and intermediate regimes, and also to determine if the nature of the transport is modified by FLR effects.

In figure 5.9 (a) and (b) we plot the running diffusion coefficients $X^2/2t$ and $Y^2/2t$ versus time for the HW case for $\rho = [0, 1, 2]$. We find that these quantities

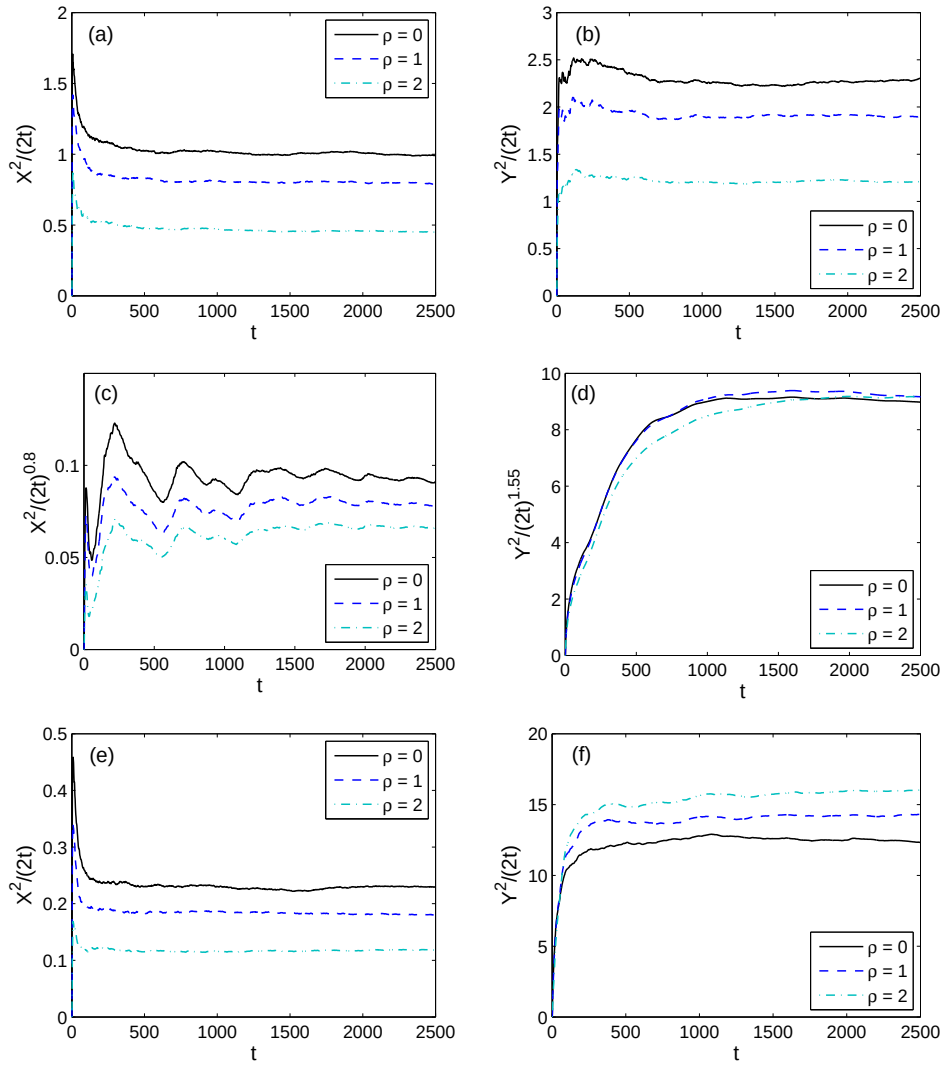

Figure 5.9: Test particle diffusion: (a) and (b) $X^2/2t$ and $Y^2/2t$ versus time for HW case showing normal diffusion; (c) and (d) $X^2/(2t)^{0.8}$ and $Y^2/(2t)^{1.55}$ versus time for ZHW case demonstrating subdiffusion in x and superdiffusion in y; (e) and (f) $X^2/2t$ and $Y^2/2t$ versus time for intermediate DZHW turbulence case showing normal diffusion.

converge on time independent values, indicating normal diffusive processes in both the x and y directions and for all values of ρ. We note that the rate of transport is larger in the poloidal y direction than the radial x direction by a factor of about two. These results agree with [Naulin et al., 1999], where it was shown that passive test particle transport in the HW model is essentially a normal diffusive process arising from trapping and detrapping of the test particles by the turbulent vortices.

Figures 5.9 (c) and (d) show $X^2/(2t)^{0.8}$ and $Y^2/(2t)^{1.55}$ versus time for the ZHW case. We find that these quantities become time independent, indicating that for all values of ρ, radial diffusion (across the zones) is subdiffusive with exponent $\sigma \approx 0.8$ while poloidal diffusion (along the zones) is superdiffusive with exponent $\sigma \approx 1.55$. Unlike the other two cases presented here, the measured exponents for the ZHW case change slightly with different seeding of the turbulence code. We obtain exponents in the range $\sigma \approx 0.8 - 0.9$ in the radial direction and $\sigma \approx 1.5 - 1.8$ in the poloidal direction. We note that zonal flows drastically reduce radial transport and increase poloidal transport compared to the HW case. In the presence of zonal flows, poloidal superdiffusion was found in [Annibaldi et al., 2002] and [Gustafson et al., 2008] using the HM model and radial subdiffusion was found in gyrokinetic ITG turbulence in [Sanchez et al., 2009].

Figures 5.9 (e) and (f) show $X^2/2t$ and $Y^2/2t$ versus time for the DZHW turbulence case. In contrast to the ZHW case, we find that the running diffusion coefficients converge on time independent values, indicating normal diffusive processes for all ρ. We note that the rate of transport is larger in the poloidal y direction than the radial x direction by about an order of magnitude. Compared to the HW case, the poloidal diffusion is about five times larger, while the radial diffusion is about five times smaller.

5.4.6 Larmor radius dependence

In the previous section, we determined the nature of the test particle diffusion and established that this does not change with the Larmor radius, i.e. the exponent σ is independent of ρ. In this section, we determine how the magnitude of the diffusion changes with the Larmor radius ρ. In figure 5.10 we plot the values of the diffusion coefficients D_x and D_y at the end of the simulation ($t = 2500$ normalised time units) as a function of ρ for all the cases considered in order to show the trends. The results taken from the previous section, where all the test particles share the same Larmor radius ρ, are indicated by crosses. Circles indicate the results when the Larmor radii ρ' are distributed around a most probable value ρ according to a discrete approximation to the Boltzmann distribution,

$$f(\rho') = (4\pi^{-1/2}\rho^{-3})\rho'^2 \exp\left(-\rho'^2/\rho^2\right) . \tag{5.8}$$

We note that the results for the ZHW case do not represent true diffusion coefficients since D_x and D_y change with time and the figures are plotted for comparison purposes.

Figures 5.10 (a) and (b) show the results for the HW case. For all cases, the diffusion coefficients decrease as ρ increases. A transition between regions of faster and slower decline occurs around $\rho = 3$ which equates to the typical radius of the turbulent vortices seen in snapshots of the potential (figure 5.5).

Figures 5.10 (c) and (d) show the results for the ZHW case. The Larmor radius dependence of the poloidal diffusion coefficient D_y is radically different from the HW case. For small values of ρ, D_y is constant and even increases slightly with ρ. For larger ρ, the rate at which D_x and D_y decline with increasing ρ is smaller than in the HW case. For large values of ρ, the Larmor radius dependence of D_y significantly differs between the case where all test particles share the same ρ and the case where the Larmor radii follow a Boltzmann distribution. In the former case, D_y falls off almost to zero at $\rho = 8$ which corresponds to the radial half-wavelength of the zonal flow, so that the effects of the zonal flow are maximally averaged out. Although the exponents σ change when

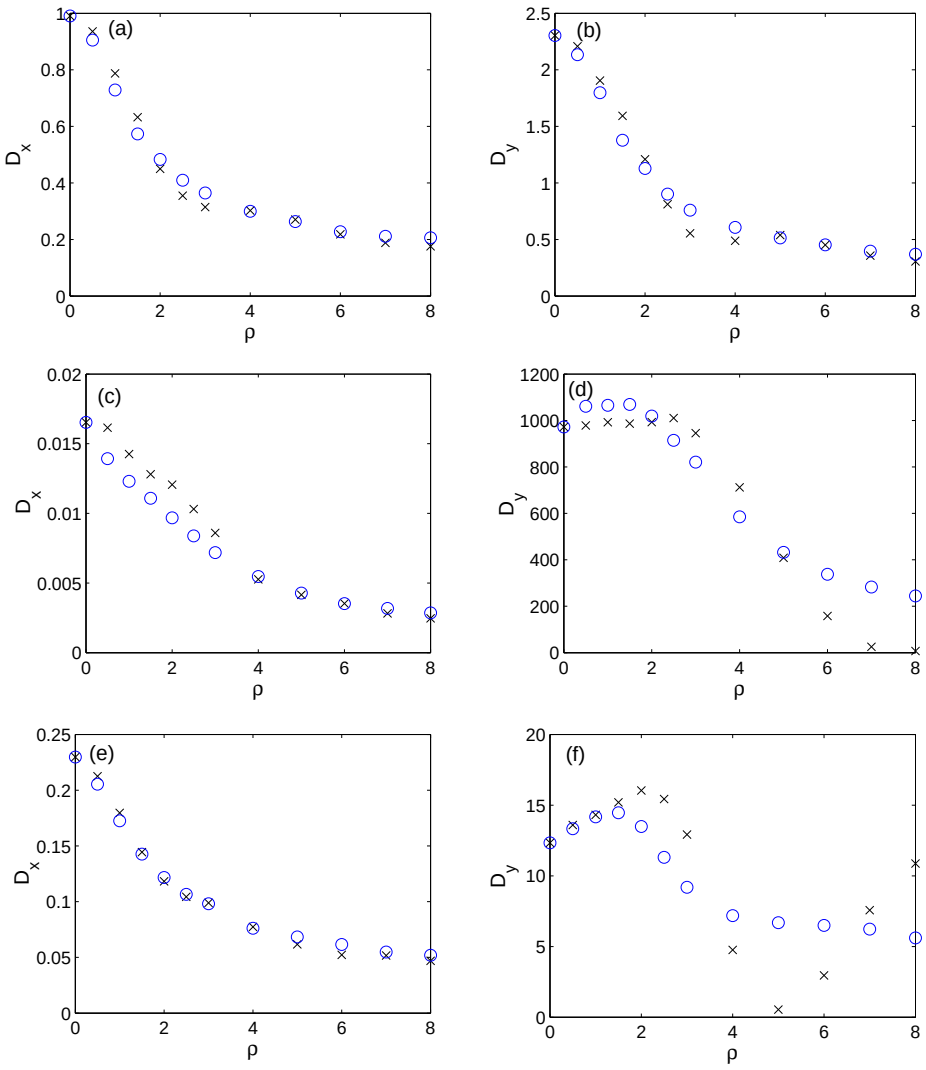

Figure 5.10: Value of diffusion coefficients D_x and D_y at the end of the simulation ($t = 2500$ normalised time units) as a function of ρ: (a) and (b) HW case; (c) and (d) ZHW case; (e) and (f) intermediate DZHW turbulence case. Crosses indicate results when all the test particle share the same Larmor radius ρ; circles indicate results when the Larmor radii are distributed around a most probable value ρ.

the seeding of the turbulence code is changed–as discussed in the previous section–the features of the Larmor radius dependence described here do not change.

Figures 5.10 (e) and (f) show the results for the DZHW case. We find that the Larmor radius dependence has similarities to the ZHW case. The radial diffusion coefficient D_x decreases with ρ. For small ρ, the poloidal diffusion coefficient D_y increases with ρ, and this effect is larger than in the ZHW case. For larger ρ, when all the test particles share the same Larmor radius, D_y decreases to a minimum around $\rho = 5$ and this corresponds to the radial half-wavelength of the zonal flow. The value of D_y at this minimum is very close to the corresponding value for the HW case. After the minimum, D_y increases with ρ. When the test particles have a Boltzmann distribution of Larmor radii, there is no such minimum, and D_y falls off slowly with large ρ.

5.4.7 Discussion

Several interesting effects for test particle transport in the presence of zonal flows have been identified. The introduction of strong zonal flows modifies the distribution of particle steps significantly. This is accompanied by a radical change in the nature of transport, which is no longer diffusive. While we are able to identify subdiffusive radial transport and superdiffusive poloidal transport, the convergence to these regimes is slow and the exact values of the scaling exponents σ appear not to be universal since their values depend on the initial conditions.

In the intermediate regime the PDFs also depart from Gaussian, but the transport process can still be described as diffusion. This may be due to the deviation from Gaussian being small, but may also reflect the fact that the strong spatial correlations due to the zonal flow do not dominate as in the ZHW case. While the diffusive behaviour is qualitatively similar to the HW case, the values of the diffusion coefficients are radically different with D_x decreasing and D_y increasing by an order of magnitude.

With zonal flows present, when all test particles share the same Larmor radius, D_y falls off with ρ to a minimum which corresponds to the half-wavelength of the zonal

flow. This minimum might be expected since test particles with ρ equal to the half-wavelength of the zonal flow will sample one full period of the zonal potential, leading to a low rate of poloidal transport since the sum over one period should be close to zero. As ρ becomes larger than the zonal flow half-wavelength, D_y begins to increase because the zonal potential is no longer averaged out. Minima in D_y should therefore be expected to occur periodically in ρ. No such minimum occurs when the test particles have a Boltzmann distribution, because a significant fraction of the test particles then have Larmor radii not equal to the zonal flow half-wavelength.

Intuitively, increasing the Larmor radius ρ should lead to a decrease in diffusion since increasingly large fluctuations are averaged out, as seen in HM simulations [Annibaldi et al., 2002]. In the HW case defined by equations 3.19 and 3.20, we observe this decrease. However, when zonal flows and turbulent vortices coexist (as in the ZHW and intermediate DZHW cases defined by equations 3.49 and 3.50) we find that the poloidal diffusion D_y increases with ρ for small ρ. This may be explained by the fact that increasing ρ also decreases the amount of trapping due to turbulent vortices. When ρ is small, test particles can be trapped in vortices and effectively shielded from the zonal flow. As ρ is increased the amount of trapping is reduced, so that the test particles are more exposed to the zonal flow potential, leading to an increase in D_y. This effect is stronger in the DZHW case than in the ZHW case, due to the presence of larger turbulent vortices. No increase in D_x is observed, because zonal flows do not produce radial diffusion.

The transport of test particles here may correspond with the transport of impurities in experiment. One would not expect a population of impurities to be monoenergetic and therefore the results using test particles with a Boltzmann distribution of Larmor radii may be closer to experiment. In a tokamak, impurities can affect confinement by radiating energy and causing collisions. Poloidal transport can lead to the dispersal of impurities throughout the plasma, whereas radial transport can lead to impurities leaving the plasma or reaching the core. The results here suggest that the radial transport of

impurities may be reduced by the presence of zonal flows and this may help to prevent impurities produced at the vessel wall reaching the core. On the other hand, impurities within the plasma may accumulate and degrade confinement. A zonal flow may quickly (superdiffusively) disperse impurities throughout the plasma. In ignited plasmas, alpha particles produced by fusion are an important impurity species. The results here suggest that such high energy particles will experience a low rate of turbulent diffusion, helping to heat the plasma.

5.4.8 Summary

We have investigated the effect of finite Larmor radius on the transport of passive test particles moving in turbulent electrostatic fields modelled by different variants of the Hasegawa-Wakatani equations. A wide variety of transport phenomena were observed due to an interplay between trapping in small scale vortices and entrainment in larger scale zonal flows. This flexible model allows the comparison of the case where zonal flows are damped, the case where zonal flows are self-generated and an intermediate state where the kinetic energy is shared equally between the zonal flows and drift wave turbulence.

We have established that, with zonal flows damped, the test particle transport is classically diffusive, with Gaussian statistics, and the rate of transport decreases with increasing Larmor radius. Once the Larmor radius is larger than the typical radius of the turbulent vortices, the rate of transport remains roughly constant.

When self-generating, poloidally extended zonal flows are allowed, non-Gaussian PDFs of test particle displacements are produced, the rate of radial transport is reduced, the rate of poloidal transport is increased and the Larmor radius dependence is altered. The rate of poloidal transport increases with small values of the Larmor radius and this may be attributed to a reduction in trapping effects due to the turbulent vortices, which shield particles from the zonal flows. When zonal flows are allowed to dominate, poloidal transport becomes superdiffusive and radial transport becomes subdiffusive.

Chapter 6

Summary and future work

The edge region of magnetically confined plasmas involves complicated physics acting over a wide range of spatial and temporal scales. This makes understanding this region very difficult and therefore it is beneficial to approach the problem from many different angles. In this thesis, edge plasma experimental data has been analysed and edge plasma modelling has been explored.

In Chapter 2 of this thesis, ion saturation current (I_{sat}) data taken from the Large Helical Device (LHD) and Mega-Amp Spherical Tokamak (MAST) was analysed. The absolute moment analysis revealed two regions of scaling, separated at a time scale of about $\tau_m = 40\mu$s, for all datasets studied. A monotonic relationship between connection length and skewness of the probability density function was found for LHD. Conditional averaging was used to characterise the average temporal shape of the largest intermittent bursts.

In Chapter 3, a new numerical code called HAWK was introduced. HAWK solves the Hasegawa-Wakatani (HW) equations which form a simple model of turbulence in the edge region of magnetic confinement devices. Modifications to the HW model, to include the effects of non-uniform magnetic field strength (curvature-Hasegawa-Wakatani [CHW] model) and zonal flows (zonal-Hasegawa-Wakatani [ZHW] model) were introduced and demonstrated.

In Chapter 4, output from the HAWK code was analysed. The probability density function of turbulent flux was computed and its variation with the parameters of the HW model was studied. Structure functions and higher order spectra were also investigated. Transfer functions demonstrated the presence of a turbulent dual cascade in the CHW model and the transfer of energy from drift-wave turbulence to zonal flows in the ZHW model.

In Chapter 5, the transport of passive test particles in the HW model and modifications was studied. For the CHW model, the conservation of potential vorticity $\Pi = \nabla^2\phi - n + (\kappa - C)x$ accounts for much of the phenomenology. Simple analytical arguments yielded a Fickian relation $\Gamma_n = (\kappa - C)D_x$ between the radial density flux Γ_n and the radial tracer diffusivity D_x, which was shown to explain key trends in the simulations. For the ZHW model, a subtle interplay between trapping in small scale vortices and entrainment in larger scale zonal flows determines the rate, character and Larmor radius dependence of the test particle transport. When zonal flows are damped, the transport is classically diffusive, with Gaussian statistics, and the rate of transport decreases with increasing Larmor radius. Once the Larmor radius is larger than the typical radius of the turbulent vortices, the rate of transport remains roughly constant. When zonal flows are allowed non-Gaussian statistics are observed. Radial transport (across the zones) is subdiffusive and decreases with the Larmor radius at a slower rate. Poloidal transport (along the zones), however, is superdiffusive and increases with small values of the Larmor radius.

6.1 Further work

In this thesis, many different avenues have been explored, some in more detail than others, and there are clearly many ways to take the work further.

6.1.1 Analysis of experimental data

The analysis presented in Chapter 2 would benefit from a systematic study using many additional datasets with different experimental conditions. This would allow more concrete statements on the question of universality.

Extra magnetic field coils, called resonant magnetic perturbation (RMP) coils have recently been installed in MAST. These coils, which are primarily used for ELM mitigation, modify the magnetic field structure near the edge of the plasma. Vacuum modelling shows that RMP coils effectively ergodize the edge field. This means that the magnetic field structure of MAST with RMP coils turned on may more closely resemble the field structure in stellarators. Comparison of fluctuation data may shed more light on the question of universality and the role of magnetic field structure in edge turbulence.

In the following, ergodization of vacuum magnetic fields by RMP fields is illustrated. We consider an equilibrium magnetic field in cylindrical coordinates (r, θ, z), where $0 \leq r \leq a$ is along the minor radius, $0 \leq \theta < 2\pi$ is the poloidal angle and $0 \leq z < 2\pi$ is the toroidal angle:

$$\mathbf{B} = B_0 \left[\hat{\phi} + \frac{1}{q} \hat{\mathbf{z}} \right] \ , \tag{6.1}$$

where q is the safety factor. We assume that the RMP field can be written in terms of a magnetic potential $\mathbf{A} = A\hat{\mathbf{z}}$ such that the total field becomes

$$\mathbf{B} = B_0 \left[\hat{\mathbf{z}} + \frac{1}{q} \hat{\theta} \right] + \nabla \times A\hat{\mathbf{z}} = B_0 \left[\hat{\mathbf{z}} + \frac{1}{q} \hat{\theta} \right] + \frac{1}{r} \frac{\partial A}{\partial \theta} \hat{\mathbf{r}} - \frac{\partial A}{\partial r} \hat{\theta} \ . \tag{6.2}$$

We assume the form of A to be [Reiser, 2007]

$$A = -\sum_m (-1)^m A_0 \exp\left[m(r-a)/a\right] \cos\left[m\theta - nz\right] \ . \tag{6.3}$$

Field lines can be traced by solving the following equations,

$$\frac{\partial \theta}{\partial z} = \frac{1}{qR} - \frac{1}{rB_0} \frac{\partial A}{\partial r} \text{ and } \frac{\partial r}{\partial z} = \frac{1}{rB_0} \frac{\partial A}{\partial \theta} \ , \tag{6.4}$$

where z is used as a pseudo-time for numerical integration using the Karniadakis third order scheme [Karniadakis et al., 1991]. 150 field lines are traced around the torus 1000

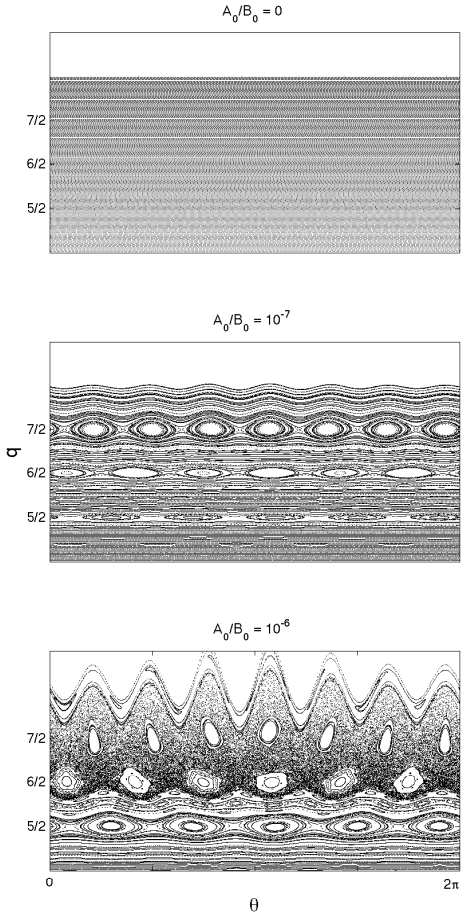

Figure 6.1: Poincare plot of the magnetic field produced by equation 6.3 and 6.2.

times each and figure 6.1 shows the resulting Poincare plot for different values of the ratio A_0/B_0. With $A_0/B_0 = 0$, there is no RMP field and the field lines form straight flux surfaces. As A_0/B_0 is increased, magnetic islands form on resonant $q = m/n$ surfaces, $m = [5, 6, 7]$ $n = 2$. For large values of $A_0/B_0 = 0$, these magnetic islands overlap and the field becomes ergodic.

6.1.2 Modifications to the Hasegawa-Wakatani equations

In this thesis, modifications to the Hasegawa-Wakatani equations to include the effects of non-uniform magnetic field strength and zonal flows have been studied. Other simple modifications include considering magnetic fluctuations, temperature fluctuations and magnetic shear. The HW equations can also be solved in three dimensions. Figure 6.2 shows a snapshot of potential taken from a simulation of the three-dimensional HW equations, using a modified form of the HAWK code. The effect of these modifications

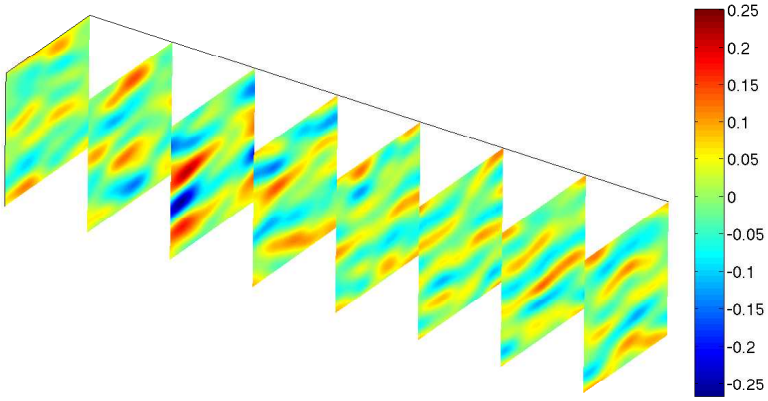

Figure 6.2: Snapshot of potential for the three dimensional Hasegawa-Wakatani model.

on the statistics and the transport of test particles may provide interesting results. Modifying the test particle equation of motion to include more physics is also possible. In the longer term, the HAWK code may be modified in order to solve more complicated equations, such as the gyrofluid equations, and in a more realistic geometry, e.g. toroidal geometry using a field aligned coordinate system.

Bibliography

C Angioni and A G Peeters. Gyrokinetic calculations of diffusive and convective transport of alpha particles with a slowing-down distribution function. *Physics of Plasmas*, 15: 052307, 2008.

S V Annibaldi, G Manfredi, R O Dendy, and L O'C Drury. Evidence for strange kinetics in hasegawa-mima turbulent transport. *Plasma Physics and Controlled Fusion*, 42: L13, 2000.

S V Annibaldi, G Manfredi, and R O Dendy. Non-gaussian transport in strong plasma turbulence. *Physics of Plasmas*, 9:791, 2002.

G Y Antar, G Counsell, Y Yu, B Labombard, and P Devynck. Universality of intermittent convective transport in the scrape-off layer of magnetically confined devices. *Physics of Plasmas*, 10:419, 2003.

A Arakawa. Computational design for long-term numerical integration of the equations of fluid motion: Two-dimensional incompressible flow. part i. *Journal of Computational Physics*, 1:119, 1966.

C W Van Atta and R A Antonia. Reynolds number dependence of skewness and flatness factors of turbulent velocity derivatives. *Physics of Fluids*, 23:252, 1980.

A L Barabasi and E Stanley. *Fractal Concepts in Surface Growth*. Cambridge University Press, 1995.

R Basu, T Jessen, V Naulin, and J Juul Rasmussen. Turbulent flux and the diffusion of passive tracers in electrostatic turbulence. *Physics of Plasmas*, 10:2696, 2003a.

R Basu, V Naulin, and J Juul Rasmussen. Particle diffusion in anisotropic turbulence. *Communications in Nonlinear Science and Numerical Simulation*, 8:477, 2003b.

R Benzi, S Ciliberto, R Tripiccione, C Baudet, F Massaioli, and S Succi. Extended self-similarity in turbulent flows. *Physical Review E*, 48:R29, 1993.

D Biskamp. *Nonlinear Magnetohydrodynamics*. Cambridge University Press, 1993.

J A Boedo, D L Rudakov, R A Moyer, G R McKee, R J Colchin, M J Schaffer, P G Stangeby, W P West, S L Allen, T E Evans, R J Fonck, E M Hollmann, S Krasheninnikov, A W Leonard, W Nevins, M A Mahdavi, G D Porter, G R Tynan, D G Whyte, and X Xu. Transport by intermittency in the boundary of the diii-d tokamak. *Physics of Plasmas*, 10:1670, 2003.

W J T Bos, S Futatani, S Benkadda, M Farge, and K Schneider. The role of coherent vorticity in turbulent transport in resistive drift-wave turbulence. *Physics of Plasmas*, 15:072305, 2008.

S I Braginskii. Transport processes in a plasma. *Reviews of Plasma Physics*, 1:205, 1965.

S J Camargo, D Biskamp, and B D Scott. Resistive drift wave turbulence. *Physics of Plasmas*, 2:48, 1995.

B A Carreras, C Hidalgo, E Sanchez, M A Pedrosa, R Balbin, I Garcia-Cortes, B Ph van Milligen, D E Newman, and V E Lynch. Fluctuation-induced flux at the plasma edge in toroidal devices. *Physics of Plasmas*, 3:2664, 1996.

B A Carreras, B Ph van Milligen, M A Pedrosa, R Balbin, C Hidalgo, D E Newman, E Sanchez, M Frances, I Garcia-Cortes, J Bleuel, M Endler, C Riccardi, S Davies,

G F Matthews, E Martines, V Antoni, A Latten, and T Klinger. Self-similarity of the plasma edge fluctuations. *Physics of Plasmas*, 5:3632, 1998.

T A Carter. Intermittent turbulence and turbulent structures in a linear magnetized plasma. *Physics of Plasmas*, 13:010701, 2006.

CCFE, August 2009. `http://fusion.org.uk`.

F F Chen. Spectrum of low beta plasma turbulence. *Physical Review Letters*, 15:381, 1965.

F F Chen. *Introduction to Plasma Physics and Controlled Fusion*. Plenum Press, 1984.

L Chen, M S Chance, and C Z Cheng. *Nuclear Fusion*, 20:901, 1980.

P C Clemmow and J P Dougherty. *Electrodynamics of particles and plasmas*. Addison-Wesley Publishing, 1969.

T Dudok de Wit. *Spectral and statistical analysis of plasma turbulence: beyond linear techniques*. Springer, Berlin, 2003.

R O Dendy. *Plasma Dynamics*. Oxford University Press, 1990.

J M Dewhurst, B Hnat, N Ohno, R O Dendy, S Masuzaki, T Morisaki, and A Komori. Statistical properties of edge plasma turbulence in the large helical device. *Plasma Physics and Controlled Fusion*, 50:095013, 2008.

J M Dewhurst, B Hnat, and R O Dendy. The effects of nonuniform magnetic field strength on density flux and test particle transport in drift wave turbulence. *Physics of Plasmas*, 16:072306, 2009.

J M Dewhurst, B Hnat, and R O Dendy. Finite larmor radius effects on test particle transport in drift wave-zonal flow turbulence. *Plasma Physics and Controlled Fusion*, 52:025004, 2010.

P H Diamond, S-I Itoh, K Itoh, and T S Hahm. Zonal flows in plasma–a review. *Plasma Physics and Controlled Fusion*, 47:R35, 2005.

W Dorland and G W Hammett. Gyrofluid turbulence models with kinetic effects. *Physics of Fluids B*, 5:812, 1993.

B D Dudson, R O Dendy, A Kirk, H Meyer, and G F Counsell. Comparison of l- and h-mode plasma edge fluctuations in mast. *Plasma Physics and Controlled Fusion*, 47: 885, 2005.

R Dux and A G Peeters. Neoclassical impurity transport in the core of an ignited tokamak plasma. *Nuclear Fusion*, 40:1721, 2000.

ENS, August 2009. `www.euronuclear.org`.

FFTW, 2009. `http://fftw.org`.

U Frisch. *Turbulence: The Legacy of A.N. Kolmogorov*. Cambridge University Press, 1995.

U Frisch, P L Sulem, and M Nelkin. A simple dynamical model of intermittent fully developed turbulence. *Journal of Fluid Mechanics*, 87:719, 1978.

S Futatani, S Benkadda, Y Nakamura, and K Kondo. Characterization of intermittency of impurity turbulent transport in tokamak edge plasmas. *Physics of Plasmas*, 15: 072506, 2008.

J P Graves, J Horacek, R A Pitts, and K I Hopcraft. Self-similar density turbulence in the tcv tokamak scrape-off layer. *Plasma Physics and Controlled Fusion*, 47:L1, 2005.

K Gustafson, D del Castillo-Negrete, and W Dorland. Finite larmor radius effects on nondiffusive tracer transport in a zonal flow. *Physics of Plasmas*, 15:102309, 2008.

A Hasegawa and K Mima. Pseudo-three-dimensional turbulence in magnetized nonuniform plasma. *Physics of Fluids*, 21:87, 1978.

A Hasegawa and M Wakatani. Plasma edge turbulence. *Physical Review Letters*, 50: 682, 1983.

T Hauff and F Jenko. Turbulent e?b advection of charged test particles with large gyroradii. *Physics of Plasmas*, 13:102309, 2006.

T Hauff and F Jenko. E?b advection of trace ions in tokamak microturbulence. *Physics of Plasmas*, 14:092301, 2007.

B Hnat, S C Chapman, and G Rowlands. Intermittency, scaling, and the fokker-planck approach to fluctuations of the solar wind bulk plasma parameters as seen by the wind spacecraft. *Physical Review E*, 67:056404, 2003.

B Hnat, B D Dudson, R O Dendy, G F Counsell, A Kirk, and the MAST team. Characterisation of edge turbulence in l-mode plasmas in the mega amp spherical tokamak. *Nuclear Fusion*, 48:085009, 2008.

W Horton. Drift waves and transport. *Reviews of Modern Physics*, 71:735, 1999.

G E Karniadakis, M Israeli, and S O Orzag. High-order splitting methods for the incompressible navier-stokes equations. *Journal of Computational Physics*, 97:414, 1991.

A Kendl, B D Scott, and H Wobig. Transition from tokamak to stellarator turbulence. *Plasma Physics and Controlled Fusion*, 42:L23, 2000.

R H Kraichnan. Inertial ranges in two-dimensional turbulence. *Physics of Fluids*, 10: 1417, 1967.

B LaBombard, R L Boivin, M Greenwald, J Hughes, B Lipschultz, D Mossessian, C S Pitcher, J L Terry, and S J Zweben. Particle transport in the scrape-off layer and its relationship to discharge density limit in alcator c-mod. *Physics of Plasmas*, 8:2107, 2001.

B B Mandelbrot. *Gaussian Self-Afinity and Fractals*. Springer-Verlag Berlin, 2002.

G Manfredi and R O Dendy. Test-particle transport in strong electrostatic drift turbulence with finite larmor radius effects. *Physical Review Letters*, 76:4360, 1996.

G Manfredi and R O Dendy. Transport properties of energetic particles in a turbulent electrostatic field. *Physics of Plasmas*, 4:628, 1997.

P Manz, M Ramisch, and U Stroth. Experimental estimation of the dual cascade in two-dimensional drift-wave turbulence. *Plasma Physics and Controlled Fusion*, 51: 035008, 2009a.

P Manz, M Ramisch, and U Stroth. Physical mechanism behind zonal-flow generation in drift-wave turbulence. *Physical Review Letters*, 103:165004, 2009b.

S Masuzaki, T Morisaki, N Ohyabu, A Komori, H Suzuki, N Noda, Y Kubota, R Sakamoto, K Narihara, K Kawahata, K Tanaka, T Tokuzawa, S Morita, M Goto, M Osakabe, T Watanabe, Y Matsumoto, O Motojima, and the LHD Experimental group. The divertor plasma characteristics in the large helical device. *Nuclear Fusion*, 42:750, 2002.

V Naulin. Aspects of flow generation and saturation in drift-wave turbulence. *New Journal of Physics*, 4:28, 2002.

V Naulin. Electromagnetic transport components and sheared flows in drift-alfven turbulence. *Physics of Plasmas*, 10:4016, 2003.

V Naulin and A Nielsen. Accuracy of spectral and finite difference schemes in 2d advection problmes. *SIAM Journal on Scientific Computing*, 25:104, 2003.

V Naulin, A H Nielsen, and J Juul Rasmussen. Dispersion of ideal particles in a two-dimensional model of electrostatic turbulence. *Physics of Plasmas*, 6:4575, 1999.

V Naulin, O E Garcia, M Priego, and J Juul Rasmussen. The application of passive tracers for investigating transport in plasma turbulence. *Physica Scripta*, T112:129, 2006.

V Naulin, J Juul Rasmussen, C Angioni, C Giroud, M Valisa, M E Puiatti, and L Carraro. Turbulent impurity transport. *AIP Conference Proceedings*, 1013:191, 2008.

NIFS, August 2009. `http://www.lhd.nifs.ac.jp/en/`.

R Numata, R Ball, and R L Dewar. Bifurcation in electrostatic resistive drift wave turbulence. *Physics of Plasmas*, 14:102312, 2007.

N Ohno, S Masuzaki, V P Budaev, H Miyoshi, S Takamura, T Morisaki, N Ohyabu, and A Komori. Bursty fluctuation characteristics in sol/divertor plasmas of large helical device. *21st IAEA Fusion Energy Conference (Chengdu)*, pages EX/P4–20, 2006a.

N Ohno, S Masuzaki, H Miyoshi, S Takamura, V P Budaev, T Morisaki, N Ohyabu, and A Komori. Analysis on relation between magnetic structure and bursty fluctuation in sol/divertor plasmas of lhd. *Contributions to Plasma Physics*, 46:692, 2006b.

H Pecseli. Plasmafysikk - en introduksjon, August 2009. `http://www.fys.uio.no/plasma/plasma/norsk/`.

H L Pecseli and J Trulsen. A statistical analysis of numerically simulated plasma turbulence. *Physics of Fluids B*, 1:1616, 1989.

T S Pedersen, P K Michelsen, and J Juul Rasmussen. Lyapunov exponents and particle dispersion in drift wave turbulence. *Physics of Plasmas*, 3:2939, 1996.

M A Pedrosa, C Hidalgo, D Lopez-Bruna, A Lopez-Fraguas, J Castellano, and J A Jimenez. Experimental evidence of fluctuation-induced inward transport linked to rational surfaces in the tj-ii stellarator. *Plasma Physics and Controlled Fusion*, 43: 1573, 2001.

A G Peeters, 2009. Private communication.

W H Press, B P Flannery, S A Teukolsky, and W T Vetterling. *Numerical Recipes in C*. Cambridge University Press, 1993.

D Reiser. Impact of large island perturbations on turbulence blob transport in tokamaks. *Physics of Plasmas*, 14:082314, 2007.

S K Saha and S Chowdhury. Intermittent transport in the scrape-off layer of the sinp tokamak. *Physics of Plasmas*, 13:092512, 2006.

E Sanchez, C Hidalgo, D Lopez-Bruna, I Garcia-Cortes, R Balbin, M A Pedrosa, B van Milligen, C Riccardi, G Chiodini, J Bleuel, M Endler, B A Carreras, and D E Newman. Statistical characterization of fluctuation wave forms in the boundary region of fusion and nonfusion plasma. *Physics of Plasmas*, 7:1408, 2000.

R Sanchez, D E Newman, J N Leboeuf, B A Carreras, and V K Decyk. On the nature of radial transport across sheared zonal flows in electrostatic ion-temperature-gradient gyrokinetic tokamak plasma turbulence. *Physics of Plasmas*, 16:055905, 2009.

B D Scott. Exb shear flows and electromagnetic gyrofluid turbulence. *Physics of Plasmas*, 7:1845, 2000.

B D Scott. Energetics of the interaction between electromagnetic exb turbulence and zonal flows. *New Journal of Physics*, 7:92, 2005.

B D Scott. Basics of turbulence computation for magnetically confined plasmas. *AIP Conference Proceedings*, 1013:316, 2008.

A I Smolyakov, P H Diamond, and M Malkov. Coherent structure phenomena in drift wavezonal flow turbulence. *Physical Review Letters*, 84:491, 2000.

D Sornette. *Critical Phenomena in Natural Sciences*. Springer-Verlag Berlin, 2000.

H Sugama, M Wakatani, and A Hasegawa. Study of resistive drift and resistive interchange modes in a cylindrical plasma with magnetic shear. *Physics of Fluids*, 31:1601, 1988.

D J Thomson. Spectrum estimation and harmonic analysis. *Proceedings of the IEEE*, 70:1055, 1982.

B Ph van Milligen, R Sánchez, B A Carreras, V E Lynch, B LaBombard, M A Pedrosa, C Hidalgo, B Goncalves, R Balbin, and the WZ-AS Team. Additional evidence for the universality of the probability distribution of turbulent fluctuations and fluxes in the scrape-off layer region of fusion plasmas. *Physics of Plasmas*, 12:052507, 2005.

M Vergote, M Van Schoor, Y Xu, S Jachmich, and R Weynants. The interplay between reynolds stress and zonal flows: direct numerical simulation as a bridge between theory and experiment. *Plasma Physics and Controlled Fusion*, 48:S75, 2006.

M Vlad and F Spineanu. Larmor radius effects on impurity transport in turbulent plasmas. *Plasma Physics and Controlled Fusion*, 47:281, 2005.

M Vlad, F Spineanu, S-I Itoh, M Yagi, and K Itoh. Turbulent transport of ions with large larmor radii. *Plasma Physics and Controlled Fusion*, 47:1015, 2005.

J Weiss. The dynamics of enstrophy transfer in two-dimensional hydrodynamics. *Physica D: Nonlinear Phenomena*, 48:273, 1991.

J Wesson. *Tokamaks*. Oxford University Press, 2004.

Y H Xu, S Jachmich, R R Weynants, and the TEXTOR team. On the properties of turbulence intermittency in the boundary of the textor tokamak. *Plasma Physics and Controlled Fusion*, 47:1841, 2005.

C X Yu, M Gilmore, W A Peebles, and T L Rhodes. Structure function analysis of long-range correlations in plasma turbulence. *Physics of Plasmas*, 10:2772, 2003.

S Zoletnik, M Anton, M Endler, S Fiedler, M Hirsch, K McCormick, J Schweinzer, and the W7-AS Team. Density fluctuation phenomena in the scrape-off layer and edge plasma of the wendelstein 7-as stellarator. *Physics of Plasmas*, 6:4239, 1999.

S J Zweben, J A Boedo, O Grulke, C Hidalgo, B LaBombard, R J Maqueda, P Scarin, and J L Terry. Edge turbulence measurements in toroidal fusion devices. *Plasma Physics and Controlled Fusion*, 49:S1, 2007.